Technische Universität Braunschweig

Manuela Gerken

Quantitative and Traceable Measurement Techniques for Magnetic Microstructures

Dissertation
Braunschweig 2020

Berichte aus dem **Institut für Elektrische Messtechnik und Grundlagen der Elektrotechnik**

Band **70**

Hrsg. Prof. Dr. Meinhard Schilling

Quantitative and Traceable Measurement Techniques for Magnetic Microstructures

Von der Fakultät für Elektrotechnik, Informationstechnik, Physik
der Technischen Universität Carolo-Wilhelmina zu Braunschweig

zur Erlangung des Grades einer Doktorin

der Ingenieurwissenschaften (Dr.-Ing.)

genehmigte Dissertation

von Manuela Gerken

aus Zeven

eingereicht am: 17.07.2020

mündliche Prüfung am: 08.10.2020

1. Referent: Prof. Dr. rer. nat. Meinhard Schilling

2. Referent: PD Dr. rer. nat. Hans Werner Schumacher

Druckjahr: 2021

Dissertation an der Technischen Universität Braunschweig,
Fakultät für Elektrotechnik, Informationstechnik, Physik

Kurzfassung

Für die quantitative Charakterisierung von wissenschaftlich und industriell relevanten magnetischen Mikrostrukturen werden rückgeführt kalibrierte magnetische Messtechniken benötigt. Hier werden zwei Ansätze, die magnetische Streufelder detektieren, weiterentwickelt und charakterisiert und zwar Raster-Hall-Sonden-Mikroskopie (SHPM, engl. scanning Hall probe microscopy) und magnetooptische Indikatorfilm (MOIF) Technik. Hall-Sensoren basierend auf Gold und Graphen mit bis zu $50 \times 50\,\mathrm{nm}^2$ kleinen aktiven Flächen wurden unter der Anwendung von Elektronenstrahllithographie hergestellt. Nach der Charakterisierung wurden Gold-Hall-Sensoren auf der Spitze von Biegebalken in ein auf Rasterkraftmikroskopie basierendes Rastersystem integriert. Dies ermöglichte die rückgeführte Messung der Streufeldverteilung eines magnetischen Maßstabes unter Umgebungsbedingungen. Um den Kalibrierprozess zu vervollständigen, wurde eine systematische Unsicherheitsanalyse der Hall-Sensor-Charakterisierung sowie der SHPM durchgeführt. Die Resultate wurden mittels Vergleich mit den Ergebnissen von zwei Simulationsmethoden verifiziert. Außerdem wird eine Kalibrierprozedur für die schnelle Messung von magnetischen Proben basierend auf dem magneto-optischen Faraday-Effekt eingeführt und am Beispiel eines kommerziellen MOIF-Gerätes gezeigt. Zuerst wird eine makroskopische Kalibrierung ausgeführt, welche die vom Gerät gemessene Intensität mit der homogenen, magnetischen Flussdichte verknüpft, die senkrecht zur Sensorfläche von einem Elektromagneten angelegt wird. Die Eigenschaften des Elektromagneten und das Verhalten des MOIF-Gerätes selbst fließen mit in das detaillierte Unsicherheitsbudget ein. Diese pixelweise Kalibrierung beinhaltet örtlich variierende Eigenschaften des MOIFs und eine inhomogene Ausleuchtung sowie den Einfluss magnetischer Anisotropien des MOIF-Materials, welche durch ferromagnetische Resonanzmessungen ermittelt wurden. Die mikroskopische Kalibrierung hat eine Simulation der Geräteantwort auf das Streufeld mikroskaliger magnetischer Proben mit einem örtlich schnell variierenden Magnetfeld zum Ziel. Für den hier verwendeten MOIF zeigte sich ein signifikanter Effekt der in der Ebene liegenden Streufeldkomponenten und ein vernachlässigbarer Einfluss der MOIF-Dicke. Die Gültigkeit der nicht nur implementierten sondern auch rückgeführt kalibrierten SHPM und MOIF-Techniken wurde durch einen Quervergleich der Ergebnisse der Charakterisierung eines magnetischen Maßstabes unter Berücksichtigung der Unsicherheitsbudgets nachgewiesen. Die Ergebnisse dieser Arbeit ermöglichen erstmals die metrologisch rückgeführte Charakterisierung magnetischer Streufelder auf Größenskalen von einigen Mikrometern und im Feldbereich von $2\,\mathrm{mT}$ bis $1\,\mathrm{T}$.

Abstract

For the quantitative characterization of scientific and industrial relevant magnetic microstructures traceably calibrated measurement techniques are required. Here, two magnetic stray field detection approaches, namely scanning Hall probe microscopy (SHPM) and magneto-optical indicator film (MOIF) technique, are presented. Hall sensors based on gold and graphene with active areas down to $50 \times 50\,\mathrm{nm}^2$ were fabricated utilizing electron beam lithography. After the characterization, gold Hall sensors on cantilever tips were integrated into an atomic force microscopy based scanning system. This allowed the traceable measurement of the stray field distribution of a magnetic scale under ambient conditions. To complete the calibration process, a systematic uncertainty analysis for the Hall sensor characterization as well as for the SHPM was performed. The results were verified by comparison to the output from two simulation approaches. Moreover, a calibration procedure for fast magnetic sample measurements based on the magneto-optical Faraday effect is introduced and demonstrated on the example of a commercial MOIF device. First, a macroscopic calibration is executed which relates the intensity measured by the device to the homogeneous magnetic flux density applied perpendicular to the sensor surface by an electromagnet. Properties of the electromagnet and the behavior of the MOIF device itself enter into the detailed uncertainty budget. This pixel-wise calibration incorporates spatially varying MOIF properties and a inhomogeneous illumination as well as the influence of magnetic anisotropies of the MOIF material, which were ascertained via ferromagnetic resonance measurements. Second, the microscopic calibration has the aim of simulating the device response to stray fields of microscale magnetic samples with spatially fast varying magnetic fields. For the here utilized MOIF, a significant effect of in-plane stray field components and a neglectable influence of the MOIF thickness was observed. The validity of not only implemented but also traceably calibrated SHPM and MOIF techniques was proven by a cross-comparison of results from the characterization of a magnetic scale under consideration of the uncertainty budgets. The results of this thesis enable the metrological traceable characterization of magnetic stray fields on scales of a few micrometer and in a field range from 2 mT to 1 T.

Contents

Kurzfassung I

Abstract III

Contents V

1 Introduction 1

2 Theoretical background 6
2.1 Methods . . . 6
2.1.1 Hall measurements . . . 6
2.1.2 Magneto-optics and Faraday effect . . . 7
2.1.3 Magnetic anisotropies . . . 10
2.1.4 Influence of anisotropies and external magnetic fields on the magnetization direction . . . 11
2.1.5 Ferromagnetic resonance measurements . . . 14
2.1.6 Approximation of the sample magnetization structure . . . 17
2.1.7 Stray field calculation with transfer functions . . . 19
2.1.8 Uncertainty analysis . . . 23
2.2 Material properties . . . 25
2.2.1 Gold . . . 25
2.2.2 Graphene . . . 26
2.2.3 Bismuth-substituted rare earth iron garnet . . . 28

3 Scanning probe microscopy with nano- and micro-size Hall sensors 29
3.1 Fabrication . . . 29
3.1.1 Fabrication basics . . . 29
3.1.2 Gold Hall sensors . . . 31
3.1.3 Graphene Hall sensors . . . 33
3.2 Characterization . . . 35
3.3 Scanning probe system . . . 40
3.4 SHPM measurement of a magnetic scale . . . 41
3.5 Uncertainty budget . . . 44
3.6 Verification by comparison to simulation . . . 45
3.7 Conclusion SHPM . . . 49

4 Calibration of a magneto-optical measurement system 52
4.1 Characterization of the calibration magnet . . . 52
4.2 Properties of the MOIF device . . . 55
4.2.1 Noise, operating temperature, repeatability . . . 55
4.2.2 MOIF saturation magnetization . . . 57

4.2.3 MOIF magnetic anisotropies . . . 57
4.3 Macroscopic calibration . . . 60
4.3.1 Theory . . . 60
4.3.2 Results . . . 63
4.3.3 Uncertainty . . . 64
4.3.4 Discussion and summary . . . 65
4.4 Microscopic calibration . . . 66
4.4.1 Simulation of device response for vector stray fields . . . 66
4.4.2 Influence of MOIF thickness . . . 67
4.5 Application . . . 69
4.5.1 Measurement and simulation of a magnetic scale . . . 69
4.5.2 Uncertainty Budget . . . 70
4.6 Conclusion MOIF calibration . . . 72

5 Comparison of measurement techniques 73

6 Conclusion and Outlook 82

A Explanation of exponential stray field decrease 85

B Fabrication details and parameters 87
B.1 Gold . . . 87
B.2 Graphene . . . 88

List of Abbrevations 91

List of Symbols 93

List of Figures 96

List of Tables 98

References 99

Own Publications 107

Acknowledgements 110

1 Introduction

Magnetic sensors are important for scientific sample characterization as well as for industrial applications. Encoders consisting of a sensor and a magnetic scale are utilized for positioning processes. For example, the defined movement of microscope tables or plant facilities is realized with linear encoders. Also, the rotation of steering wheels or motors can be detected by counting up and down magnetized poles with an encoder. Thus, they are applicable for angle measurements as well. During magnetic scale fabrication, characterization techniques with short measurement times are required for in-line quality control. Within the overall optimization process of smaller, faster, cheaper and better sensors, also the structure and pole size of magnetic samples is decreased. For instance, the production of high quality magnetic scales with defined pole sizes in the nanometer range will enable even more precise position measurements. These scales might replace optical scales due to lower fabrication costs and higher temperature stability. Furthermore, they are unaffected by dust, which would prevent optical read out, and are thus robust in industrial environments. However, the development of such small magnetic structures requires suitable quantitative measurement techniques with high spatial resolution to verify the requested properties. Only few magnetic measurement techniques are available on these small length scales, and those existing are not adequately calibrated. Therefore, in this thesis two traceably calibrated stray field measurement methods for magnetic microstructures were developed. As it is well-known for all metrologists, a calibration is not possible without a detailed uncertainty analysis, which is also described here. The scientific community will profit from these results, since only a correctly determined and stated uncertainty budget allows comparability of measurement results.

Two main challenges need to be overcome for the realization of quantitative and microscale stray field measurements. First, stray fields of magnetic microstructures change their direction and amplitude within a few micrometers as visualized in Figure 1.1(a). Regarding typical actual sensor sizes, they can to no extend be considered as homogeneous, and all three stray field components must be taken into account. Therefore, the utilized sensors are supposed to be as small as possible to avoid field averaging or even canceling. The applied measurement techniques should offer a high spatial resolution and a precise positioning. Second, the stray fields varying on the microscale exhibit a fast exponential field decay with increasing distance to the sample surface [1, 2] as shown in Figure 1.1(b). At a certain point the signal amplitude

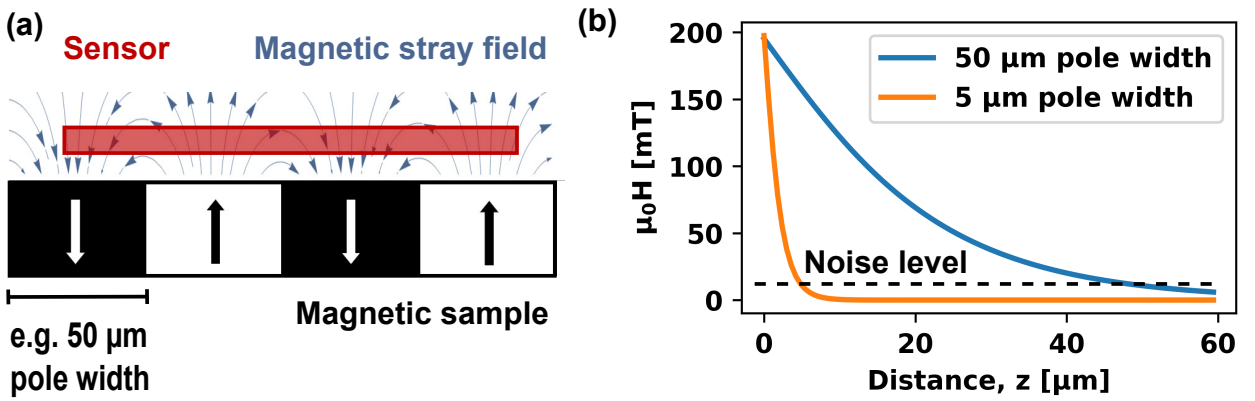

Figure 1.1: Stray field properties of magnetic microstructures. (a) Spatial stray field distribution of a magnetic sample. (b) Decay of the magnetic flux density with increasing distance to the sample surface for two magnetic scales with different pole sizes.

drops below the sensor noise level. Consequently, low measurement heights, smaller than the structure sizes, are necessary.

The two approaches pursued here to solve the described problems are scanning Hall probe microscopy (SHPM) [3–5] and magneto-optical indicator film (MOIF) [6, 7] technique. The demand for suitable and Hall sensor based measurement methods can be derived from the existence of commercial SHPM systems utilizing sub-micron Hall probes at room temperature (RT) [8, 9]. In the relevant field range from a few mT to 500 mT Hall sensors are superior to magneto resistive sensors due to their intrinsically better linearity [10, 11]. In comparison to another popular scanning approach, namely magnetic force microscopy (MFM) [12, 13], SHPM is directly quantitative but has a lower spatial resolution. Moreover, SHPM is non-invasive, which means that the magnetization of the sample is not manipulated because no magnetic materials are present and the magnetic field generated by the operating current is too small. Therefore, the sensor can be operated in proximity to the sample surface where the actual measurement height is determined by the scanning system, the sensor integration and the sample's surface character. This enables a high spatial resolution only limited by the positioning accuracy and the sensor size. Furthermore, a three dimensional image of the stray field can be generated by repeating two dimensional scans at different heights [14]. However, a systematic determination of uncertainty contributions is missing, which is indispensable for significant measurement results. Also, small and low noise Hall elements are rare, which are especially necessary for RT measurements on microstructures.

Concerning SHPM, besides a detailed investigation of the uncertainty budget the method can be improved for RT measurements of magnetic microstructures by applying suitable Hall sensors. Conventional semiconductor based Hall sensors reveal an especially good performance at low temperatures [15]. At RT only sensors down to a minimal active area in the micrometer range are applicable [3, 16, 17]. The in general beneficial small carrier density of semiconductors for Hall sensor applications becomes a drawback for nano-sized sensors at RT. Fluctuations in the small number of carriers appear and create noise on the Hall signal. Furthermore, the fabrication of nano-sized active areas is challenging for semiconductors due to the depletion region. [18] Therefore, in this work uncommon sensing materials, namely gold and graphene, were examined for the utilization in SHPM systems. This included the fabrication and characterization of gold and graphene Hall sensors as well as the analysis of the performance of calibrated SHPM measurements. Gold was chosen due to the fact that Hall sensors out of gold with an active area below 500 nm have been shown to exhibit a better noise figure at RT than semiconductor Hall sensors [18]. In general, gold possesses good electrical properties and is chemically stable. Relevant for Hall measurements with a low sensitivity uncertainty is the stable carrier density of gold. Furthermore, it is simple to handle during the fabrication process and can be well deposited on substrates suitable for cantilever fabrication, enabling easily accessible SHPM. Only the high carrier density of the metallic gold leads unfortunately to a rather low sensitivity. The other investigated material, graphene, combines as a semi-metal advantages of semiconductor based and metallic Hall sensors [4, 19–22]. Similar results were reported for another semi-metal, bismuth [5]. On the one hand, graphene offers a low carrier density at RT leading to a high Hall sensitivity. On the other hand its carrier density is sensitive to charge accumulations and a good encapsulation is needed to reduce this impact on the uncertainty. In contrast to semiconductors it is also applicable at high temperatures [19]. A unique property of graphene is the one atomically thin active layer causing the best resolution in the corresponding direction.

In contrast to scanning probe microscopy (SPM) techniques, magneto-optical investigations making use of the magneto-optical Faraday effect in an indicator film enable fast measurements by imaging a two-dimensional plane at one shot. The Faraday effect has been used to detect magnetic stray fields and currents of nanostructures [6, 23]. Also, a time resolution of 100 fs can be achieved [6, 24]. By the application of a MOIF instead of the direct magneto-optical detection of the sample magnetization, it is possible to characterize non-transparent samples. Furthermore, the MOIF is optimized for a large Faraday rotation, which facilitates a better field resolution. The drawbacks are a reduced spatial resolution due to field averaging over the sensor thickness and the distance between the sensor film and the sample. The detectable field range is limited by the saturation magnetization of the MOIF and the optical resolution

limit. The functionality of MOIF setups was demonstrated on different applications like the quantitative analysis of thin hard magnetic samples [25] or the investigation of vortex dynamics in superconductors [26, 27]. The quantitative analysis of electrodynamics in superconductors was performed including a consideration of all three stray field components [28]. Some quantitative measurement approaches incorporate a pixel-wise calibration accounting for inhomogeneous illumination of the indicator film [29, 30]. Although the suitability of MOIFs in principle was demonstrated, some essential issues are still not addressed. A detailed uncertainty analysis, which is mandatory for calibrations, was not reported so far. Also, the investigation of all and complex anisotropy contributions and their influence on the device response was not sufficiently considered.

To close this gap, in this work a calibration procedure for MOIF setups was developed that incorporates these effects. The potency of this approach was demonstrated by applying it to a commercial MOIF device, the CMOS-MagView XL (CMOS: complementary metal oxide semiconductor) from Matesy GmbH [31,32]. The device is capable of imaging millimeter-sized magnetic samples with a resolution of 28 µm due to a $60 \times 45\,\mathrm{mm}^2$ large sensor film. For the quantitative measurement of magnetic microstructures the anisotropy constants of the MOIF were investigated by ferromagnetic resonance (FMR) technique and included in the calibration. The effect of vectorial stray field components on the device response and the averaging over the sensor film thickness were introduced in a simulation algorithm.

The results of this thesis are structured in the following way. In chapter 2 the theoretical background is introduced. Relevant physical effects and measurement methods are explained and a magnetic stray field simulation approach is presented. Furthermore, a short overview about state of the art uncertainty analysis is presented. Finally, the properties of deployed sensing materials are introduced.

Chapter 3 is devoted to SHPM with gold and graphene based Hall sensors. The fabrication of sensors with minimal active area sizes of $50 \times 50\,\mathrm{nm}^2$ is described and their characteristics are presented. The performance of a atomic force microscope (AFM) equipped with 5 µm gold Hall sensor is demonstrated by calibrated SHPM of a magnetic scale. The results are verified by comparison to simulations under consideration of the uncertainty budget.

The calibration of a magneto-optical measurement system is presented in chapter 4. It consists of three main parts: The characterization of the MOIF device and its magnetic properties like anisotropy constants, a macroscopic calibration utilizing the well-known stray field of an electromagnet and a microscopic calibration in terms of a device response simulation. The influences of vectorial stray fields and the sensor thickness on the results are demonstrated at the exemplary measurement of a magnetic scale.

Chapter 5 merges the outcome of the two previous chapters by comparing results from the two measurement methods and the related simulations and thus verifying the calibrations.

The work is finalized in chapter 6 with a conclusion and an outlook. Hereby, the successful implementation and calibration of SHPM and MOIF technique is demonstrated. Furthermore, the importance of a detailed uncertainty analysis for traceable characterization of magnetic microstructures is emphasized.

2 Theoretical background

In the following, the theoretical basics needed to understand the experimental chapters and the challenges of quantitative magnetic stray field measurements of magnetic microstructures are explained.

2.1 Methods

Within this section, the applied measurement techniques like Hall measurements, MOIF technique and FMR are introduced. The underlying physical effects and special magnetic properties are explained. Furthermore, a numerical approach for stray field simulations and the basics of uncertainty analysis are presented.

2.1.1 Hall measurements

One technique to measure the magnetic field utilizes the Hall effect, which was first discovered by Edwin Hall in 1879 [33]. The principle of the Hall effect can be explained with the help of Figure 2.1. An electric conductor containing a charge current is placed in a magnetic field which is oriented perpendicular to the direction of current flow. Here, an electron was chosen to visualize the present forces, because in the Hall sensor material used in this work the charge carriers are mainly electrons. However, the principle also holds for positive charges. While the electrons with charge q are moving with the velocity v, they are affected by the Lorentz force F_L. [34]

$$F_\mathrm{L} = q \cdot \vec{E} + q \cdot \left(\vec{v} \times \vec{B} \right) \tag{2.1}$$

The electrons are deflected to the lower side of the conductor due to the magnetic field $\vec{B}$ leaving positive charges on the opposite surface. Inside the Hall sensor this creates an electric field $\vec{E}$ and thus a force opposed to the magnetic force. In equilibrium condition both forces are balanced. The electric potential can be measured by a voltage perpendicular to the

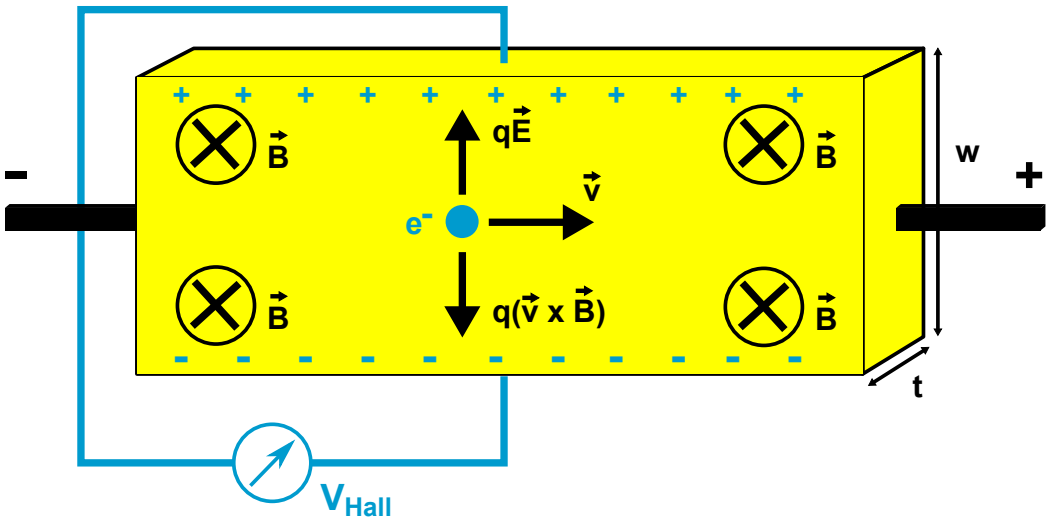

Figure 2.1: Schematic visualizing the Hall effect. Forces effecting an electron current are depicted.

current direction and perpendicular to the magnetic field. This voltage is called Hall voltage V_{Hall} and is given by

$$V_{\text{Hall}} = \frac{I \cdot B}{n \cdot e \cdot t}, \tag{2.2}$$

where I is the supply current, n is the electron density, e is the electron charge and t is the thickness of the active sensing layer. [35] To achieve a large Hall sensitivity $S = \frac{I}{n \cdot e \cdot t}$ for measuring magnetic fields, a large supply current is needed. Furthermore, the sensor should be as thin as possible and contain a low carrier density.

2.1.2 Magneto-optics and Faraday effect

Another method to measure magnetic stray fields employed within this work is based on the magneto-optical Faraday effect first discovered by Michael Faraday in 1845 [36]. This effect describes the fact that linear polarized light that is transmitted through a medium while a magnetic field is applied in the direction of transmission experiences a rotation of the polarization plane. This Faraday rotation angle $\beta(\omega)$ is proportional to the material and frequency dependent Verdet constant $\nu(\omega)$, the length of the medium l and the magnetic field H.

$$\beta(\omega) = \nu(\omega) \cdot l \cdot H \tag{2.3}$$

The effect is enhanced in ferro- and ferrimagnetic materials and here H can be replaced by the magnetization M. Thus, a sample magnetization or a magnetic field can be measured by a detection of the Faraday rotation for example with an analyzer, as shown in Figure 2.2. Only magnetic components oriented parallel or antiparallel to the propagation direction of

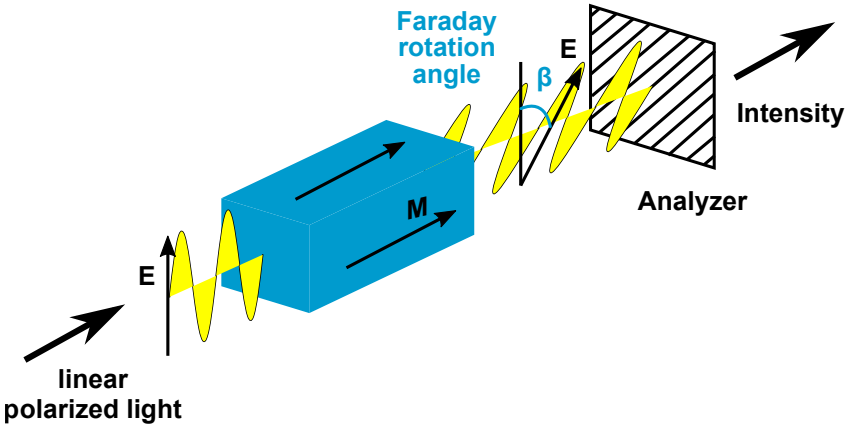

Figure 2.2: Visualization of the magneto-optical Faraday effect.

the light are detected. The two cases are distinguishable by the direction of the rotation. The physical explanation of the effect is given by the different velocities of left and right circularly polarized light in a ferromagnet. Linear polarized light is the combination of two circularly polarized waves with same amplitude. The phase shift of the two waves, originating from the transmission through the ferromagnet, determines the polarization plane of the linearly polarized light. [37]

In this work, a commercially available device, the CMOS-MagView XL from Matesy GmbH [31], which utilizes the magneto-optical Faraday effect for characterizing magnetic structures is calibrated. The device consists of a MOIF and optical components that transfer the Faraday rotation into an intensity signal and map it onto a CMOS chip. The CMOS camera converts the intensity signal into an electrical signal. With this device the magnetization distribution of a sample is not measured directly by its own Faraday effect. Instead, the sample's stray field influences the magnetization of the MOIF and the MOIF magnetization is then detected by the Faraday effect. The application of an indicator film has two main advantages: Firstly, also non transparent samples can be characterized. Secondly, the indicator film can be optimized to reveal a large Faraday rotation and thus an optimized sensitivity and a better resolution. The MOIF used in the CMOS-MagView XL consists of a magneto-optical active layer on a substrate. A mirroring layer is deposited onto the active layer and the whole structure is capped with a hard protection layer. In this device the active layer is a ferrimagnetic bismuth-substituted rare earth iron garnet (Bi-REIG) with an in-plane magnetic anisotropy.

So, in a relaxed state the magnetization lies in the plane of the active layer. The magnetization can be adjusted by out-of the plane sample stray fields. At the utilized wavelength of 590 nm the MOIF shows a doubled Faraday rotation of 10° if the magnetization is saturated in the perpendicular direction. Its saturation field strength is 130 kA/m. In the CMOS-MagView XL a $60 \times 45\,\mathrm{mm}^2$ large MOIF is incorporated, which enables the characterization of the stray field distribution over mm-sized samples at one shot. The spatial resolution is determined by the pixel number of the camera to $28 \times 28\,\mu\mathrm{m}^2$. [32]

The operation principle, of measuring the sample stray field as a brightness contrast by making use of the Faraday effect in an indicator film, is visualized in Figure 2.3. The magnetic

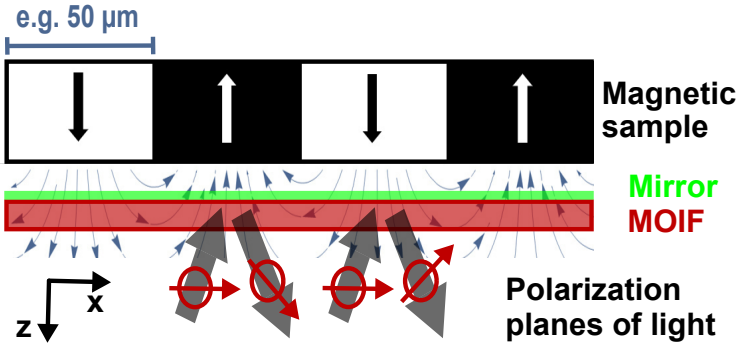

Figure 2.3: Schematic drawing of the MOIF device operation principle. The stray field of the sample orients the magnetization of the MOIF. The z-component of the MOIF magnetization is detected via the Faraday effect by a rotation of the linear polarized light. Using polarizing filters and a camera this Faraday rotation is visualized as a contrast in brightness. Thus, the sample magnetization is measured as an intensity by the device.

sample is placed on top of the MOIF and its magnetic stray field orients the magnetization of the MOIF. From below linear polarized light is transmitted nearly perpendicular to the MOIF plane and is reflected at a mirroring layer on the sensor surface. The polarization plane of the incident light is rotated, due to the Faraday effect, depending on the z-component of the MOIF magnetization which is the component parallel to its transmission direction. With the help of a polarizing filter the position dependent Faraday rotation is converted into a brightness contrast and detected using a camera with an image forming optics. Calibrating this device implies accounting for illumination and sensor inhomogeneities as well as for contributions of the optical path and compensating for CMOS camera pixel related dependencies of the sensitivity. Additionally, non-linearities of the sensor material must be corrected. A suitable structured approach based on a pixelwise calibration is discussed in chapter 4. [Reproduced from Manuela Gerken et al 2020 Meas. Sci. Technol. 31 075009 with permission of IOP Publishing.]

2.1.3 Magnetic anisotropies

The adjustment of magnetic moments in ferro- and ferrimagnetic materials, like the MOIF, is caused by exchange interactions. These interactions lead to spontaneous magnetizations and the formation of domains. However, the sum of all domains and their magnetization directions results in zero external magnetic field. Thus, another influence factor must be responsible for an externally measurable magnetic field. It is the magnetic anisotropy energy that determines the overall magnetization direction of a sample. Without external field, the magnetization points into the direction of one of the easy axes determined by the anisotropies. The magnetic anisotropy energy is the energy which is needed to rotate the magnetization from an easy into a hard direction. There are several contributions generating an anisotropy. [38, 39]

Shape anisotropy

One cause is the shape of a magnetic sample in combination with the dipole-dipole interaction of magnetic moments. For example in a thin film the preferable magnetization direction is in the film plane. This reduces the demagnetization field $\boldsymbol{H}_{\mathrm{demag}}$ and thus minimizes the stray field energy

$$F_{\mathrm{demag}} = -\frac{1}{2}\int \mu_0 \boldsymbol{M}\boldsymbol{H}_{\mathrm{demag}}\,\mathrm{d}V. \tag{2.4}$$

$\boldsymbol{M}$ is the vector of the magnetization and V is the volume of the sample. For symmetric samples, $\boldsymbol{H}_{\mathrm{demag}}$ can be expressed by

$$\boldsymbol{H}_{\mathrm{demag}} = -N\boldsymbol{M} \tag{2.5}$$

with the diagonal demagnetization tensor N. N incorporates the sample geometry. For example, $\mathrm{tr}(N) = 1/3 + 1/3 + 1/3$ for a sphere and $\mathrm{tr}(N) = 0 + 0 + 1$ for a film with infinitesimal thin layer thickness.

Crystalline anisotropy:

Another important contribution is based on the crystallographic structure. The electrons are coupled to the lattice atoms. This in combination with spin-orbit interactions creates easy and hard axes within the crystal. For example, a cubic lattice creates a cubic anisotropy component. In general, the crystalline anisotropy energy is given by

$$F_{\mathrm{crys}} = K_0 + K_1 \sin^2\theta + K_2 \sin^4\theta + ... \tag{2.6}$$

with θ being the angle between the magnetization and the corresponding coordinate axis.

Also stress effects the magnetic anisotropy because the atomic lattice is deformed. This effect is known as magnetostriction. Surfaces and interfaces influence the anisotropy due to the broken symmetry. Some of these different physical contributions can cause similar effects. An out-of-plane anisotropy, for example, can originate from the sample shape, the crystal structure or unidirectional stress.

2.1.4 Influence of anisotropies and external magnetic fields on the magnetization direction

As explained in the previous section, the direction of the magnetization is determined through magnetic anisotropies. The interesting question now is, in which direction the magnetization $\boldsymbol{M}$ points if an external magnetic field $\boldsymbol{H}$ is applied to a magnetically anisotropic sample. This is exactly the case at MOIF measurements where the stray field of a magnetic sample reorients the magnetization of the MOIF. A demonstrative solution for this problem can be given for Stoner-Wohlfarth-particles, which are small enough to comprise a uniform magnetization equal to the saturation magnetization M_S. [39,40] Although the MOIF contains domains that are magnetized in the plane of the film, the general concept explained in the following can be transferred to get an idea of the approximate magnetization behavior of each domain in the MOIF.

A description of the coherent rotation of the magnetization in two dimensions under an arbitrary magnetic anisotropy is given in [41] and extended for three dimensions in [42]. Here, the two dimensional approach is sufficient to demonstrate the effects of magnetic anisotropies and applied magnetic fields on the direction of the magnetization. This direction is determined by the lowest particle energy F.

$$F(\boldsymbol{h}) = \min\left[F(\boldsymbol{m}) = G(\boldsymbol{m}) - 2 \cdot \boldsymbol{h} \cdot \boldsymbol{m}\right] \tag{2.7}$$

The anisotropy energy density divided by K the anisotropy constant is G. The reduced external field is $\boldsymbol{h} = \frac{\boldsymbol{H} \cdot M_\mathrm{S}}{2 \cdot K}$ and $\boldsymbol{m} = \frac{\boldsymbol{M}}{M_\mathrm{S}} = (\cos\zeta, \sin\zeta)$ is the normalized vector of the magnetization. The angle ζ is the sought angle which is enclosed by $\boldsymbol{M}$ and the easy axis, here the x-axis, as indicated in Figure 2.4. Due to the consideration of a two-dimensional case, here, the in-plane angles χ and ϕ are set to zero. A general solution for Equation 2.7 is given by

$$0 = \frac{\mathrm{d}G}{\mathrm{d}\zeta} - 2 \cdot \boldsymbol{h} \cdot \boldsymbol{e} \tag{2.8}$$

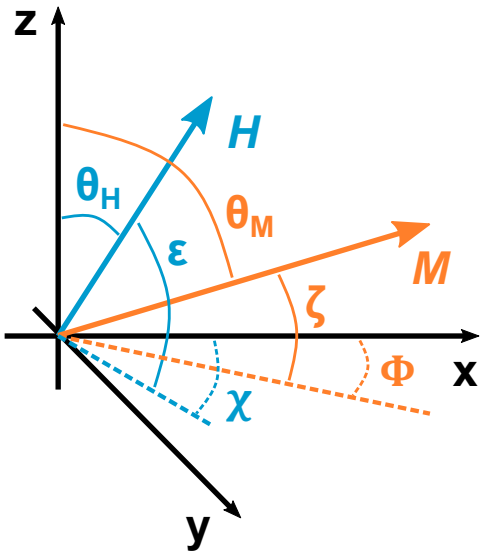

Figure 2.4: Coordinate system introducing the angles between the magnetic field $\boldsymbol{H}$ as well as the magnetization $\boldsymbol{M}$ and the axes of the system.

with $\boldsymbol{e} = (-\sin\zeta, \cos\zeta)$ being the orthogonal vector. As implied in Figure 2.4 $\boldsymbol{M}$ and $\boldsymbol{H}$ are not pointing in the same direction which is caused by the magnetic anisotropy. Furthermore, due to the magnetic anisotropy even a continuous change of $\boldsymbol{H}$, either in amount $|\boldsymbol{H}|$ or direction ϵ, entails jumps in the orientation of the magnetization ζ. This jumps occur around the hard axes at critical fields $\boldsymbol{h}_0$ of

$$\boldsymbol{h}_0 = \frac{1}{2}\left(\frac{\mathrm{d}G}{\mathrm{d}\zeta}\cdot\boldsymbol{e} - \frac{\mathrm{d}^2G}{\mathrm{d}\zeta^2}\cdot\boldsymbol{m}\right). \tag{2.9}$$

The graphical representation of these critical fields is called astroid [41] and shown in Figure 2.5 for a simple uniaxial anisotropy where $\boldsymbol{h}_0 = (-\cos^3\zeta, \sin^3\zeta)$. The direction of the magnetization under magnetic anisotropy and applied fields is graphically determined by drawing lines that are tangent to the critical curve and touch the tip of the field vector. As visualized by the solid and dotted blue lines in Figure 2.5(a) for $\boldsymbol{H}_1$, two suitable tangent lines exist if the applied field is larger than the critical field. However, only the one enclosing the smaller angle ζ with the easy axis and thus pointing more in the direction of the easy axis is stable. If the applied field is smaller than the critical switching field, more than one stable solution is present. In this case, also the magnetic history of the sample influences the direction of the magnetization.

In the following, the concept of utilizing the astroid to determine the magnetization direction is transferred to the MOIF measurement principle. Within MOIF measurements the z-component of the MOIF magnetization M_z is detected. Important is that M_z is not only

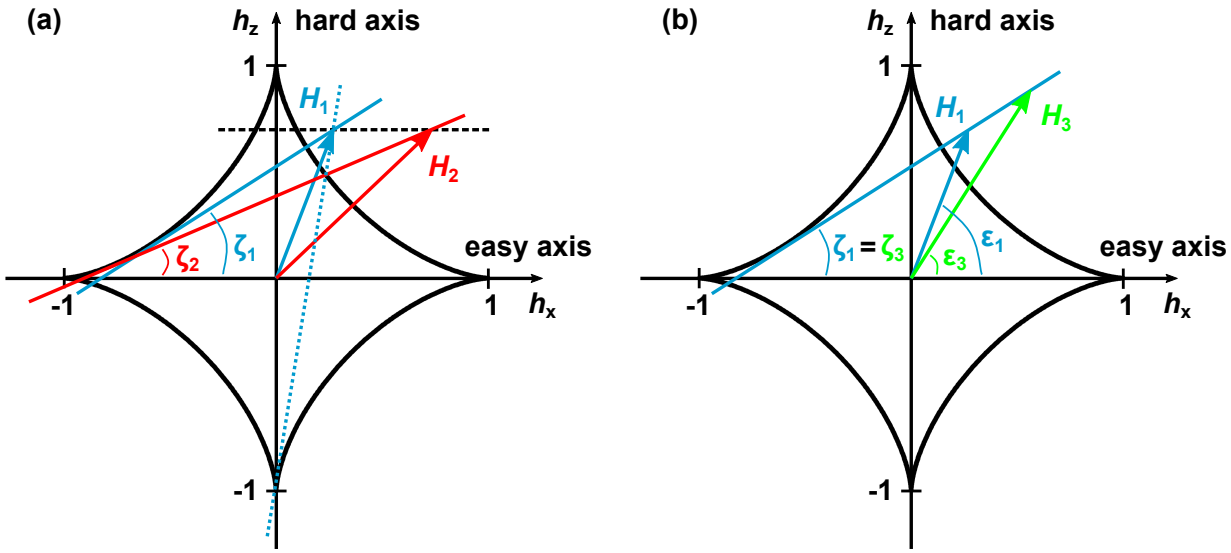

Figure 2.5: Astroid illustrating the critical curve of a out-of-plane uniaxial anisotropy. (a) Demonstration that two magnetic fields $\boldsymbol{H}_1$ and $\boldsymbol{H}_2$ having the same z-component lead to two different magnetization directions ζ_1 and ζ_2. The orientation of the magnetization indicated by the angle ζ is found by drawing lines through the tip of $\boldsymbol{H}$ that are also tangent to the astroid. The line enclosing the smallest angle with the easy axis (solid blue or solid red) denotes the direction of the magnetization. The direction indicated by the dotted blue line belongs to the larger angle and is thus not stable. It is closer to the hard axis than the solid blue line. (b) Visualization of the inverse problem to reconstruct the applied magnetic field from the z-component of the magnetization. From the z-component also ζ is known. Both magnetic fields $\boldsymbol{H}_1$ and $\boldsymbol{H}_3$ end on the tangent line defined by ζ. Similar, other fitting fields can be constructed thus the process is not unambiguous. Adopted from [39].

influenced by the perpendicular stray field component H_z but also by stray field components parallel to the plane H_x and H_y. This is visualized in Figure 2.5(a). The two stray fields $\boldsymbol{H}_1$ and $\boldsymbol{H}_2$ have the same z-component as highlighted by the dashed black line. The difference in the x-component leads to different angles ζ_1 and ζ_2 of the magnetization. With this angles the corresponding z-components of the MOIF magnetization can be calculated by $M_\mathrm{z} = M_\mathrm{S} \cdot \sin\zeta$. Hence, M_z also depends on in-plane stray field components. Demonstrating the influence of in-plane stray field components on the MOIF response with a uniaxial out-of-plane anisotropy is adequate in a first approximation, since in the MOIF this is the largest anisotropy energy as investigated in subsection 4.2.3. Its cubic anisotropy energy and all three dimensions can be considered in a similar way. [42] Consequently, after a calibration of the MOIF in perpendicular, homogeneous stray fields and without further analysis, only pure perpendicular stray fields are measured correctly. This implies that the values measured for a magnetic

scale as shown in Figure 2.3 are only traceable over the centers of each magnetic pole. At these points the stray field is directed perpendicular to the MOIF plane. For the quantitative characterization of the whole sample stray field, a microscopic calibration is introduced in section 4.4.

Within the microscopic MOIF device calibration and for measurement result validation it would be beneficial to calculate the sample stray field from the MOIF device response. This response is based on M_z. Unfortunately, there is no unambiguous assignment for this reverse process as visualized in Figure 2.5(b). The blue tangent line belonging to a detected M_z is drawn from the magnetization angle $\zeta = \arcsin \frac{M_\mathrm{z}}{M_\mathrm{S}}$. There is only one criterion for suitable sample stray fields: Their vector must end on the tangent line. As exemplarily demonstrated by $\boldsymbol{H}_1$ and $\boldsymbol{H}_3$, several suitable stray field vectors exist. Consequently, only the forward calculation from the sample stray field to the MOIF magnetization is unambiguous and applied within this work.

2.1.5 Ferromagnetic resonance measurements

FMR measurements are a versatile tool to investigate the magnetization, spin relaxation times, and magnetic anisotropies of a ferro- or ferrimagnetic sample. The latter is the reason why FMR is used in this work and explained in the following. The behavior of a magnetic dipole $\boldsymbol{m}$ in an effective magnetic field $\boldsymbol{H}_\mathrm{eff}$ is described by the Landau-Lifschitz-Gilbert equation.

$$\frac{\mathrm{d}\boldsymbol{m}}{\mathrm{d}t} = \gamma \cdot [\boldsymbol{m} \times \boldsymbol{H}_\mathrm{eff}] + \frac{\alpha}{m} \cdot \left[\boldsymbol{m} \times \frac{\mathrm{d}\boldsymbol{m}}{\mathrm{d}t}\right], \text{ with } m = |\boldsymbol{m}| \tag{2.10}$$

γ is the gyromagnetic ratio and α the damping parameter. The first term $\gamma \cdot [\boldsymbol{m} \times \boldsymbol{H}_\mathrm{eff}]$ describes a precession of the magnetic dipole around the effective magnetic field. The second term represents the damping torque T_D which causes an alignment of the magnetic dipole with the magnetic field. In a FMR experiment a high frequency magnetic field H_hf is applied perpendicular to the static field $\boldsymbol{H}_\mathrm{eff}$ and $\boldsymbol{m}$ as shown in Figure 2.6. This generates a torque T_hf compensating the damping torque if the frequency of H_hf is equal to the FMR frequency $\omega = -\gamma \times \boldsymbol{H}_\mathrm{eff}$ of the sample under the applied field without damping. The effective field $\boldsymbol{H}_\mathrm{eff}$ is a combination of the applied static field, the Zeeman field, the demagnetization field and magnetic anisotropy fields. Thus, by determining the resonance frequency it is possible to extract the magnetic anisotropies of a sample. [43]

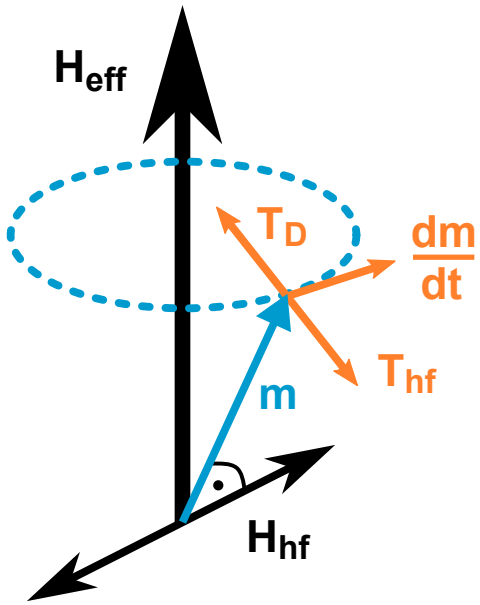

Figure 2.6: Schematic of fields and torques affecting a magnetic dipole under ferromagnetic resonance condition.

Next, the FMR setup utilized within this work to characterize the anisotropies of the MOIF is introduced: A rotatable electromagnet generates a static magnetic field $B_{\text{ext}} = \mu_0 H_{\text{ext}}$ of up to 200 mT. Centered between the pole shoes, as shown in Figure 2.7, a coplanar waveguide (CPW) is positioned that produces a high frequency magnetic field. The sample is placed

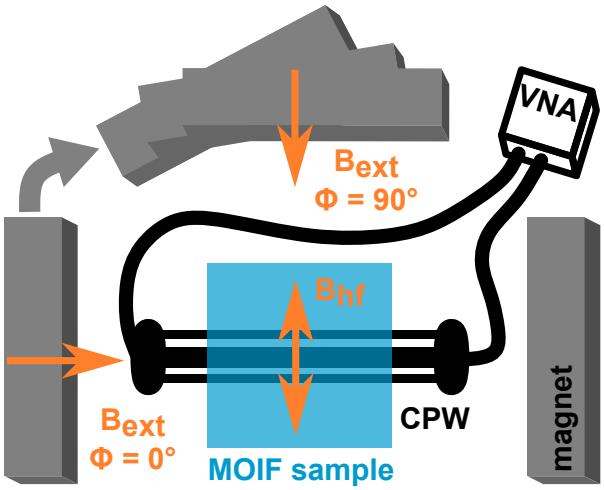

Figure 2.7: Schematic of the FMR setup with a rotatable electromagnet.

on top of the CPW. The frequency of the power applied to the CPW is swept by a vector network analyzer (VNA) in the GHz range. Simultaneously, the VNA measures the absorbed power. The largest absorption indicates the resonance state when all spins in the sample

precess homogeneously with the same frequency. This resonance frequency f_{res}, also known as the uniform FMR mode, is measured for different ϕ-angles of the static magnetic field in the sample plane. The f_{res} vs. ϕ data can be analyzed to calculate the magnetic anisotropies as explained below.

To model the FMR spectra and extract the magnetic anisotropies, the Smit-Beljers-Suhl approach [44, 45] was applied, which relates the FMR frequency $f_{\mathrm{res}} = \omega/2\pi$ of the material to the derivatives of the magnetization and field dependent terms of the free energy function F of the material:

$$\frac{\omega}{\gamma} = \frac{1}{M_S \cdot \sin\theta_0} \cdot \sqrt{\frac{\partial^2 F}{\partial\theta^2} \cdot \frac{\partial^2 F}{\partial\phi^2} - \left(\frac{\partial^2 F}{\partial\theta\partial\phi}\right)^2}, \gamma = \frac{g \cdot \mu_{\mathrm{B}}}{\hbar}. \tag{2.11}$$

Where the derivatives must be taken at the equilibrium magnetization angles θ_0 (to the plane normal) and ϕ_0 (in the plane). The general angle designation is introduced in Figure 2.4. M_S is the saturation magnetization, g is the g-factor and μ_{B} the Bohr magneton. In the MOIF magnetic thin film material, the dominant contributions to F are the demagnetization energy F_{demag} and the crystalline anisotropy energy terms F_{c} (cubic anisotropy), F_{uip} (uniaxial in-plane anisotropy), and F_{uoop} (uniaxial out-of-plane anisotropy). Especially in FMR experiments, also the Zeeman energy F_{zee} has to be taken into account due to the band splitting caused by the applied magnetic field. All contributions are functions of the magnetic field $\boldsymbol{H}$ and the magnetization $\boldsymbol{M}$ vectors. For convenience, both vectors are given in spherical coordinates

$$\boldsymbol{M} = M\left(\sin\theta_{\mathrm{M}} \cdot \cos\phi, \sin\theta_{\mathrm{M}} \cdot \sin\phi, \cos\theta_{\mathrm{M}}\right) \text{ and} \tag{2.12}$$

$$\boldsymbol{H} = H\left(\sin\theta_{\mathrm{H}} \cdot \cos\chi, \sin\theta_{\mathrm{H}} \cdot \sin\chi, \cos\theta_{\mathrm{H}}\right). \tag{2.13}$$

In spherical coordinates the energy contributions take the following forms [39, 46]:

$$\begin{aligned} F_{\mathrm{zee}} = &-\mu_0 \cdot M_{\mathrm{S}} \cdot H \\ &\cdot \left(\cos\theta_{\mathrm{H}} \cdot \cos\theta_{\mathrm{M}} + \sin\theta_{\mathrm{H}} \cdot \sin\theta_{\mathrm{M}} \cdot (\cos\phi \cdot \cos\chi + \sin\phi \cdot \sin\chi)\right) \end{aligned} \tag{2.14}$$

$$F_{\mathrm{demag}} = \frac{1}{2}\mu_0 M_{\mathrm{S}}^2 \cdot \left(N_{\mathrm{z}} \cdot \cos^2\theta_{\mathrm{M}} + N_{\mathrm{x}} \cdot \cos^2\phi \cdot \sin^2\theta_{\mathrm{M}} + N_{\mathrm{y}} \cdot \sin^2\theta_{\mathrm{M}} \cdot \sin^2\phi\right) \tag{2.15}$$

$$F_{\mathrm{uip}} = -K_{\mathrm{uip}} \cdot \sin^2\theta_{\mathrm{M}} \cdot \cos^2(\phi - \phi_{\mathrm{u}}) \tag{2.16}$$

$$F_{\mathrm{uoop}} = -K_{\mathrm{uoop}} \cdot \cos^2\theta_{\mathrm{M}} \tag{2.17}$$

$$F_{\mathrm{c}} = K_{\mathrm{c}} \cdot \sin^2\theta_{\mathrm{M}} - \frac{K_{\mathrm{c}}}{8} \cdot \sin^4\theta_{\mathrm{M}} \cdot \left(7 + \cos(4(\phi - \phi_{\mathrm{c}}))\right) \tag{2.18}$$

Here, the $N_{(x/y/z)}$ are the entries of the demagnetization tensor of the thin film MOIF material in main axis representation and ϕ_u and ϕ_c are the orientation of the uniaxial and cubic anisotropy axes, respectively, in the sample plane. Combining equations Equation 2.11 to Equation 2.18 allows to derive an expression relating the field angle ϕ to the measured FMR frequency as a function of the anisotropy parameters of the material and of its magnetization.

$$\begin{aligned} f_\mathrm{res} =& \frac{\gamma}{2\pi\sqrt{2}\cdot M} \\ & \cdot \Bigg(\Big[3K_\mathrm{c} + 2K_\mathrm{uip} - 4K_\mathrm{uoop} + 2MH\mu_0 + 2M^2\mu_0 \\ & \quad + K_\mathrm{c}\cdot\cos\left(4(\phi-\phi_\mathrm{c})\right) + 2K_\mathrm{uip}\cdot\cos\left(2(\phi-\phi_\mathrm{u})\right) \Big] \\ & \quad \cdot \Big[MH\mu_0 + 2K_\mathrm{c}\cdot\cos\left(4(\phi-\phi_\mathrm{c})\right) + 2K_\mathrm{uip}\cdot\cos\left(2(\phi-\phi_\mathrm{u})\right) \Big] \Bigg)^{1/2} \end{aligned} \tag{2.19}$$

The equation is valid if the magnetization lies in-plane and if the in-plane magnetization component is aligned with the in-plane magnetic field component ($\phi = \chi$). This is approximately the case for the MOIF sample in the described FMR setup with relatively high applied magnetic fields in the plane. Fitting measured data with Equation 2.19 reveals the magnetic anisotropy constants, as presented in subsection 4.2.3. [Reproduced from Manuela Gerken et al 2020 Meas. Sci. Technol. 31 075009 with permission of IOP Publishing.]

2.1.6 Approximation of the sample magnetization structure

In the following, an approach to reconstruct the magnetization structure of a sample from its measured stray field is introduced. An example of a measured stray field distribution is shown in Figure 2.8(a). Here, the z-component of the stray field is plotted because this work focuses on perpendicular magnetized samples. The process works in a similar way with detected Hall voltages or the field value given by the CMOS-MagView XL. It is assumed that areas with opposite magnetization can be distinguished by the sign of the measured signal, here B_z. Thus, areas belonging to a positive (negative) signal, as indicated by the dashed red lines in Figure 2.8, are set to the positive (negative) remanence magnetization $\mu_0 M_\mathrm{R}$ of the sample material. The magnetization $\mu_0 M_\mathrm{R}$ can for example be determined via superconducting quantum interference device (SQUID) measurements. Through this discrimination process, the approximate magnetization structure of a sample can be reconstructed as shown in Figure 2.8(b).

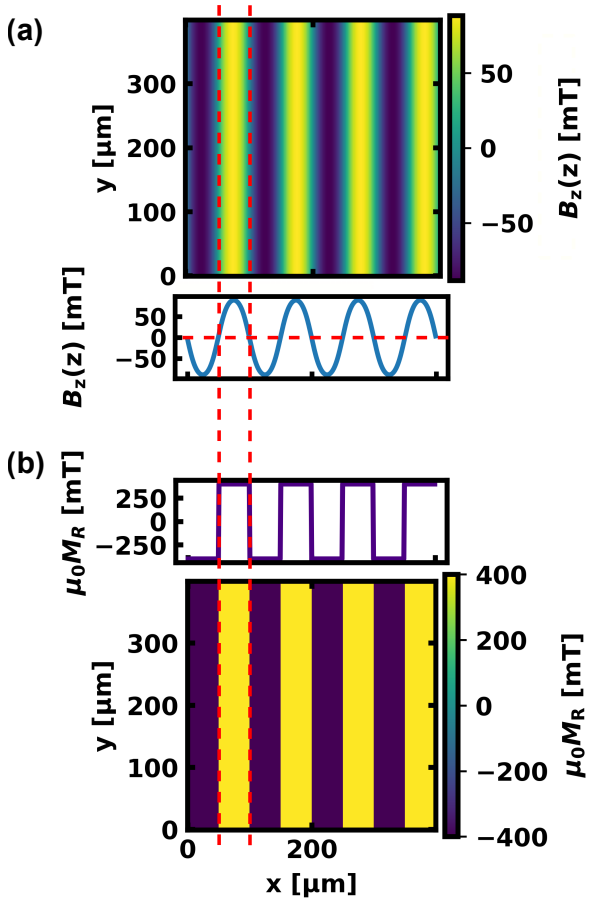

Figure 2.8: Approximation of a sample magnetization distribution from measured stray field data. (a) Distribution of the perpendicular stray field component and the field amplitude for a single line. (b) Magnetization amplitude for a single line and the two-dimensional magnetization distribution of a magnetic scale derived from its stray field.

2.1.7 Stray field calculation with transfer functions

Simulations of sample stray fields are utilized to validate the here developed and calibrated measurement techniques. In the following, a numerically inexpensive simulation approach based on transfer functions (TF) [47, 48] is introduced. More details to this simulation approach are given in Appendix A. The method starts from a given sample magnetization. The magnetization is supposed to be perpendicular to the sample plane and homogeneous over the sample thickness. An inhomogeneous magnetization distribution in the perpendicular direction can be approximated by an interlayering of the sample to thin layers with constant magnetization. The magnetization creates magnetic charges on the sample layer surfaces and interfaces that generate the magnetic stray field. The measurement techniques utilized within this work detect the stray field at discrete points at planes parallel to the sample surface. Therefore, a partial Fourier transformation of only the in-plane coordinates from (x, y, z) to (k_x, k_y, z) can be applied. In the Fourier space, the stray field calculation becomes a simple multiplication by TFs instead of inconvenient integrations and differentiations. The method is applicable if the characterized area and the measurement height are small in comparison to the sample surface area. Otherwise, also edge effects from the sample and the vicinity of the sample influence the detected stray field values. Three steps, which are visualized in Figure 2.9 for an example, have to be executed:

(i) A two-dimensional discrete Fourier transformation (DFT) of the magnetization

$$M(x, y) \Longrightarrow M(\boldsymbol{k}) = \mathcal{F}(M(x, y)), \text{ with } \boldsymbol{k} = (k_x, k_y) \tag{2.20}$$

is performed because the utilized devices measure at discrete sampling points (pixels) in the xy-plane. The DFT of the perpendicular magnetization is calculated by

$$\begin{aligned} M_{\mathrm{z}}(m, n) = &\sum_{p=0}^{N_x-1} \sum_{q=0}^{N_y-1} M_{\mathrm{z}}(p, q) \cdot \mathrm{e}^{-2\pi i \left(\frac{pm}{N_x} + \frac{qn}{N_y}\right)}, \text{ with} \\ &m \in \left\{ -\frac{N_x}{2}, -\left(\frac{N_x}{2} - 1\right), ..., \frac{N_x}{2} - 1 \right\} \text{ and} \\ &n \in \left\{ -\frac{N_y}{2}, -\left(\frac{N_y}{2} - 1\right), ..., \frac{N_y}{2} - 1 \right\} \text{ if } N_x,\ N_y \text{ are even or with} \\ &m \in \left\{ -\frac{N_x - 1}{2}, -\left(\frac{N_x - 1}{2} - 1\right), ..., \frac{N_x - 1}{2} \right\} \text{ and} \\ &n \in \left\{ -\frac{N_y - 1}{2}, -\left(\frac{N_y - 1}{2} - 1\right), ..., \frac{N_y - 1}{2} \right\} \text{ if } N_x,\ N_y \text{ are odd.} \end{aligned} \tag{2.21}$$

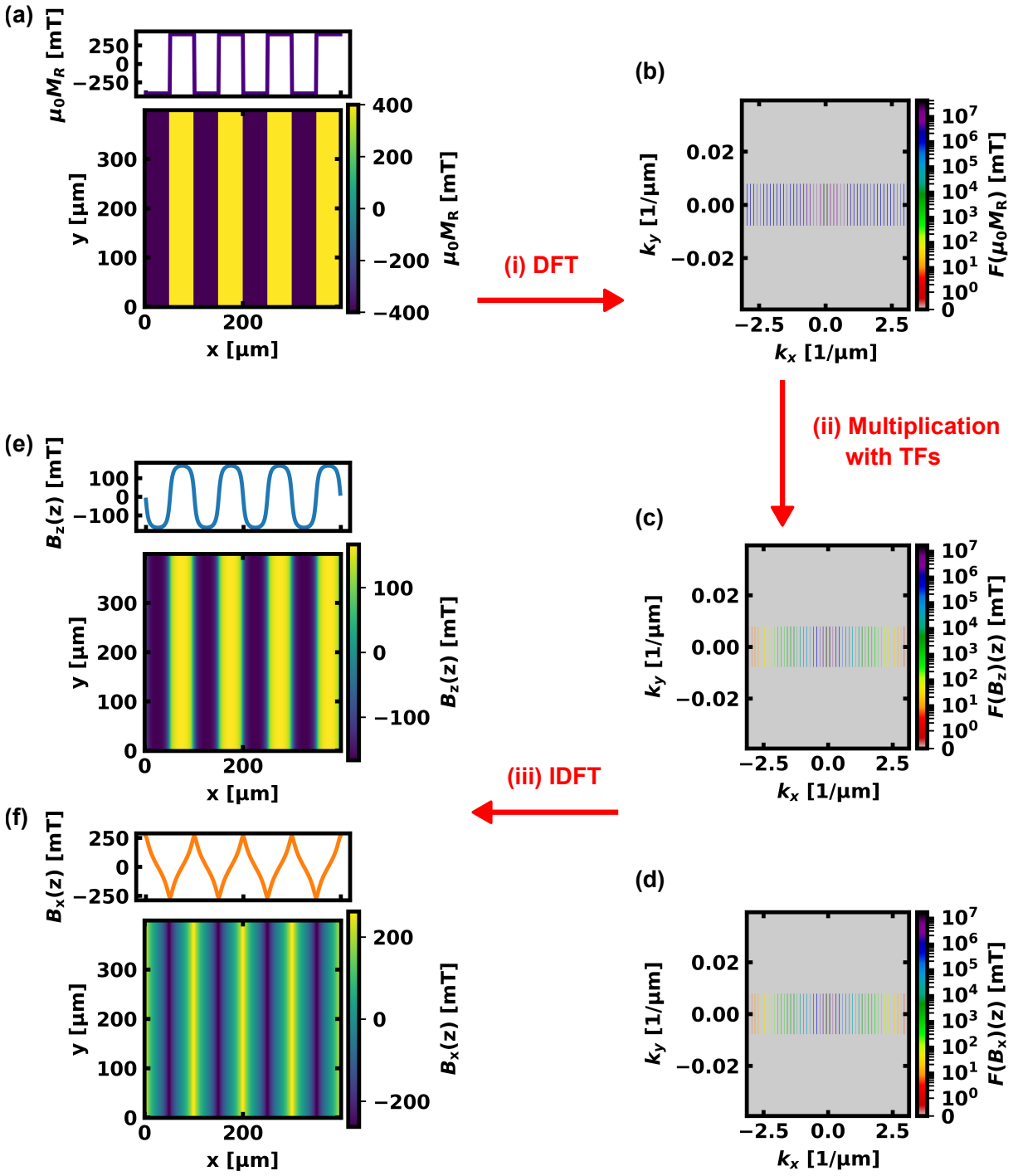

Figure 2.9: Stray field simulation process. (a) Perpendicular magnetization distribution of a magnetic sample. (b) Magnetization in Fourier space generated by DFT. (c) and (d) z- and x-component of the stray field in Fourier space at height z calculated by multiplication with TFs. (e) and (f) z- and x- component of the stray field in real space at height $z = 4\,\mu\text{m}$ generated by IDFT.

The relations between physical points and mathematical indices are given by $x = p \cdot \mathrm{d}x$ and $y = q \cdot \mathrm{d}y$ as well as $k_x = \frac{2\pi \cdot m}{N_x \cdot \mathrm{d}x}$ and $k_y = \frac{2\pi \cdot n}{N_y \cdot \mathrm{d}y}$. N_x and N_y are the pixel numbers in x- and y-direction, respectively. Together with the pixel size in real space $\mathrm{d}x \times \mathrm{d}y$ this leads to a pixel size in k-space of $\mathrm{d}k_x \times \mathrm{d}k_y = \frac{2\pi}{N_x \cdot \mathrm{d}x} \times \frac{2\pi}{N_y \cdot \mathrm{d}y}$.

(ii) The stray field components of $\boldsymbol{B} = \mu_0 \boldsymbol{H} = (B_\mathrm{x}, B_\mathrm{y}, B_\mathrm{z})$ in a parallel plane at a distance z above the sample are calculated by a multiplication in Fourier space of $M_\mathrm{z}(\boldsymbol{k})$ with TFs, thereby is $k = |(k_\mathrm{x}, k_\mathrm{y})|$. The TFs contain the sample thickness d dependent field decay.

$$B_\mathrm{x}(\boldsymbol{k}) = \mu_0 M_\mathrm{z}(\boldsymbol{k}) \cdot \frac{(1 - e^{-kd})e^{-kz}}{2} \cdot \frac{-ik_\mathrm{x}}{k} \tag{2.22}$$

$$B_\mathrm{y}(\boldsymbol{k}) = \mu_0 M_\mathrm{z}(\boldsymbol{k}) \cdot \frac{(1 - e^{-kd})e^{-kz}}{2} \cdot \frac{-ik_\mathrm{y}}{k} \tag{2.23}$$

$$B_\mathrm{z}(\boldsymbol{k}) = \mu_0 M_\mathrm{z}(\boldsymbol{k}) \cdot \frac{(1 - e^{-kd})e^{-kz}}{2} \tag{2.24}$$

(iii) The magnetic stray field in real space is recovered by the inverse DFT.

$$B(\boldsymbol{k}, z) \Longrightarrow B(x, y, z) = \mathcal{F}^{-1}(B(\boldsymbol{k}, z)) \tag{2.25}$$

This is mathematically performed by

$$B(p, q) = \frac{1}{N_x \cdot N_y} \cdot \sum_m \sum_n B(m, n) \cdot \mathrm{e}^{2\pi i \left(\frac{pm}{N_x} + \frac{qn}{N_y}\right)}. \tag{2.26}$$

[Reproduced from Manuela Gerken et al 2020 Meas. Sci. Technol. 31 075009 with permission of IOP Publishing.]

With this method, starting from the sample magnetization, the sample stray field can be calculated at all interesting points (x, y, z) above the sample surface by a simple multiplication with TFs in the Fourier space.

This TF simulation approach is also helpful to understand the properties of stray fields of magnetic microstructures. In Figure 2.10 the simulated perpendicular stray field component of a magnetic scale with 50 µm pole size, a 75 µm thick magnetic layer and a remanence magnetization of $\mu_0 M_\mathrm{R} = 400\,\mathrm{mT}$ is plotted at different measurement heights z. For a fixed sensor resolution, which is normally the case for real sensors, the field contrast attenuates with increasing z, as visualized in Figure 2.10 from (e) over (c) to (a). This decrease in measurement resolution is even enhanced by a lower signal to noise ratio for lower field values. The decrease of the field amplitude depends exponentially on the measurement height [1, 2], as shown in Figure 2.11 for the x- and z-component. This behavior is indicated by the

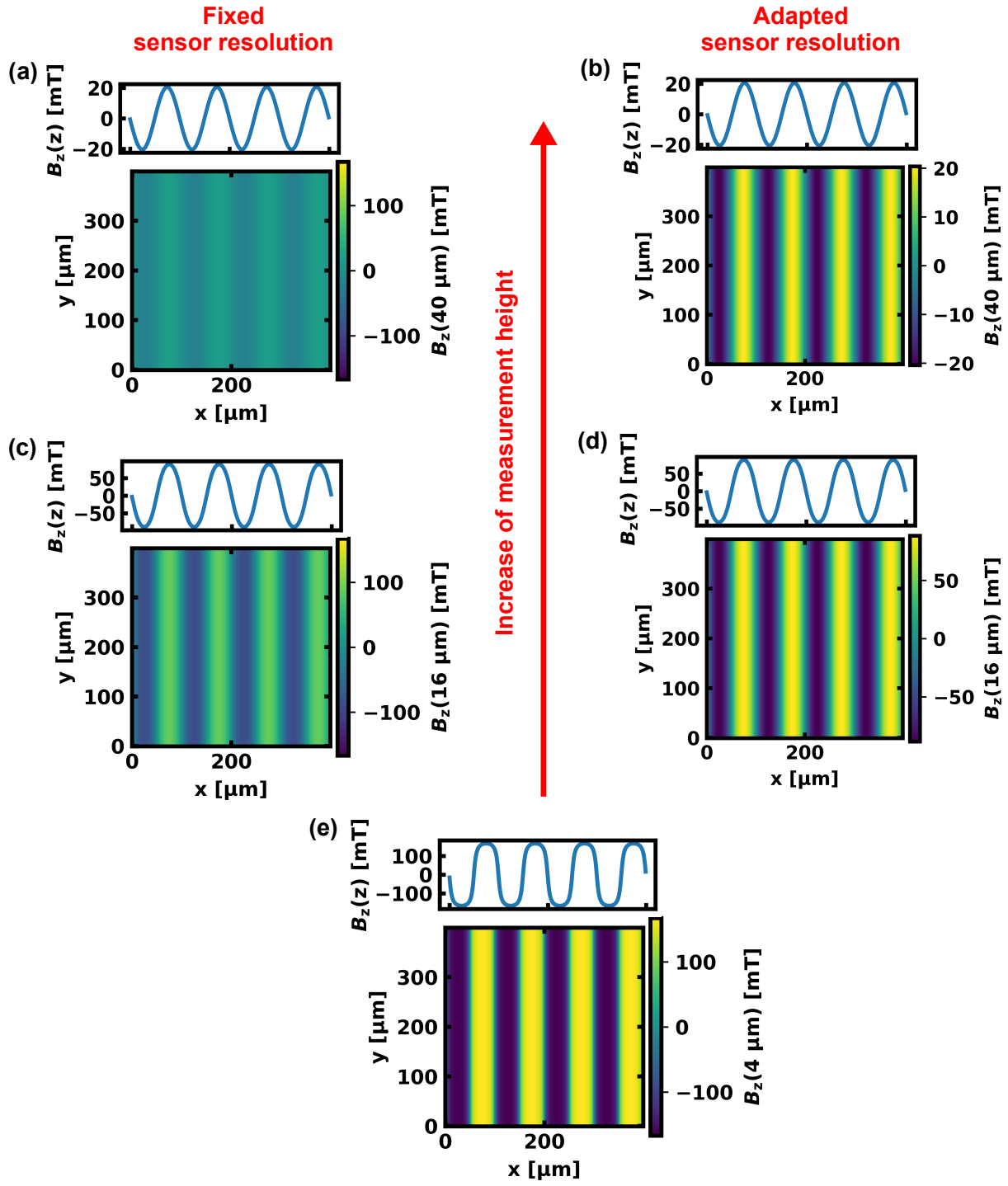

Figure 2.10: Simulated perpendicular stray field component at a distance to the sample surface of (a) and (b) 40 µm, (c) and (d) 16 µm as well as (e) 4 µm. (a) and (c) show the reduced contrast for a fixed sensor resolution, whereas (b) and (d) emphasize the increase of areas with in-plane stray field components with increasing measurement height.

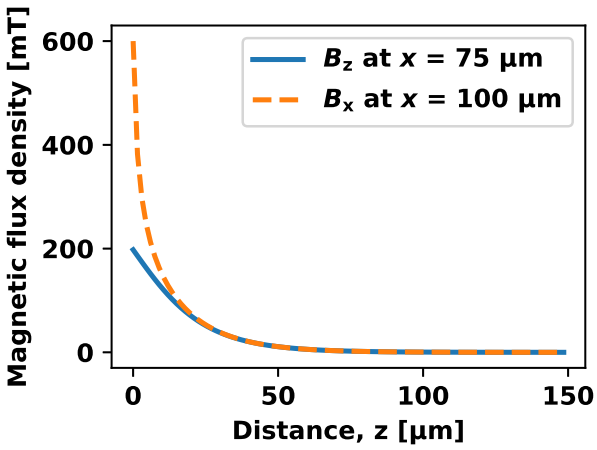

Figure 2.11: Exponential decrease of the field amplitude with increasing measurement height. This example is calculated for a magnetic scale with a remanence magnetization of $\mu_0 M_R = 400\,\mathrm{mT}$, a thickness of $d = 50\,\mu\mathrm{m}$ and a pole width of 50 µm. The z-component is given at the position $x = 75\,\mu\mathrm{m}$ over the center of the positive pole. The x-component is given at $x = 100\,\mu\mathrm{m}$ at the transition from a up to a down magnetized pole.

transfer function $\frac{(1-e^{-kd})e^{-kz}}{2}$ in Equation 2.22 to Equation 2.24. Due to the fact that a two-dimensional DFT was performed for the directions in the plane, the exponential decrease in z-direction remains in real space. Although B_x is overestimated because of the perfectly sharp transition between up and down poles, the general exponential decrease is clearly visible. The origin of this exponentially stray field decrease is explained in more detail in Appendix A. Another property can be demonstrated if a adapted sensor resolution is assumed. For this purpose, the scale bars of the simulation results in Figure 2.10(e), (d) and (b) are always adapted to the present field range. The simulation results show an enlarged area with $B_z = 0$, and thus $B_x \neq 0$, indicated by thicker green bars for an increasing measurement height z. The spatial resolution of the pole transition is decreased with increasing z. Consequently, the resolution of the underlying magnetic structure is better for low measurement heights.

2.1.8 Uncertainty analysis

For a meaningful measurement result it is necessary to also give the uncertainty of the measured values. The uncertainty represents the doubt on the correctness of the result. Only if the measurement uncertainty is given, a comparison of measurement results is possible. To this end, an analysis of the uncertainty budget must be performed. This budget contains the uncertainties of all known influence parameters. A guidance how to

determine the uncertainty budget is introduced by the 'Guide to the expression of uncertainty in measurement' (GUM) [49] and its supplements [50, 51].

In general, quantities X_1, X_2, ..., X_N are combined in a function f that results in the measurand of interest

$$Y = f(X_1, X_2, ..., X_N). \tag{2.27}$$

The estimate of the output y can in the cases considered by the GUM be given by

$$y = \overline{Y} = \frac{1}{n}\sum_{k=1}^{n} Y_k = \frac{1}{n}\sum_{k=1}^{n} f(X_{1,k}, X_{2,k}, ..., X_{N,k}) \tag{2.28}$$

for n individual observations. Especially, if f is not a linear function of X_i, this approach is preferable instead of first building the arithmetic mean x_i from each observation $X_{i,k}$.

$$x_i = \overline{X}_i = \frac{1}{n}\sum_{k=1}^{n} X_{i,k} \tag{2.29}$$

Two different ways of evaluating the standard uncertainty $u(x_i)$ are described. The first, called Type A, uses a statistical approach. The variance σ^2 is calculated by

$$s^2(X_{i,k}) = \frac{1}{n-1}\sum_{j=1}^{n}(X_{i,j} - \overline{X_i})^2. \tag{2.30}$$

This leads to the experimental standard deviation of the mean $s^2(\overline{X}_i)$ and to the Type A standard uncertainty

$$u(x_i) = s(\overline{X}_i) = \frac{s(X_{i,k})}{\sqrt{n}}. \tag{2.31}$$

The second approach, called Type B, is based on scientific judgement and experience. Obtainable knowledge on the potential fluctuation of X_i is utilized to determine its probability density function (PDF). The PDF can show a Gaussian distribution as for Type A or be an interval with constant probability or something in between. The information can be taken from data sheets, calibration certificates or previous measurement data. Also, uncertainties belonging to reference data as well as experiences with the relevant instruments or materials and their behavior can be included. From this, a Type B standard uncertainty $u(x_i)$ is gained.

The uncertainties of the input parameters are merged to receive the combined standard uncertainty of the output estimate.

$$u_c^2(y) = \sum_{i=1}^{N} \left(\frac{\partial f}{\partial x_i} \right)^2 u^2(x_i) + 2 \sum_{i=1}^{N-1} \sum_{j=i+1}^{N} \frac{\partial f}{\partial x_i} \frac{\partial f}{\partial x_j} u(x_i, x_j) \tag{2.32}$$

$u(x_i, x_j)$ is the covariance that determines the correlation of the input quantities. If x_i and x_j are independent, $u(x_i, x_j) = 0$ and the second term of Equation 2.32 disappears.

To report the outcome of a measurement it is not sufficient to give the estimate y and its combined standard uncertainty $u_c(y)$. Additionally, the functional relationship f and the input quantities X_i must be stated. Thus, it is reasonable if a input quantity was overlooked during the determination of the uncertainty budget. Later, for example during a comparison, this can be considered. The GUM is applicable for scalar output quantities and a linear functional relation or if, at least, a linearization of the model is adequate. If this is not the case or the PDF is not Gaussian or a t-distribution, the Monte Carlo method introduced in Supplement 1 is more suitable. For multivariate output quantities, Supplement 2 provides more general instructions in addition to the example in GUM Annex H.3. [49–51]

2.2 Material properties

Below, the properties of the three materials gold, graphene and Bi-REIG, which are used as the sensing materials in this work, are introduced.

2.2.1 Gold

The description of gold (symbol in periodic table: Au) is limited to the facts relevant for Hall sensor application. Thus, mainly the electronic properties are of interest. Gold is a transition metal with a very high conductivity of about $0.452 \cdot 10^6\,\mathrm{S/cm^2}$. However, the large density of conduction electrons leads to a small Hall sensitivity. This drawback is compensated by the following advantages. Gold exhibits an outstanding stable carrier density which causes a low variation in the Hall sensitivity and thus a small uncertainty of the Hall coefficient. The carrier density is, due to the metallic properties, almost not affected by temperature, strain, light or surface contamination. This allows the application of gold Hall sensors on oscillating cantilevers and without any non-transparent encapsulation. Moreover, it is also chemically very stable and shows a low corrosion tendency. The thermal conductivity amounts

to 318 W/(m · K) which ensures a uniform sensor temperature and facilitates heat transfer to the substrate. Another important aspect is the behavior of gold during fabrication. In general, it is robust and widely insensitive to environmental impacts. A desired substrate can be chosen flexibly if a suitable adhesive layer, like titanium, is employed. Electrical connections from the chip to the package can be easily achieved by wire bonding, for example with silver. In summary, gold is a promising choice as the active Hall sensor material. [52]

2.2.2 Graphene

Graphene is, due to its semi-metallic behavior and low carrier density, a remarkable material for Hall sensor applications. The origins of these properties are explained in this subsection. First measurements on graphene exfoliated from graphite were executed by Novoselov and Geim et al. in 2004 [53]. Today preparation of higher quality graphene via chemical vapor deposition or epitaxy is possible. Graphene is a single layer of graphite which makes it a truly two dimensional material. The carbon atoms are ordered in a honeycomb lattice, as shown in Figure 2.12(a). Crystallographically, the structure can be described by the

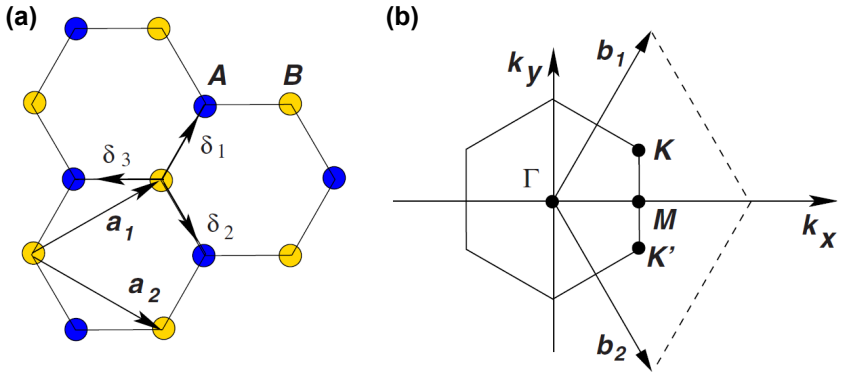

Figure 2.12: (a) Hexagonal lattice structure of graphene. A and B are indicating atoms of the two triangular sublattices. The lattice and nearest-neighbor vectors are given by $\mathbf{a}_{1/2}$ and $\boldsymbol{\delta}_{1/2/3}$, respectively. (b) Brillouin zone of graphene with the reciprocal-lattice vectors $\mathbf{b}_{1/2}$. K and K' are indicating the interesting Dirac points. Adopted from [54].

combination of two equivalent triangular sublattices A and B. Thus, a unit cell consists of two nearest-neighbor atoms with a distance of $a = 0.142\,\text{nm}$. The vectors pointing to the nearest-neighbors are $\boldsymbol{\delta}_{1/2/3}$. The lattice vectors are $\mathbf{a}_{1/2}$. This hexagonal lattice originates from the sp_2-hybridized bonds between the carbon atoms in the plane. This strong σ-bonds are responsible for the mechanical and thermal properties of graphene. Although, the thermal

conductivity depends on the substrate, it is larger than the thermal conductivity of gold. The fourth electron of each carbon atom, not involved in the sp_2 bonds, remains in the p_z orbital oriented perpendicular to the plane. The overlapping of these orbitals forms the weak π bonds. This delocalized electrons in the π bands are the main source of electrical conductivity. The electrical properties of graphene can be better explained by making use of the reciprocal space. It is the Fourier transform of the real space and also known as k-space. The Brillouin zone of graphene is depicted in Figure 2.12(b). The lattice vectors of this primitive cell are $\mathbf{b}_{1/2}$. The most interesting points regarding the electrical conductivity are K and K'. There, the gap between valence and conduction band becomes zero, as visible from the band structure shown in Figure 2.13. The Fermi energy lies directly at the joint

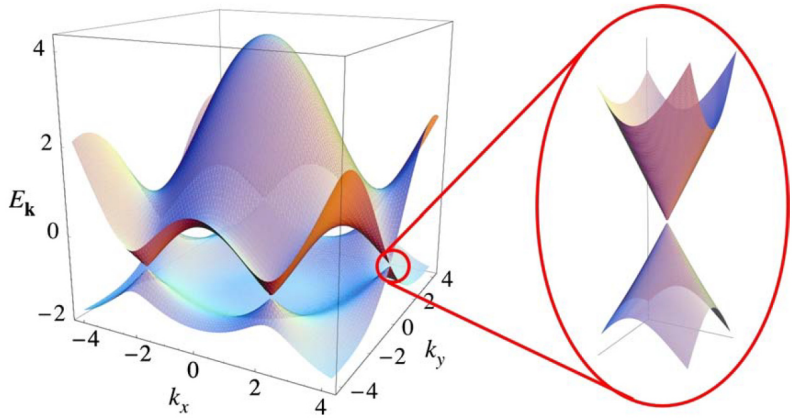

Figure 2.13: Band structure of graphene near the Fermi energy depicted in the reciprocal-space. The zoom shows the conical dispersion at the Dirac points K and K'. From [54].

point of the two cones from valence and conduction band. Thus, for this momentums no energy is needed to lift an electron from the valence band into the conduction band and graphene behaves like a semi-metal. For all other points the band structure equals the band structures of semiconductors or even insulators. At low energies near the K and K' points the dispersion for electrons and holes is linear. The energy degeneracy at the Dirac points K and K' is protected by the symmetry of the two atomic sublattices, which is unique for graphene. [54, 55]

Considering SHPM, graphene sensors offer the highest possible resolution in the z-direction because the sensing layer is atomically thin. The semi-metallic properties offer a good conductivity while the carrier density can be controlled by gating and is usually small and comparable to semiconductors favoring a high Hall sensitivity. Equation 2.2 is also valid for epitaxial graphene grown on silicon carbide (SiC) because after the fabrication process

it is naturally n-doped. As a drawback Graphene has a high chemical sensitivity. The adsorption or desorption of single molecules can be measured as a resistance change. This is disadvantageous for Hall measurements and must be suppressed by a passivation. Still ions on the passivation layer can influence the carrier density and thus the Hall coefficient. Introducing a gate and applying a certain voltage might stabilize the carrier density to a defined value in the n- or p-regime.

2.2.3 Bismuth-substituted rare earth iron garnet

The magneto-optically sensitive material of the MOIF, integrated in the CMOS-MagView XL, is a bismuth-substituted rare earth iron garnet (Bi-REIG). Its structure as well as the relevant magnetic and optic properties are discussed in the following: It has the stoichiometry $(Bi,RE)_3(Fe,Ga)_5O_{12}$ where some of the rare earth elements are replaced by bismuth. Crystalline layers of of Bi-REIG are grown by liquid phase epitaxy on gadolinium gallium garnet ($Gd_3Ga_5O_{12}$) substrates. The lattice structure has a body-centered cubic symmetry with three sublattices and 160 atoms in the unit cell. This rather complicated structure offers lattice sites with space for various ionic radii. This enables the combination of different rare earth elements and substitution with other elements like bismuth leading to a wide range of magnetic, microwave and optical properties. For example, the strength and direction of its magnetic anisotropy can be adjusted. REIGs, in general, possess a low magnetic damping and therefore outstanding spin wave propagation lengths in the centimeter range. Furthermore, Bi-REIG features the largest known Faraday rotation of a few degrees per micrometer, which makes is favorable for quantitative magnetic stray field measurements. [56–58]

3 Scanning probe microscopy with nano- and micro-size Hall sensors

In this chapter the story how to perform SHPM of magnetic microstructures is told. It starts with the fabrication process of nano- and micro-size Hall sensors using uncommon materials, gold and graphene, as the active sensing layers. The subsequent characterization of these Hall sensors includes not only sensitivity measurements but also an evaluation of the reproducibility and sensor stability as well as of the temperature behavior. Before the SHPM measurement of a magnetic scale is presented, the SHPM system is described. The chapter is topped off with an analysis of the uncertainty budget and a verification of the SHPM measurements by comparison to simulation results.

3.1 Fabrication

Hall sensor cross-structures with active square areas from $5 \times 5\,\mu m^2$ down to $50 \times 50\,nm^2$ were fabricated using EBL combined with lift-off and etching techniques. Below, fabrication basics are introduced, then the fabrication processes for gold and graphene sensors are described in detail.

3.1.1 Fabrication basics

Electrical devices, like Hall sensors, are mainly fabricated using thin film technology. Below, the main procedures, applied for the fabrication of gold and graphene based Hall sensors in this work, are explained. The fabrication process consists of several lift-off processes sometimes in combination with an etching step. Details and fabrication parameters are given in Appendix B. In general, a lift-off process contains four main steps which are presented in Figure 3.1. First, a resist that will be transfered into a mask for the final structure is

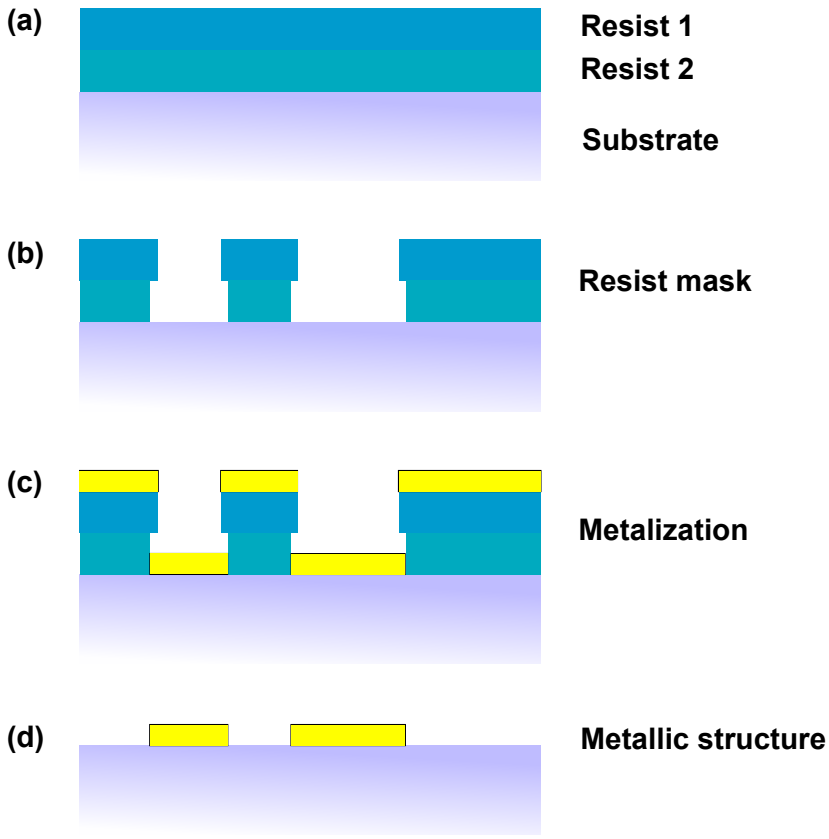

Figure 3.1: Schematic of the lift-off process. (a) Substrate with the two layer resist deposited by spin coating. (b) Resist mask after electron beam lithography and resist development. (c) Structure after metalization by electron beam evaporation. (d) Final metallic structure after lift-off.

deposited. Polymethyl methacrylate (PMMA) resists solved in chlorbenzene or anisole from Allresist GmbH [59, 60] are used here. The PMMA is dropped on a wafer, then the wafer is rotated by a spin coater at a speed of several thousands revolutions per minute. This creates a homogeneously thick PMMA film with a possible thicknesses ranging from tens to hundreds of nanometers. The PMMA resist is then tempered on a hot plate to evaporate a sufficient amount of the solvent to get a solid layer. This procedure is repeated with a second PMMA resist which has a higher concentration of PMMA. The result is shown in Figure 3.1(a). To create the resist mask as shown in Figure 3.1(b) electron beam lithography (EBL) is applied. Here, the system EBPG5200 from Raith GmbH is utilized. The geometry of interest is written with an electron beam into the resist. The beam is generated with an electron gun and accelerated into the direction of the wafer. Electromagnetic lenses focus the beam to a minimal size on the wafer of a few nanometer. A deflection electrode scans the beam over the wafer to write the structures and a blanking electrode suppresses the beam at the spots where no writing is needed. To define the geometry that the beam should write, a

computer aided design program is employed. The electrons of the beam change the chemical structure of the PMMA resist. After the writing process the resist is developed in a suitable solution. For a positive resist, as applied here, the exposed areas are freed from the resist. The bottom resist is, due to its lower molecular weight, more sensitive to the electron beam. Thus, the undercut visible in Figure 3.1(b) is generated. This undercut is important for the actual lift-off step. Now the required material is deposited. Within this work, the metallic layers are evaporated via an electron beam in a vacuum system based on Univex 350 from Oerlikon Leybold. The metals are heated by the electron beam, evaporate and condense on the wafer. The layer constitution after this step is depicted in Figure 3.1(c). Within the final lift-off step, the remaining resist is dissolved in acetone and the metallic layer on top of the resist is lifted. Due to the two layer resist structure with the undercut profile there is no connection between the metallic layer on the wafer and the one on top of the resist. This enables a smooth lift-off. So finally, a metallic layer in the desired geometry is structured on the wafer as shown in Figure 3.1(d). [61–63]

To etch existing layers, for example to structure a graphene layer, the metalization step is replaced by an etching step. Here, a Leybold Z401 system is employed to perform AC oxygen plasma-etching with an oxygen argon gas mixture. The plasma is generated through a high AC voltage. The species of the plasma react with the surface which is supposed to be etched and form volatile products. [64]

After the fabrication it is important to check the geometry and structure size. To this end, a scanning electron microscope (SEM), Supra 40 from Zeiss, was utilized. The operation principle in terms of electron beam generation and scanning is similar to EBL systems. However, for SEM the electron beam is not used to write but to image the structures. The electrons interact with the sample surface and cause characteristic signals like secondary electrons, Auger electrons, backscattered electrons, x-rays, photons and phonons. These signals or part of them, depending on the application, are detected and employed to create an image of the sample. [62] For standard imaging within this thesis usually secondary electron imaging was used.

3.1.2 Gold Hall sensors

To deposit and structure a gold layer into Hall sensors a lift-off process, as explained in subsection 3.1.1, is utilized. First, the substrate, a silicon wafer with 300 nm silicon dioxide, is cleaned using acetone and ultrasonic. Second, two PMMA resists are deposited with the help of a spin coater and tempered on a hot plate. The first resist is more sensitive to the

developer than the second one to guarantee a smooth lift-off. Third, the resist is exposed via EBL, which is operated by Thomas Weimann at PTB, and the Hall cross structure as well as the contact structure is written into the resist. Next, the resist is developed which reveals the Hall sensor shape. Finally, the metallic layers are deposited by electron beam evaporation. 5 nm of titanium serve as an adhesion agent for the gold layer. A gold layer thickness of 30 nm turned out to be an optimal compromise. On the one hand, a 30 nm thick active layer is thick enough to be stable and able to carry a sufficient current. On the other hand, it is thin enough to result in an acceptable Hall coefficient and to keep the field averaging over the sensor thickness as small as possible. The structuring of the active layer is completed by a lift-off in acetone. The contact regions are strengthened with an additional 50 nm thick gold layer, as shown in Figure 3.2(a). To this end, a second fabrications step, similar to

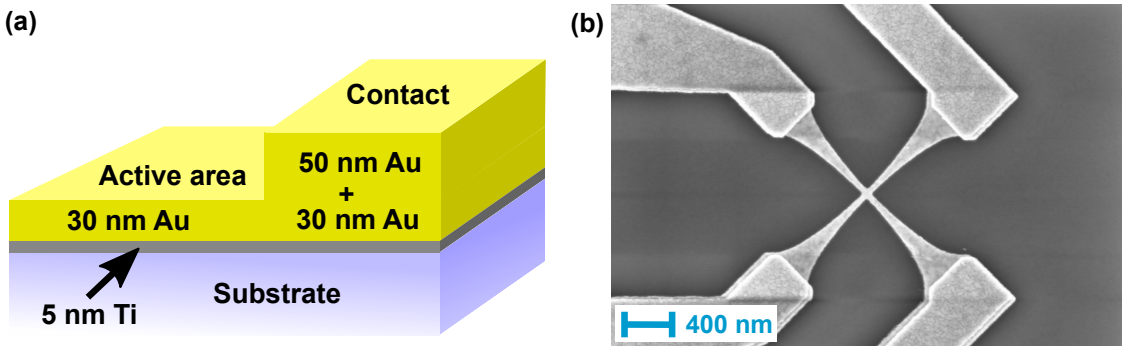

Figure 3.2: (a) Layer structure of gold Hall sensors. (b) SEM image of a 50 nm Hall cross.

the first one, is necessary. The two steps mainly differ from each other by the deposited metallic layers. An SEM image of a $50 \times 50\,\mathrm{nm}^2$ gold cross-shaped Hall sensor is presented in Figure 3.2(b). The smooth edges of the final structure and a nearly perfect alignment of the two fabrication steps are visible.

To enable the integration of Hall sensors into a scanning system a special substrate is used. The substrate consists of a silicon wafer covered on both sides with a 1 µm thick silicon nitride (Si_3N_4) layer deposited by low-pressure chemical vapor deposition. After the fabrication of the Hall sensors, cantilever chips with Hall sensors on the tips of the cantilevers, as depicted in Figure 3.3, are fabricated out of the Si_3N_4 wafer by optical lithography and etching. This cantilever structuring is performed by Aurélie Solignac at CEA Saclay in France. The shape of the cantilever is defined by an aluminum (Al) mask, resistant to the Si_3N_4 final reactive ion etching (RIE). Windows are opened in the Si_3N_4 on the backside by RIE allowing the wet etching of silicon under the cantilever region with potassium hydroxide (KOH). The cantilevers now protrude from windows of 1 µm thick Si_3N_4 and are protected by an Al mask. Cantilevers are then released by performing the final top RIE etching of the Si_3N_4, and the

Al mask is dissolved in a photoresist developer basic solution. The result is presented in Figure 3.3. By careful alignment of the Hall sensor and cantilever fabrication processes, a Hall sensor positioning close to the cantilever tip is possible. The geometrical dimensions are visualized in Figure 3.3(a) and (b). For the 5 µm sensors a minimal distance between the sensor center and triangular cantilever tip of 20 µm and for the 50 nm ones a distance of 2.4 µm can be achieved.

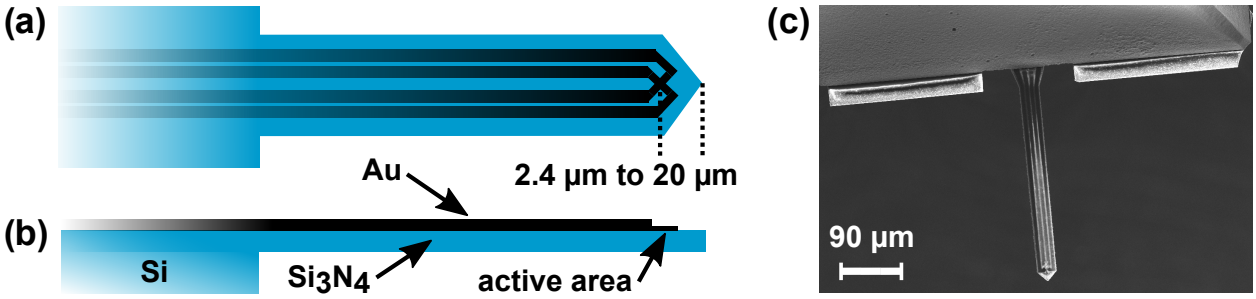

Figure 3.3: (a) Top view schematic of the Hall sensor on the cantilever. The distance between the active area and the triangular tip of the cantilever depends on the size of the sensor, so that the smaller sensors can be positioned closer to the tip. (b) Side view of the cantilever. Dimensions are exaggerated for the sake of visibility (the cantilever is 1 µm thick). (c) SEM image of a cantilever from the backside. The material is so thin that the gold conductors from the front side are visible.

3.1.3 Graphene Hall sensors

The graphene samples were grown by Davood Momeni Pakdehi at PTB on SiC (0001) substrates with a size of $5 \times 10\,\mathrm{mm}^2$ using a so-called polymer-assisted sublimation growth technique [65–67]. The high morphological and electronic homogeneity of the graphene samples allows a scalable realization of Hall sensors on true two-dimensional carbon sheets without bilayer inclusions. Hall sensors were patterned into the graphene with EBL and AC plasma-etching through a resist mask. The fabrication of graphene Hall cross-structures requires five steps. (i) The process starts with an adhering metalization in the contact region. In comparison to the gold Hall sensor fabrication, some additional operations are required. After the PMMA coating a 20 nm thick chromium layer is deposited by electron beam evaporation to avoid charging of the sample during EBL due to the non-conductive SiC substrate. Then the contact regions are written by EBL. Before developing the resist the chromium layer is removed by wet etching. Then, the graphene is etched with AC oxygen plasma-etching to ensure a good adhesion of the metal contacts on the substrate. Finally, a

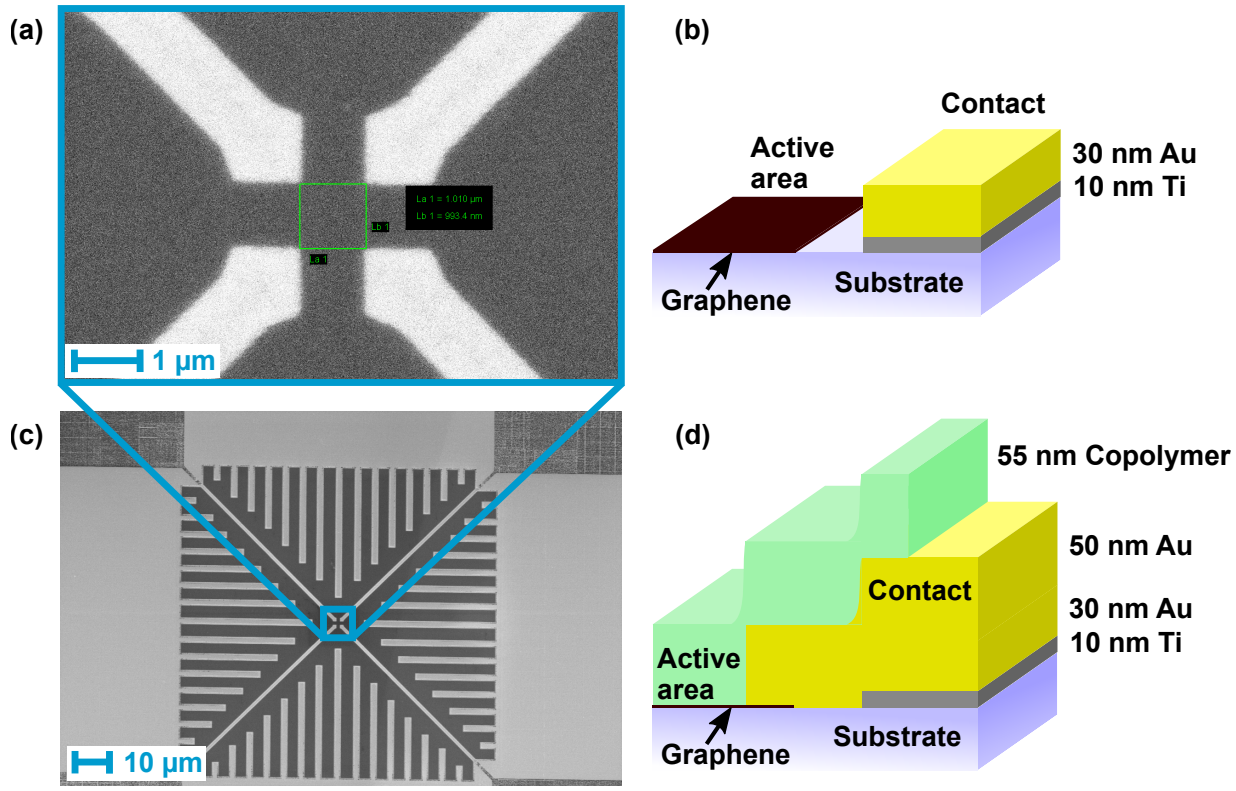

Figure 3.4: (a) SEM image of a 1 µm graphene Hall cross. (b) Layer structure after the third fabrication step. (c) SEM image visualizing the finger-contact structure between the active graphene part and the gold contacts before the deposition of the second gold layer. (d) Layer structure of graphene Hall sensors.

layer stack of 10 nm titanium and 30 nm gold is deposited via electron beam evaporation and lifted in acetone. (ii) Within the next step, the cross-shaped sensing areas of the nano-size Hall sensors are defined. From this step on the above used chromium layer is replaced with a conducting resist that can be deposited via spin coating and dissolved with water. During EBL the resist surrounding the Hall cross, which is the white area in Figure 3.4(a), is exposed. The graphene in this areas is then again etched with AC oxygen plasma-etching and the resist is removed with acetone. (iii) The second step is repeated but this time all areas where no graphene is needed are etched while the nano-size Hall crosses are protected. The result looks like Figure 3.4(b) and (c). The finger-shaped contact structure produces a long contact line between graphene and gold in the plane which enables an efficient charge transfer and reduces the contact resistance. [68–70] (iv) The electrical contact to the graphene is realized by the deposition of a second gold layer. This layer fills the gap between the active graphene region and the adhering metalization and overlaps partly with the graphene. (v) To avoid the environmental influences, especially the rapid change of the carrier density by surface

absorption on the graphene, the graphene sample is encapsulated with 50 nm co-polymer from Kayaku Advanced Materials, Inc. [71]. The final layer stack is visualized in Figure 3.4(d). Note that within this work the graphene sensors were only fabricated on SiC wafer pieces.

3.2 Characterization

Next, the properties of the Hall sensors were analyzed and they were calibrated for SHPM. An electromagnet driven by a Kepco power supply with a pole shoe diameter of 92 mm was used to provide a spatially homogeneous magnetic flux density up to 450 mT at a pole shoe distance of 18.5 mm. The field orientation was perpendicular to the Hall sensor plane. The supply current for the Hall sensors was generated by a Keithley source meter 2400. The Hall voltage was measured with Keithley Nanovoltmeter 2182A. During the Hall sensor calibration, the magnetic flux density was simultaneously measured with a traceably calibrated commercial Hall probe FH55 from Magnet-Physik Dr. Steingroever GmbH. As a consequence, the Hall sensor calibration is traceable to the SI units when considering and listing all uncertainty contributions, as presented in section 3.5. A typical output from the characterization of graphene and gold sensors is presented in Figure 3.5. The Hall voltage was measured as a function of the magnetic flux density B and corrected for the offset. The Hall voltage offset is mainly due to thermo-electric voltages as discussed below.

Sensitivity:
Both sensors show a linear dependence of the Hall voltage V_{Hall} on B as expected from Equation 2.2. For the 5 µm gold Hall sensor operated at 10 mA, the output is in the µV range for B between -150 mT and 150 mT. This leads to a sensitivity S of $3.2\,\mathrm{mV/(AT)} \pm 0.3\,\%$. For the same field range, the Hall voltage of the 500 nm graphene sensor is in the mV range using an operating current of 50 µA. Fitting the data reveals a sensitivity of $1615\,\mathrm{V/(AT)} \pm 0.5\,\%$. The sensitivity of the graphene sensor is six orders of magnitude higher due to the lower carrier density of graphene in comparison to gold. Similar results were observed in the measurements on several other 5 µm large Hall sensors. The mean sensitivity of all gold sensors is 3.1 mV/(AT) with a maximum deviation of 0.2 mV/(AT) within the sensors in this study.

Stability:
Moreover, the time stability as well as fabrication reproducibility of the sensors were investigated. To this end, the 5 µm sensors were frequently characterized within one year and compared with nominally identical sensors from different batches. For the gold sensors, the

long-term stability was very high with a deviation over time below 0.6 %. Graphene sensors showed sensitivity deviations of up to 9.3 % from one day to another. This is most likely to be caused by electrostatic charges attaching and detaching to the co-polymer which act like a gate and thus influence the carrier density in the graphene. Also, the overall variation in sensitivity was larger for graphene sensors ranging from 500 V/(AT) to 1700 V/(AT) depending on the carrier density in the respective graphene material and actual sensor.

Resolution:
Based on the Hall voltage deviation of measured data points from the expected value given by the linear characterization fit

$$\overline{\Delta V}_{\mathrm{Hall}} = \sum_{i=1}^{N} \frac{|V_{\mathrm{Hall}}^{\mathrm{meas}}(B_i) - V_{\mathrm{Hall}}^{\mathrm{fit}}(B_i)|}{N}, \tag{3.1}$$

the resolution is analyzed. Here, N is the number of measured B fields. To gain the resolution, this deviation $\overline{\Delta V}_{\mathrm{Hall}}$ is divided by the sensitivity S.

$$\text{Resolution (in T)} = \frac{\overline{\Delta V}_{\mathrm{Hall}}}{S} \tag{3.2}$$

A typical resolution of 2 mT for gold sensors and 0.45 mT for the graphene sensors was calculated. The resolution includes, besides the sensor properties, also influences and noise contributions from devices and cables in the circuitry.

Noise:
Noise measurements, performed by Felix Nording from Institut für Elektrische Messtechnik und Grundlagen der Elektrotechnik of TU Braunschweig, revealed a detectivity of 60 µT/$\sqrt{\mathrm{Hz}}$ at 1 Hz for a 5 µm graphene Hall cross. The property data of 5 µm large Hall sensors are summarized in Table 3.1. Due to the small resistance of the gold Hall sensors, it was not

Table 3.1: Properties of 5 µm gold and graphene Hall sensors.

Sensor material	**Sensitivity**	**Resolution**	**Detectivity at 1 Hz**	**Long-term deviation**
Gold	2.9 – 3.3 mV/(AT)	2 mT	–	0.6 %
Graphene	500 – 1700 V/(AT)	0.45 mT	60 µT/$\sqrt{\mathrm{Hz}}$	9.3 %

possible to measure their noise characteristics using the given setup. This also means that the noise properties of the electronics have a larger influence on the S/N than the sensor itself.

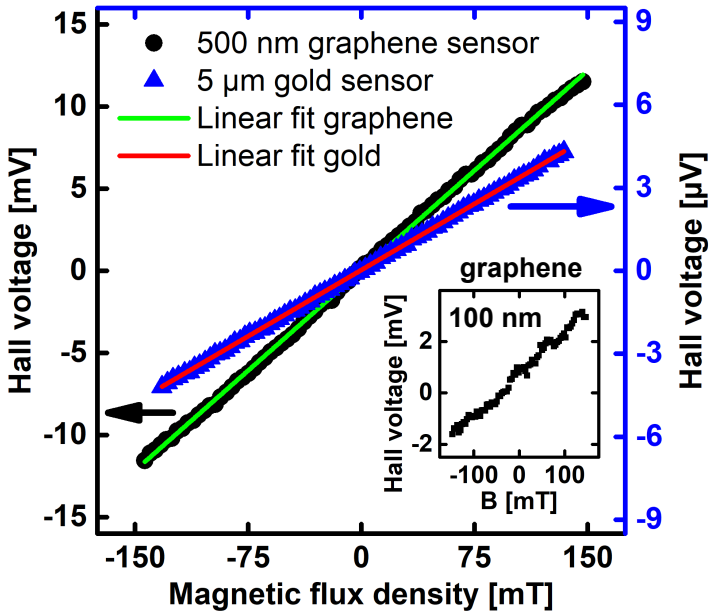

Figure 3.5: Typical calibration curves of gold and graphene Hall sensors. For both measurements, the offset was subtracted from the Hall voltage. The 500 nm graphene Hall sensor was operated at 50 µA and exhibited a sensitivity of 1615 V/(AT) ± 0.5 %. A supply current of 10 mA was used for the 5 µm gold sensor. The sensitivity extracted from the fitted result is 3.2 mV/(AT) ± 0.3 %. The inset shows the calibration result of a 100 nm graphene sensor operated at 10 µA. The sensitivity was determined to 1649 V/(AT) ± 1.17 %.

Sensor size:

With the described measurement equipment, it was possible to calibrate gold sensors with active areas down to 1 µm. For 50 nm gold sensors on cantilevers, the background noise of the setup is larger than the expected Hall voltage of 1.5 nV per 10 mT at the operating current of 50 µA. Because of higher sensitivity and thus larger Hall voltage, graphene sensors with a size of 100 nm still show an overall linear dependence on the applied magnetic flux density, as shown in the inset of Figure 3.5. The resolution is decreased to 8.5 mT presumably because of the growing impact of carrier fluctuations for smaller sensor sizes. Furthermore, the lower current supply leads to smaller Hall voltages, thereby the overall S/N is reduced.

Temperature:

Another important aspect is the temperature T dependence of the Hall sensitivity S and of the Hall voltage offset V_{offset} at $B = 0\,\text{T}$. Therefore, these parameters were characterized in a vector cryostat. The cryostat can be operated at temperatures between -271.95°C and 6°C. A vectorial magnetic field of up to 9 T in the direction perpendicular to the Hall sensor plane can be applied. The results are presented in Figure 3.6(a) and (b) for 5 µm large gold

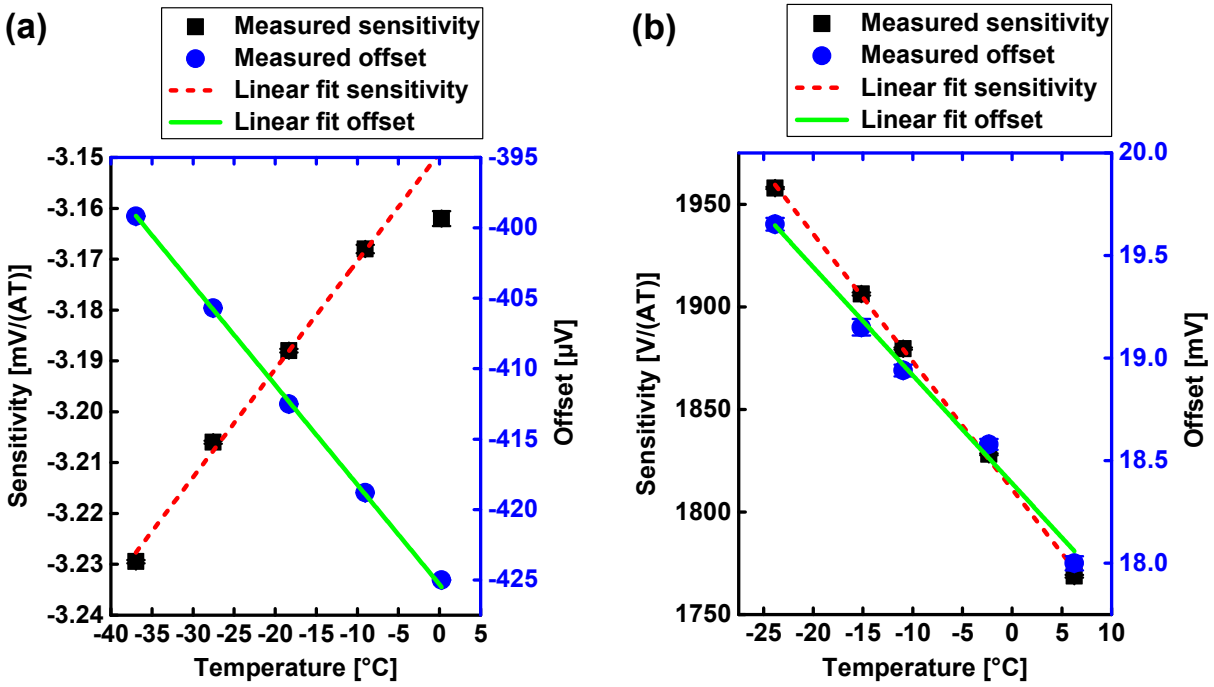

Figure 3.6: Temperature dependence of Hall sensitivity and offset voltage for (a) gold at 5 mA and (b) graphene at 100 µA supply current.

and graphene Hall sensors, respectively. For both materials the sensitivity as well as the Hall voltage offset are plotted as a function of the temperature. Fitting the data reveals the following linear dependencies.

$$S^{\text{gold}}(T) = 2.13\,\frac{\mu\text{V}}{\text{AT}\cdot\,^\circ\text{C}}\cdot T - 3.15\,\frac{\text{mV}}{\text{AT}} \tag{3.3}$$

$$V_{\text{offset}}^{\text{gold}}(T) = -0.71\,\frac{\mu\text{V}}{^\circ\text{C}}\cdot T - 425.32\,\mu\text{V} \tag{3.4}$$

$$S^{\text{graphene}}(T) = -6.22\,\frac{\text{V}}{\text{AT}\cdot\,^\circ\text{C}}\cdot T - 1811.08\,\frac{\text{V}}{\text{AT}} \tag{3.5}$$

$$V_{\text{offset}}^{\text{graphene}}(T) = -52.71\,\frac{\mu\text{V}}{^\circ\text{C}}\cdot T - 18.39\,\text{mV} \tag{3.6}$$

For both materials the sensitivity is decreasing with an increasing temperature which might be due to a higher carrier density and lower mobility. The negative sensitivity values for gold are caused by a not right handed orientation of the current, the magnetic field and the Hall voltage. The main reason for the offset voltage are thermo-electric voltages in the circuitry. This parameter depends on the employed material combinations in a setup and is not specific for the sensor. Nevertheless, these effects have an impact on the measurement uncertainty and are considered by evaluating the relative sensitivity change ΔS_{rel} and the change of the

measured magnetic field ΔB_{meas} induced by a change in the offset voltage $\Delta V_{\mathrm{offset}}$ both for a temperature change ΔT of 2 °C using

$$\Delta S_{\mathrm{rel}}\,(\text{for } \Delta T = 2\,^{\circ}\mathrm{C}) = \frac{slope_{\mathrm{sensitivity}} \cdot 2\,^{\circ}\mathrm{C}}{S(22\,^{\circ}\mathrm{C})} \text{ and} \tag{3.7}$$

$$\Delta B_{\mathrm{meas}}\,(\text{due to } \Delta V_{\mathrm{offset}} \text{ generated by } \Delta T = 2\,^{\circ}\mathrm{C}) = \frac{slope_{\mathrm{offset}} \cdot 2\,^{\circ}\mathrm{C}}{S(22\,^{\circ}\mathrm{C}) \cdot I}. \tag{3.8}$$

This temperature range reflects the typically observed ambient temperature deviations during sensor characterizations. The sensitivities at room temperature were calculated from the fit equations Equation 3.3 and Equation 3.5 as $S^{\mathrm{gold}}(22\,^{\circ}\mathrm{C}) = 3.1\,\mathrm{mV/(AT)}$ and $S^{\mathrm{graphene}}(22\,^{\circ}\mathrm{C}) = 1674\,\mathrm{V/(AT)}$ and agree very well with the previously observed sensitivity values for both materials as given in Table 3.1. The outcome is summarized in Table 3.2. The contribution to sensitivity uncertainty due to temperature fluctuations is smaller than

Table 3.2: Influence of the temperature dependence of Hall sensitivity and offset Hall voltage on sensitivity uncertainty and on the uncertainty of the magnetic flux density measured with the sensors for gold and graphene.

Sensor material	$\Delta S_{\mathrm{rel}}(\Delta T = 2\,^{\circ}\mathrm{C})$	$\Delta B_{\mathrm{meas}}(\Delta T = 2\,^{\circ}\mathrm{C})$
Gold	0.13 %	91.43 mT
Graphene	0.74 %	0.63 mT

the observed long-term instabilities for gold and graphene. Thus, these contributions can be neglected in the first approach. For graphene the influence of changes in the offset voltage have the same size as the resolution estimated from the V_{Hall} vs. B characterization curves and are smaller than the deviations due to long-term fluctuations. However, the impact of Hall voltage offset on the measured Hall voltage must be examined for each setup. For gold the changes of the Hall voltage offset have the same magnitude as the expected Hall signal. This is also indicated by the uncertainty contribution of $\Delta B^{\mathrm{gold}}_{\mathrm{meas}}(\Delta T = 2\,^{\circ}\mathrm{C}) = 91.43\,\mathrm{mT}$. This contribution thus needs to be minimized by carefully measuring the offset voltage and substract it from the Hall measurement data while stabilizing the temperature.

This comparison of gold- and graphene-based Hall sensors emphasizes the benefits and drawbacks of metallic and semi-metallic Hall sensors with the same small active areas and under consideration of the uncertainty budget.

3.3 Scanning probe system

AFM-SHPM is realized by integration of the manufactured cantilever chips with gold Hall sensors into a commercial AFM (Nanoscope IIIa, Dimension 3000 scanner). To this end, the cantilever chips are mounted on a commercial SPM holder, as visualized in Figure 3.7. The

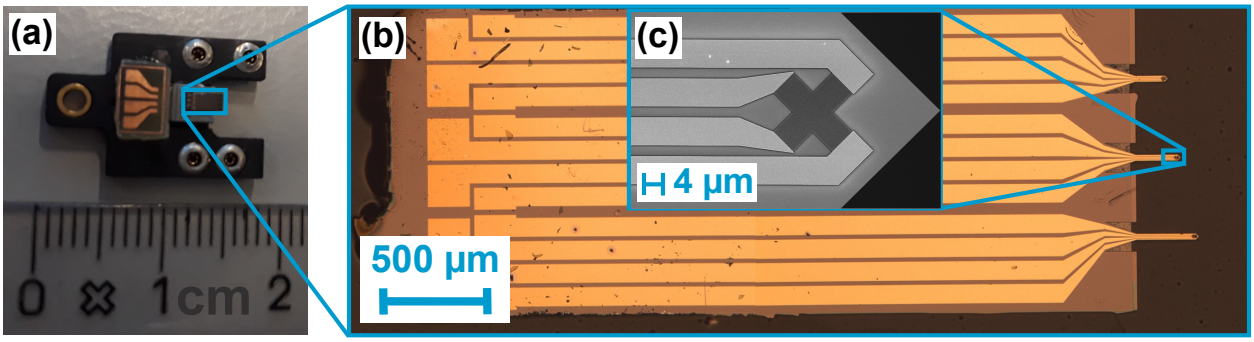

Figure 3.7: Integration of gold Hall sensor on cantilever chip into scanning system.(a) Commercial SPM holder with PCB for electrical connections. (b) Microscopy image of a 3.4 mm × 1.5 mm cantilever chip with three gold Hall sensors for integration into commercial scanning probe microscopy systems. (c) Scanning electron microscopy image of a 5 µm gold Hall cross.

cantilevers have a typical resonance frequency of about 50 kHz and can be used in standard tapping mode operation [72], and thus in close contact with the sample surface. As shown in Figure 3.8, the Hall sensors are positioned at the bottom side of the cantilever and close to its tip to achieve a small distance between the sensor and the sample. This is significant for

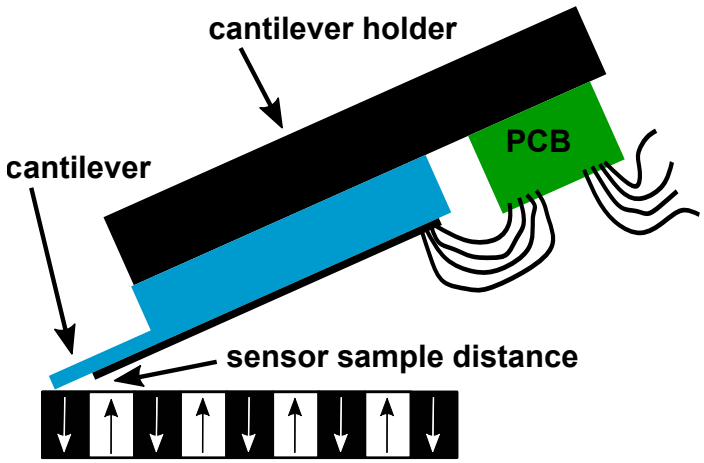

Figure 3.8: Schematic of the AFM-SHPM measurement principle with electrical connections to the sensor and the minimal sensor-sample distance.

improving spatial resolution in measuring micro- and nanostructures due to the fast decay of stray fields with increasing distance to the sample surface. The cantilevers are mounted at an angle of 10° given by the cantilever holder. This leads to minimum measurement heights of 400 nm and 3366 nm for the 50 nm and 5 µm sized sensors, respectively, for an ideal alignment of the Hall sensor on the cantilever. The electrical connection to the Hall sensor is realized by bond wires from the cantilever chip to a printed circuit board (PCB) that is fixed to the cantilever holder. The current source, voltmeter and PCB are connected via soldered cables. To increase the scan area up to the millimeter range, additional piezo tables were added to the setup that allow scanning the sample at a fixed cantilever position. Thus, the sample is moved parallel to the sample surface by x- and y-piezos whereas the measurement height is set by a z-piezo. The Hall sensor was calibrated in the electromagnet before and after the AFM-SHPM measurement.

3.4 SHPM measurement of a magnetic scale

Here, the performance of the AFM-SHPM system with a 5 µm gold Hall sensor is presented. As a test sample, a commercially available magnetic scale SST250HFA04 from Sensitec GmbH was chosen. By the selection of this sample, the operation of AFM-SHPM can be demonstrated on an industrially relevant magnetic sample. The scale is made of a wet pressed strontium ferrite with a remanence magnetization of $\mu_0 M_\mathrm{R} = 395\,\mathrm{mT}$. The material was magnetized into alternating up and down magnetized stripes with a nominal width of 250 µm and several millimeters length. The surface texture of the sample shows a granular structure. The results of a roughness analysis of the sample surface are given in Figure 3.9. The mean deviation from the averaged sample surface is 13 µm and the maximum deviation is 60 µm. Figure 3.10 displays the results of AFM-SHPM line scans on the scale with the 5 µm gold Hall sensor that has a sensitivity of $2.3\,\mathrm{mV/(AT)} \pm 13\,\%$, measured under an applied operating current of 1 mA. Line scans with ten repetitions each were performed at seven different measurement heights. For each height the calculated magnetic flux density is plotted over the position in x-direction. The curves are shifted for 100 mT each for better visibility. The closest line scan to the sample was attained in the tapping mode and thus followed the sample topography at a distance of approximately 4 µm as given by the sensor cantilever geometry. This distance is slightly larger than the above stated minimum distance of 3.366 µm for 5 µm gold Hall sensors because this sensor was positioned 2 µm further away from the triangular cantilever tip. Different distances to the cantilver tip were tried for test reasons. The AFM head in tapping mode has a limited range to adjust the measurement

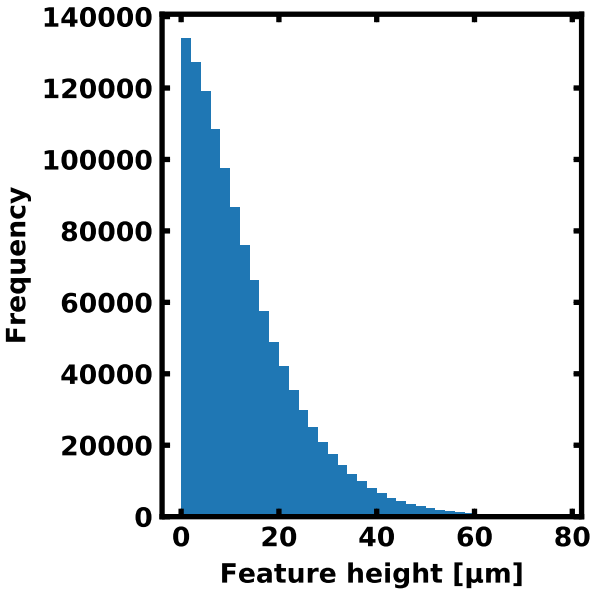

Figure 3.9: Histogram indicating the roughness of the magnetic scale SST250HFA04. The averaged sample surface is located at 0 µm. The frequency of sample features or dust particles over this averaged sample surface height is plotted.

height to stay in contact with the sample surface. The sample, characterized here, has a granular structure and thereby shows height variations of mainly 13 µm and locally tilted surface areas. Furthermore, presumably the sample is not positioned perfectly horizontal. A angular misalignment between the sample and the sensor leads to an increase or decrease in the sensor-sample distance. Over the measurement path of 2 mm even a small misalignment results in a distance variation that is not capable by the AFM head. Therefore, during the measurement in tapping mode, the z-piezo table was utilized to keep the sensor-sample distance in a range that is controllable by the AFM head. The scans for larger measurement heights were carried out at fixed heights ranging from 19 µm to 169 µm (with 30 µm intervals) by moving the sample with a 3-axis piezo scanning system and fixed sensor position. The uncertainty of these measurement heights was estimated to ±15 µm due to the roughness of the sample and thus an uncertainty of the zero plane position and the uncertainty of the z-piezo calibration for the relation between the travel length and the steps set in the software. All measurements were performed at a scan speed of 50.5 µm/s. 400 points were measured per line with an averaging time of 20 ms. All plots in Figure 3.10 show the expected 500 µm periodicity of the scale. Also, the expected decay of the stray field amplitude with increasing distance to the sample is clearly visible. Whereas at a height of 4 µm the mean amplitude over the poles is 102 mT, it is decreased to 54 mT at a measurement height of 79 µm and a magnetic flux density of only 32 mT over the pole centers is left in a height of 169 µm.

This decrease is further analyzed and compared to simulation results in section 3.6. The measurement data from the scan in tapping mode at a measurement height of 4 µm shows large variations. In contrast to the other measurement heights, here the scan follows the sample topography and thus the overall surface texture and tilted surface region influence the measurement result. To analyze this geometrical effect, the SHPM data of forward and backward line scans are presented in Figure 3.11. The forward line scan is identical to the

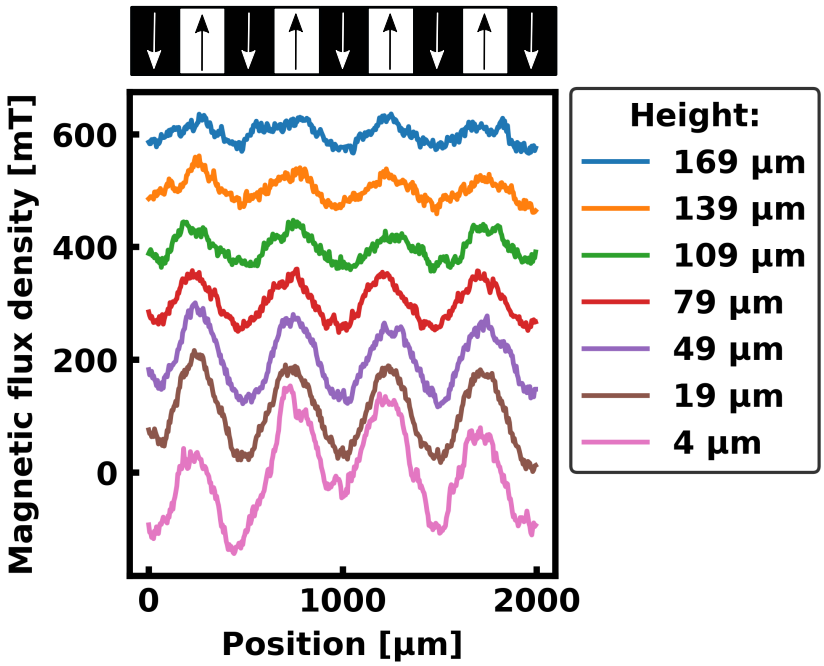

Figure 3.10: Height dependent SHPM of a magnetic scale with 250 µm pole width is shown. A 5 µm × 5 µm gold Hall sensor scanned one line of the sample 10 times for each height. The measurement at 4 µm was performed in tapping mode so that the cantilever tip was in contact with the sample surface. Data from the different measurement heights were shifted for 100 mT each to avoid overlapping.

one in Figure 3.10 where all data result from forward line scans. By comparing the forward and backward line scan a complementary behavior becomes visible. Thus, the variations origin from geometrical relation between the sensor and the sample surface. This artifacts can be eliminated by averaging over the forward and backward data as shown in Figure 3.11. For the averaged signal the large variations disappear. Furthermore, cantilever and sensor proved to be very robust, allowing the characterization of rather rough samples, as demonstrated in this study.

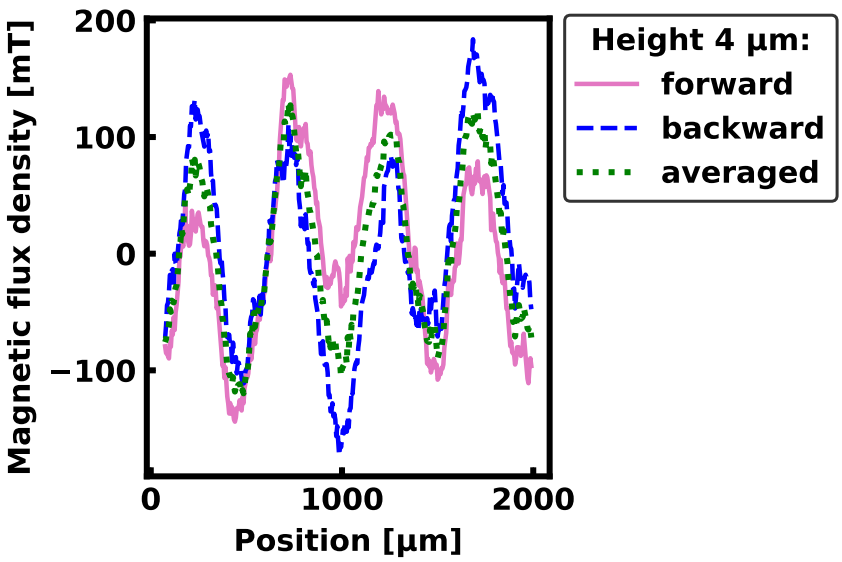

Figure 3.11: SHPM results in tapping mode leading to an averaged measurement height of 4 µm. The data of the forward and backward line scan as well as the average of both direction scans are depicted.

3.5 Uncertainty budget

A traceable calibrated scanning Hall sensor measurement obligatorily requires an analysis of all contributions of the entire scanning and read-out process to the uncertainty and a statement of their values. Five major contributions entering into the net measurement uncertainty are: (i) The Hall sensor itself, where its stability, sensitivity, offset, temperature dependence and noise must be considered. (ii) The Hall sensor calibration via the electromagnets magnetic field homogeneity, stability and repeatability. (iii) The Hall sensor driving and read-out electronics, including the stability of the current source and the voltmeter noise as well as thermoelectric voltages. (iv) The positioning accuracy of the scanning system. (v) Influences of the sensor on the sample, for example in terms of the magnetic stray field generated by the supply current.

The multiplicity of uncertainty sources and the fact that a standard uncertainty analysis is not sufficient for linear regression tasks [73] as used in the Hall sensor calibration, rule out a conventional uncertainty propagation calculation. Therefore, the uncertainties of the main contributions were analyzed separately to evaluate their impact on the measurement: By repeated sensor calibrations of the sensor utilized in the SHPM measurements and statistical analysis of the results, a calibration uncertainty for the sensor sensitivity of 13 % was found. The uncertainty includes properties of the Hall sensor (i), the applied magnetic flux density (ii)

and contributions from the electronic components (iii). The characterization of several gold sensors, as presented in section 3.2, leads to the expectation of lower sensitivity uncertainties than 13 % for the gold sensors in general. Considering the scanning system mainly two uncertainties are important: The uncertainty of the measured magnetic flux density and the positioning uncertainty. The magnetic flux density uncertainty of the scanning system was evaluated by the doubled standard deviation of the mean from ten repeated line scans. The data of the line scans was corrected for drifts by offset subtraction. Hereby, the uncertainty was determined to 7 mT. It includes properties of the Hall sensor (i) as well as contributions from the electronic components (iii). The different measurement heights were realized by an additional z-piezo. The calibration uncertainty of this piezo must be combined with the uncertainty to determine the position of the initial plane of 0 µm measurement height on the rough sample surface. Thus, the uncertainty of the measurement height was determined to (iv) 15 µm. The stray field produced by the sensor supply current at the sample surface (v) was estimated with the help of Biot-Savart law to 0.25 mT. This has thus practically no influence on the sample characterized here and is negligible for many other applications. Combining all contributions leads to a magnetic flux density uncertainty of $\pm$(7 mT + 13 %) for the SHPM and a measurement height uncertainty of $\pm$15 µm for all scans except the scan in tapping mode.

3.6 Verification by comparison to simulation

Here, two modeling approaches are presented to validate the measurement procedure. The first one uses a Fourier transform method to calculate the z-component B_z of the stray field produced by the magnetic scale as discussed in subsection 2.1.7. Assuming that the sample is perfectly parallel to the Hall sensor surface and neglecting the 10° cantilever tilt, the Hall sensor response is mainly dominated by the perpendicular magnetic field component. From now on, this will be called the perpendicular or z-component in contrast to the in-plane components of the field lying parallel to the sample surface. The calculated field profile is then compared to the experimental one, which is derived from the measured Hall voltage as $B = (V_{\mathrm{Hall}} \cdot n \cdot e \cdot t)/I$ after the application of offset corrections. The offset was determined by calculating the mean of each line scan. This mean was then subtracted from each measured Hall voltage before the averaging over all ten line scans was done.

In the following, the details of the stray field simulation procedure are described. To simulate the perpendicular stray field component, the underlying sample magnetization has to be known. To this end, the magnetization is guessed from the measured Hall signal based on

the following assumptions: (i) The transition between up and down magnetized poles can be found at zero crossings of the Hall signal after an offset and drift correction. Offset and drift were ascertained by a sinusoidal fit of the data allowing for an offset and an additional linear slope. (ii) From this the magnetization pattern of the scale can be found by a discrimination between areas with positive and negative Hall voltages, as explained in subsection 2.1.6. (iii) Areas with $+V_{\mathrm{Hall}}$ ($-V_{\mathrm{Hall}}$) are assigned a purely perpendicular and, over the thickness, homogeneous remanence magnetization of $+M_{\mathrm{R}}$ ($-M_{\mathrm{R}}$). To account for the pole writing process, the step-like transitions, as for example shown in Figure 2.8(b), are then additionally smoothed assuming a transition width of 50 µm as visualized in Figure 3.12(a) by the blue dashed line. The figure also shows the position dependent magnetic flux density as measured

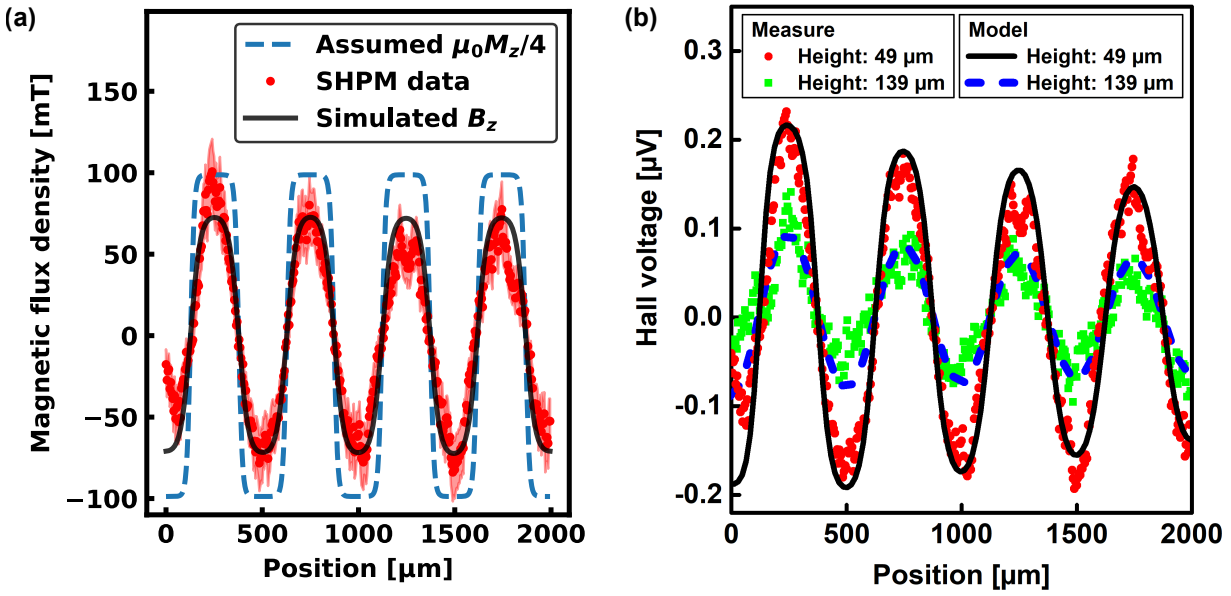

Figure 3.12: (a) Traceable SHPM data with uncertainty budget of scale SST250HFA04 at a measurement height of 49 µm compared to simulated stray field values from the assumed magnetization distribution. (b) Comparison of experimental and calculated Hall voltage signal for measurement heights of 49 µm and 139 µm. The calculation is made with the second modeling approach, introducing an angular misalignment of about 1° between the magnetic sample and the Hall device to explain the drift during scanning.

by AFM-SHPM and simulated. For the stray field simulation, the TF approach introduced in subsection 2.1.7 was pursued due to its numerical simplicity. The calculation of the stray field above the perpendicular magnetization distribution of the sample was performed in Fourier space using Equation 2.24. The stray field of the scale at measurement height z was calculated for a magnetic layer with an assumed thickness of $d = 75\,\mu\mathrm{m}$. Similarly, the

impact of the finite sensor dimensions might be considered by introducing a multiplication by an appropriate sensor sensitivity TF. However, for the relatively slowly varying field of the scale with 250 µm pole width and an only 30 nm thick sensor, this is expected to have a minor impact and was therefore neglected. Inverse discrete Fourier transformation was used to obtain the value of the perpendicular component plotted as black line in Figure 3.12(a) for each AFM-SHPM measured point in real space.

A good agreement between the measured stray field and simulated data was obtained, giving evidence of the validity of the measured quantitative magnetic field distribution, as shown exemplarily in Figure 3.12(a) for the sensor-sample distance of 49 µm. The simulation strongly confirms the measurement results in terms of maximum and minimum magnetic flux density as well as spatial periodicity.

However, the drift and slight decrease in amplitude with position cannot be explained by the stray field results of this first simulation approach. One reason would be an unstable temperature during the measurement and thus a drift of the offset voltage. Another explanation would be an angular misalignment of the sample if it is not flat or placed perfectly horizontal on the table. Such, that the scan is not perfectly parallel to the average sample surface.

To consider these possible influence factors, a second modeling approach was implemented by Alessandra Manzin from INRIM in Italy. Here, the Hall voltage signal due to magnetic scale scanning is numerically calculated, considering an angular misalignment of about 1° of the sample surface to the horizontal plane in addition to the angle of 10° between the magnetic sample and the Hall device given by the scanning setup. Furthermore, the electrical potential over the sensor geometry is analyzed in contrast to the approach above where the sensor is assumed punctual. The results are presented in Figure 3.12(b). The spatial distribution of the electric potential ϕ within the sensor is derived from the finite element solution [74] of the following equation

$$\nabla \cdot [\ddot{\sigma}(\boldsymbol{r}) \cdot \nabla\phi(\boldsymbol{r})] = 0, \tag{3.9}$$

where $\ddot{\sigma}(\boldsymbol{r})$ is the conductivity tensor

$$\ddot{\sigma}(\boldsymbol{r}) = \frac{\mu n e}{1 + [\mu B_\perp(\boldsymbol{r})]^2} \cdot \begin{bmatrix} 1 & \mu B_\perp(\boldsymbol{r}) \\ -\mu B_\perp(\boldsymbol{r}) & 1 \end{bmatrix}. \tag{3.10}$$

μ is the electron mobility, assumed equal to $8.7 \cdot 10^{-4}\,\mathrm{m^2/(Vs)}$ from 4-point resistance measurement and $n = 1.92 \cdot 10^{21}\,\mathrm{m^{-2}}$. $B_\perp$ is the component of the stray field from the scale below that is orthogonal to the sensor plane. This also regards the components of B parallel

to the sample surface, due to the relative angular sensor-sample orientation of 10° given by the scanning setup. Boundary conditions for the electrical contacts for current supply and Hall voltage measurement as well as for insulating sample boundaries are considered. The stray field of the scale, which is discretized in N 10 µm size hexahedra with imposed uniform magnetization, is calculated as

$$\boldsymbol{B}(\boldsymbol{r}) = \frac{\mu_0}{4\pi} \cdot \sum_{e=1}^{N} \int_{\partial\Omega_\mathrm{e}} \boldsymbol{M}(\boldsymbol{r}_\mathrm{e}) \cdot \boldsymbol{n}_\mathrm{e} \frac{(\boldsymbol{r} - \boldsymbol{r}_\mathrm{e})}{||\boldsymbol{r} - \boldsymbol{r}_\mathrm{e}||^3} \,\mathrm{d}s, \tag{3.11}$$

where $\partial\Omega_\mathrm{e}$ is the surface of the e-th hexahedron having normal unit vector $\boldsymbol{n}_\mathrm{e}$ and barycentre with vector position $\boldsymbol{r}_\mathrm{e}$ [75]. The drift effect in the measured Hall voltage signal is well reconstructed by the numerical results, which also support the validity of the linear dependence of V_Hall on B for all the scanning points, despite the finite sensor size due to the large width of the pole scale with respect to the Hall cross size. The agreement with experimental results is highlighted in Figure 3.12(b) for an average sensor-sample distance of 49 µm and 139 µm. The peaks reduce in amplitude during scanning, as a consequence of the increase in the sensor-sample distance due to the small assumed tilt of 1°.

For further verification, the behavior of the stray field with an increasing distance to the sample surface, as shown in Figure 3.10, was quantitatively analyzed. To this end, the maximum measured stray field amplitudes over the poles for each measurement height were compared in Figure 3.13 with the values expected from simulations using Equation 2.24 and Equation 2.25 from the first simulation approach with variable z. Here, the exponential field decrease with an increasing sensor-sample distance is clearly visible.

This behavior is explained in Appendix A and can be summarized by Equation 2.24 for the perpendicular field component and the fact that the two-dimensional IDFT is performed for x and y, the plane parallel to the sample surface. Thus, the behavior in z-direction remains constant in Fourier and real space. To illustrate the exponential dependence Equation 2.24 is given for the dominant k-vector $(k_x, k_y) = (\frac{2\pi \cdot m}{N_x \cdot \mathrm{d}x}, 0) = (0.012, 0)$, here with $m = 4$, $n = 0$, $N_x = 400$ and $\mathrm{d}x = 5\,\mu\mathrm{m}$.

$$B_z((0.012, 0), z) = 0.297 \cdot \mathrm{e}^{-0.012 \cdot z} \tag{3.12}$$

For other k-vectors the prefactors will change, but the general exponential behavior remains. The Fourier transform of B_z for all k_x-components and $k_y = 0$ at a measurement height of 4 µm is plotted in Figure 3.14(a). For all other k_y-components B_z is zero due to the shape of the magnetization in form of stripes. The Fourier transform of B_z is largest at the dominant

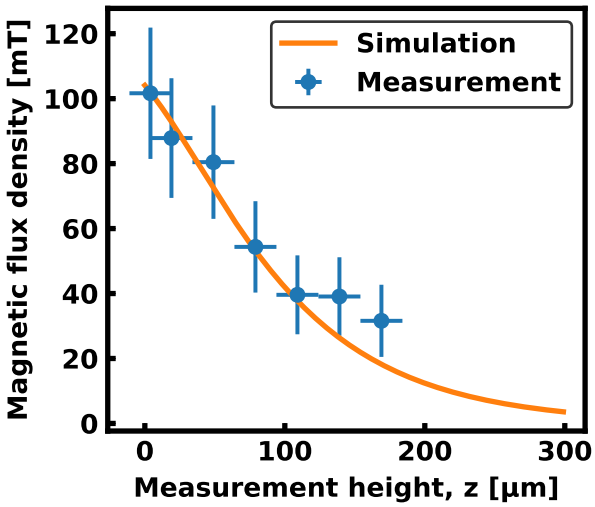

Figure 3.13: Simulated stray field decay with increasing measurement height over the middle of a pole. The data points are generated from the measurements shown in Figure 3.10 by averaging the absolute values of the three minima and four maxima.

k-vectors $(k_x, k_y) = (0.012, 0)$ and $(k_x, k_y) = (-0.012, 0)$ belonging to the fundamental sine function with 500 µm periodicity. This is the periodicity of the rectangular scale magnetization. A faster decay of $B(\boldsymbol{k}, z)$ at higher k-vectors with increasing z is indicated by comparing Figure 3.14(a) with Figure 3.14(b) and (c).

For the two largest measurement heights, shown in Figure 3.13, and corresponding two lowest expected magnetic flux densities, systematic uncertainties from evaluating the extrema have a more significant influence on the result due to an enlarged contribution of noise. However, for all measurements, the simulation result overlaps with the uncertainty squares of the data points. More details about the uncertainty range were given in section 3.5. From these results, the validity of the quantitative AFM-SHPM method using a gold sensor is concluded.

3.7 Conclusion SHPM

In summary, Si_3N_4 based AFM cantilevers equipped with micro and nano-scale gold Hall sensors were fabricated, which facilitate accurate traceably calibrated AFM-SHPM at room temperature. For this purpose, the sensors were integrated into a commercial AFM. The measurement data were in good agreement with simulation results which underlines the reliability of the presented approach. The gold sensors exhibit a sensitivity of 3.2 mV/(AT) with high long-term stability. Also, Hall sensors out of epitaxial, zero-band gap, semi-metallic

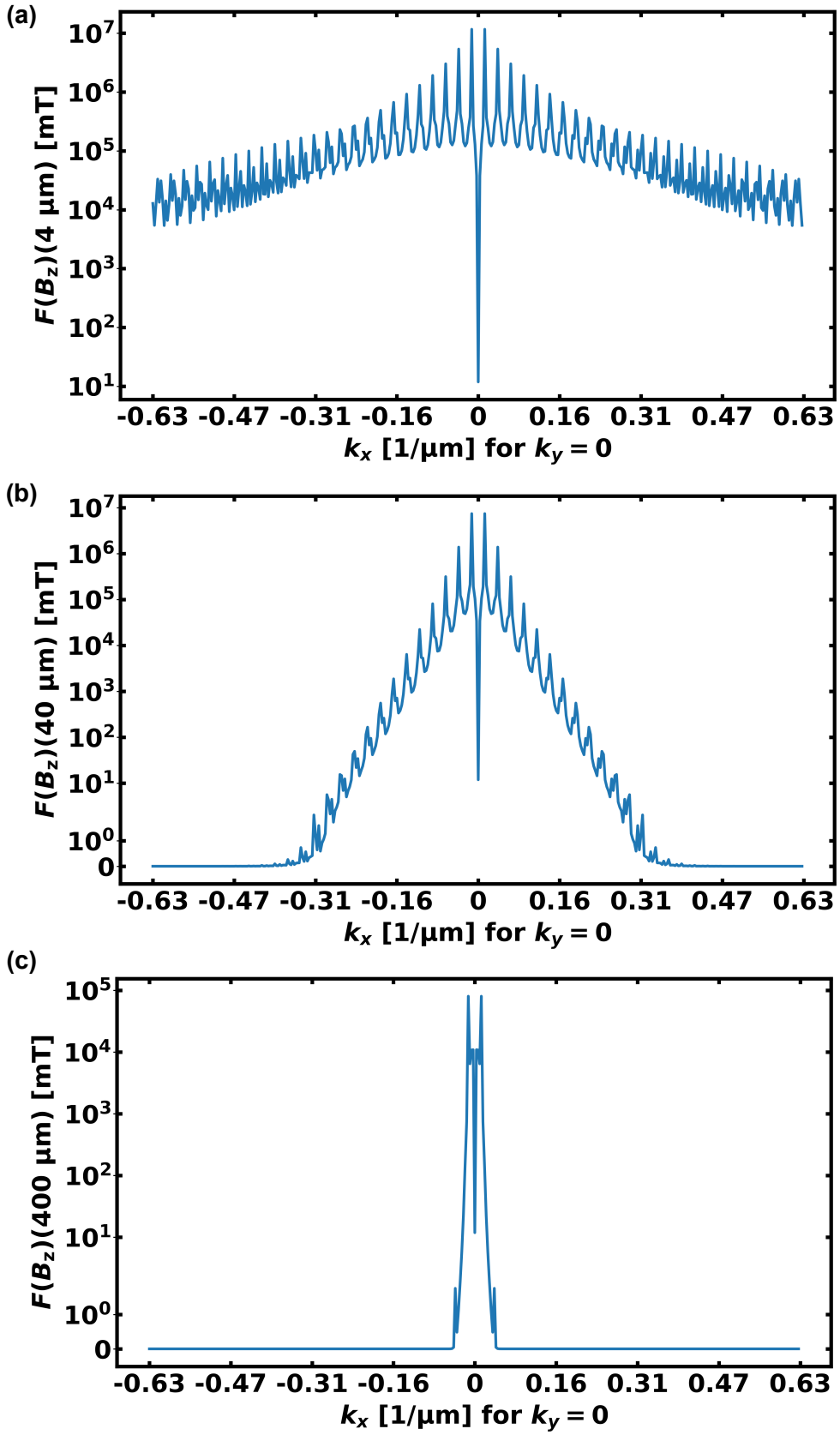

Figure 3.14: k-vector dependent Fourier transform of $B_z((k_x, 0), z)$ at a distance to the sample surface of $z = 4\,\mu\text{m}$, $z = 40\,\mu\text{m}$ and $z = 400\,\mu\text{m}$. SHPM data of the scale SST250HFA04 was used for this calculation.

graphene (on SiC) were fabricated and studied. In contrast to the metallic gold sensors, the graphene samples show an outstanding high sensitivity of 1700 V/(AT), but low time-stability. This suggests that by proper isolation of the graphene sensors from environmental influences (e.g., using hexagonal boron nitride or aluminum dioxide) a higher performance could be achieved. This, in addition to the implementation of graphene Hall sensor on the AFM cantilevers, are the subjects of future studies. For the 5 µm gold AFM-SHPM, the uncertainty budget of the entire room temperature measurement process was analyzed and determined to be $\pm(7\,\mathrm{mT} + 13\,\%)$. This method enables a direct quantitative characterization of magnetic microstructures in ambient conditions with the capability of generating three-dimensional maps of the sample's out of plane stray fields within a range from mT to T. It is expected that by developing a suitable, low-noise electronic for the 50 nm gold Hall sensors the spatial resolution can be further increased which will enable the direct traceable characterization of magnetic nanostructures at room temperature. The fabrication process is scalable thus in principle allowing high volume sensor production. Finally, the AFM-SHPM is a non-destructive and robust method for both scientific research as well as industrial applications, e.g., quality control within industrial processes.

4 Calibration of a magneto-optical measurement system

Another method to characterize magnetic microstructures makes use of the magneto-optical Faraday effect. Here, a new calibration principle for this method is demonstrated at the example of a commercial MOIF device. To traceably map the device's output, in terms of measured contrast in brightness, on magnetic flux density values, a macroscopic calibration of the CMOS-MagView XL in spatially homogeneous, perpendicular magnetic fields is performed. The stray fields are generated by an electromagnet that was pre-characterized with a calibrated Hall probe. The properties of the MOIF device itself were analyzed and used as input for the determination of the uncertainty budget. An additional microscopic calibration which consists of a simulation of the device response considers the influence of vectorial stray fields as well as a field averaging over the sensor thickness. Temperature dependent magnetic properties of the MOIF, as saturation magnetization and magnetic anisotropies, are taken into account for both calibration steps. Finally, the device and calibration performance is demonstrated at an example measurement of a magnetic scale.

Major parts of this chapter are reproduced from Manuela Gerken et al 2020 Meas. Sci. Technol. 31 075009 with permission of IOP Publishing.

4.1 Characterization of the calibration magnet

The calibration of a MOIF device requires a magnetic field with well-known spatial homogeneity and high reproducibility. Here, an electromagnet with a large pole shoe diameter of 250 mm was employed, as shown in Figure 4.1. The magnetic field B_{ext} of the electromagnet is set by a stabilized current generated by a Bruker power supply. The temperatures of the electromagnet and the power supply are stabilized by a water-cooling system (ers Energie- und Kältetechnik GmbH) which is set to 23 °C. The ambient temperature, as measured with a Hall magnetometer (FH55 from Magnet-Physik), was stabilized between 24 °C and 27 °C during the characterization of the magnetic field of the electromagnet and the subsequent calibration of the CMOS-MagView XL. To characterize the magnetic induction as a function of the position between the pole shoes, $B_{\mathrm{ext}}(x, y, z)$, a scanning unit for the Hall magnetometer

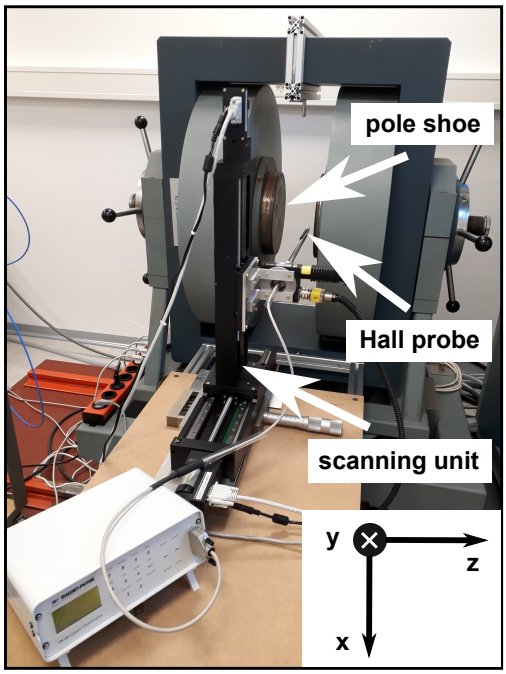

Figure 4.1: Electromagnet utilized for the calibration and scanning unit to characterize its magnetic field.

probe is employed, as indicated in Figure 4.1. The probe can be scanned parallel to the pole shoes (x- and y-direction) using motorized stages (PI) and perpendicular to the pole shoes in z-direction by a manual translation stage. A parallel alignment of the probe with the pole shoes is adjusted and controlled based on the results of an axial scan of the probe that is mounted onto a rotational motor. For the calibration a fixation for the CMOS-MagView XL was built to ensure a reproducible mounting in the electromagnet at a defined position with respect to the pole shoes and the Hall magnetometer. A characterization of the field homogeneity in z-direction showed no significant change on length scales comparable to the thickness of the MOIF with $t = 4.5\,\mu\text{m}$. Therefore, further investigations focused on characterizing the field in terms of stability and repeatability as well as lateral homogeneity for different nominal fields $B_{\text{ext}}^{\text{set}}$. To achieve the traceability to the unit Tesla, the Hall magnetometer was calibrated at PTB. This revealed an offset of 0.1 mT and an additional shift of 0.1 mT over a temperature range of 4 °C resulting in an uncertainty contribution of the Hall probe of $\Delta B^{\text{Hall}} = 0.2\,\text{mT}$.

The stability is estimated by different long-term measurements over several hours. One example where the magnetic flux density was measured over 16 hours for a supply current of 1.9 A is shown in Figure 4.2(a). The field slightly increased over time with the increasing room temperature from 25.6 °C to 27.6 °C, but the overall change was below 0.06 mT. Also measurements at a supply current of 9.1 A, which yields a field of 123 mT, corresponding to

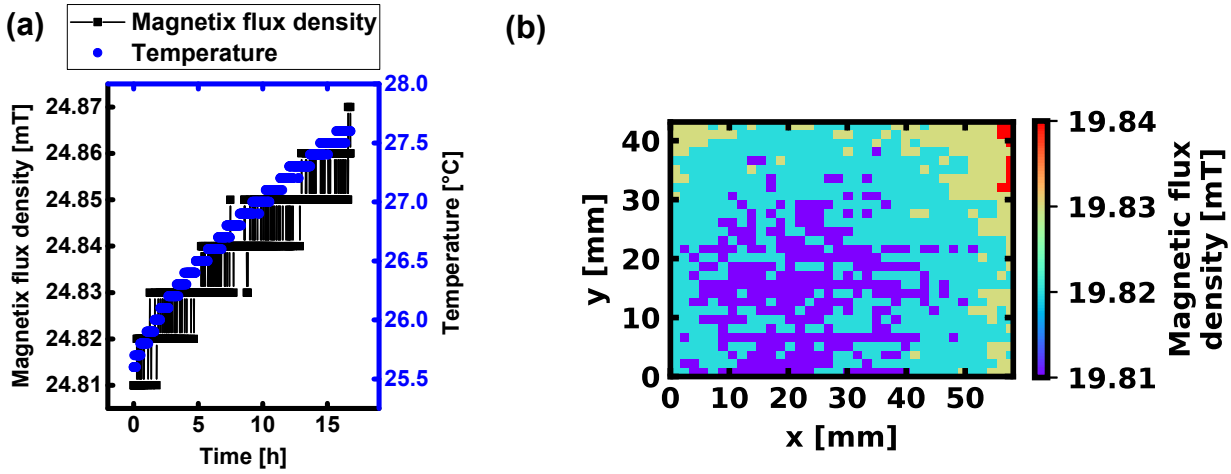

Figure 4.2: (a) Temperature dependence of the magnetic flux density from the electromagnet for a supply current of 1.9 A. (b) Homogeneity of magnetic flux density from the electromagnet over an area of $60 \times 70\,\mathrm{mm}^2$. The supply current was set to 1.6 % of the maximal current, which corresponds to 1.5 A. The overall field deviation is 0.03 mT.

the maximum calibration range, revealed a change in field of 0.1 mT for a temperature drift of 0.6 °C, which is also the resolution limit of the Hall probe in this field range. Another way to estimate the field stability as well as the stability of the scanning unit are repeated measurements of the field along one line. Here, the maximum measured fluctuation for one point over 20 measurements is 0.02 mT. The repeatability of the field measurement process can be estimated by determining the difference in the magnetic field values under repeated zeroing of the Hall magnetometer, reinstalling it in the scanning unit and resetting the supply current. For 20 repetitions differences of 0.1 mT were found. In summary, the uncertainty contributions of the stability and repeatability were estimated as $\Delta B^{\mathrm{stab}} = 0.1\,\mathrm{mT}$ and $\Delta B^{\mathrm{rep}} = 0.1\,\mathrm{mT}$, respectively.

The homogeneity of the magnetic stray field over an area of $60 \times 70\,\mathrm{mm}^2$, which is slightly larger than the sensor film, is shown in Figure 4.2(b). A radial dependency of $B_{\mathrm{ext}}(x, y)$ is visible. However, the deviation over the whole area amounts to only 0.03 mT for $B_{\mathrm{ext}}^{\mathrm{set}} \approx 20\,\mathrm{mT}$ and at a resolution of the Hall magnetometer of 0.01 mT. The field values are smaller in the middle and larger at the edges of the selected window. This is due to the fact that the measurements were performed close to a pole shoe. Here, the field lines are denser at the edge of the pole shoe than in the middle. It is the other way around for measurements centered between both pole shoes. The field homogeneity was measured for 24 field values $B_{\mathrm{ext}}^{\mathrm{set}}$ within the range of $\pm 150\,\mathrm{mT}$. For larger fields around $B_{\mathrm{ext}}^{\mathrm{set}} \approx 90\,\mathrm{mT}$, the overall deviation amounts to $\Delta B^{\mathrm{hom}} = 0.2\,\mathrm{mT}$, partially induced by the decreased resolution of the Hall magnetometer

of 0.1 mT for fields above 30 mT. The field maps are used for a pixel-wise calibration of the MOIF device. By combining the homogeneity and the positioning accuracy of the Hall magnetometer as well as of the CMOS-MagView XL in the electromagnet facilitates to state the uncertainty of the positioning in terms of magnetic flux density $\Delta B^{\mathrm{pos}} = 0.1\,\mathrm{mT}$. This uncertainty is smaller than the overall field homogeneity because in areas sufficiently larger than the positioning accuracy the maximum field change is $\pm 0.1\,\mathrm{mT}$. Adding up all uncertainty contributions resulting from the characterization of the magnetic field of the electromagnet yields an upper value of the overall magnetic field accuracy of

$$\Delta B^{\mathrm{sum}} = \Delta B^{\mathrm{Hall}} + \Delta B^{\mathrm{stab}} + \Delta B^{\mathrm{rep}} + \Delta B^{\mathrm{pos}} = \pm 0.5\,\mathrm{mT}. \tag{4.1}$$

This simple summation approach was chosen because there is no clear function relating all uncertainty contributions and their correlations to the uncertainty of the applied magnetic flux density. The result is confirmed by repeated measurements over a time of several months, where a field uncertainty of about $\pm 0.5\,\mathrm{mT}$ was observed. The above analyzed uncertainty contributions are summarized in the top-left arm of the Ishikawa diagram presented in Figure 4.3. The content of the other arms are explained in the following two sections.

4.2 Properties of the MOIF device

For the calibration a detailed analysis of the MOIF device is required. The properties of the CMOS-MagView XL enter into the uncertainty budget. Furthermore, it is necessary to characterize the magnetic properties of the MOIF, because they enter into the macroscopic calibration algorithm and into the simulation of the device response to micro-scale magnetic stray fields.

4.2.1 Noise, operating temperature, repeatability

To determine the CMOS-MagView XL's noise characteristics, the standard deviation of the intensity was determined from 30 measurements for each pixel. This leads to a mean relative intensity uncertainty over the sensor area of 1.77 % with a standard deviation of the relative uncertainty of 0.24 %. The MOIF temperature is recorded optically. During the calibration, typical temperatures were found to lie between 31 °C and 33 °C. The intensity difference between three measurements performed at 31.1 °C and three performed at 33.25 °C was analyzed for each image pixel, resulting in a temperature induced relative intensity variation

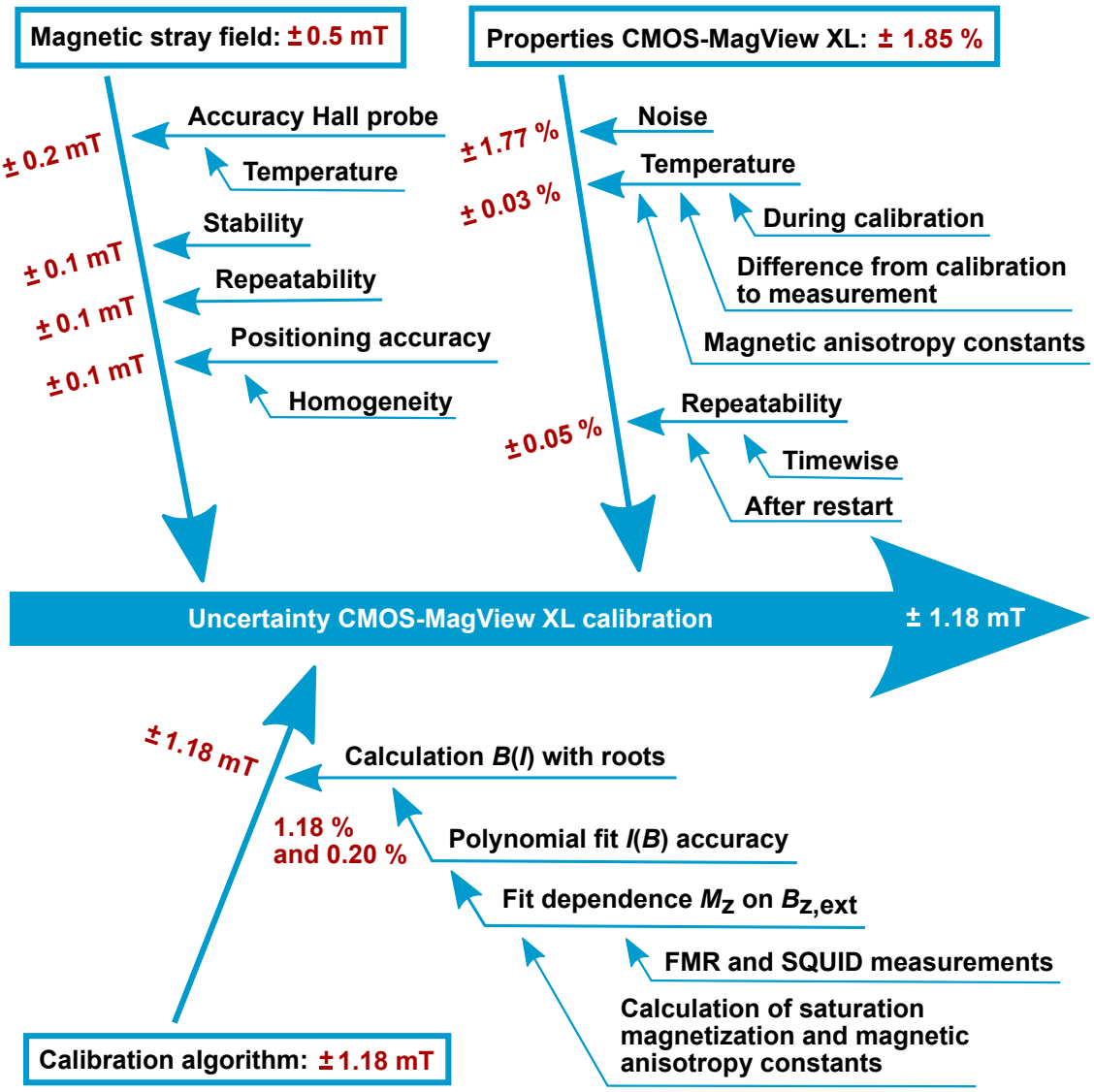

Figure 4.3: Ishikawa diagram summarizing uncertainty contributions of the CMOS-MagView XL calibration for perpendicular homogeneous magnetic stray fields. The uncertainties of the magnetic stray field and the properties of the CMOS-MagView XL are included in the uncertainty of the calibration algorithm by a consideration during the polynomial fit $I(B)$.

over the sensor area of 0.03 % with a standard deviation of 1.3 %, referred to the 31.1 °C data. The temperature of the MOIF during a sample measurement typically is found between 30 °C and 31 °C, comparable to the calibration. Therefore, the relative intensity changes of 0.03 % can be used as an estimation of the temperature induced uncertainty. The repeatability of the intensity measurements was tested by comparing results from before and after a restart of the CMOS-MagView XL. This gives a mean relative uncertainty of 0.05 % with a standard deviation of 1.49 % over the sensor area. The sum of these uncertainty contributions enter into the calibration algorithm presented in section 4.3 and are visualized in the top-right arm of Figure 4.3.

4.2.2 MOIF saturation magnetization

DC-SQUID measurements were performed to analyse the temperature dependent saturation magnetization $\mu_0 M_{\mathrm{S,MOIF}}$ of the MOIF used in the CMOS-MagView XL with a commercial SQUID magnetometer from Quantum Design (MPMS 3) in DC mode by Sibylle Sievers at PTB. The $5 \times 5\,\mathrm{mm}^2$ sample of the same sensor material as used in the MagView XL was glued to a glass rod and field dependent magnetic moment curves $m(H_{\mathrm{ext}})$ were measured with the external field from -1 T to 1 T in the plane of the film. The measurements were performed at different temperatures from 13.85 °C to 46.85 °C in steps of 3 °C. For every temperature, the diamagnetic background was subtracted from the hysteresis curves and the field dependent sample magnetization was calculated regarding the sample volume and a sample geometry dependent correction factor [76]. A magnetization curve at 31.85 °C is shown in Figure 4.4. The saturation magnetization was determined as half the differences of the offset of linear fits to the saturated magnetization values at low and high fields for the up- and down-branches of the hysteresis loop as indicated by the blue and red lines, respectively. The resulting temperature dependent saturation magnetization $\mu_0 M_{\mathrm{S}}(T)$ is shown in Figure 4.5. The analysis revealed, as expected, a nearly linear decrease of the saturation magnetization $\mu_0 M_{\mathrm{S}}$ from 19.0 mT to 17.5 mT with increasing temperature. The saturation magnetization enters into the magnetic anisotropy calculation presented in the next subsection.

4.2.3 MOIF magnetic anisotropies

The magnetic anisotropy constants of the MOIF were characterized by FMR measurements at temperatures varied from 23.23 °C to 47.25 °C in 3 °C steps. The sample was placed upside

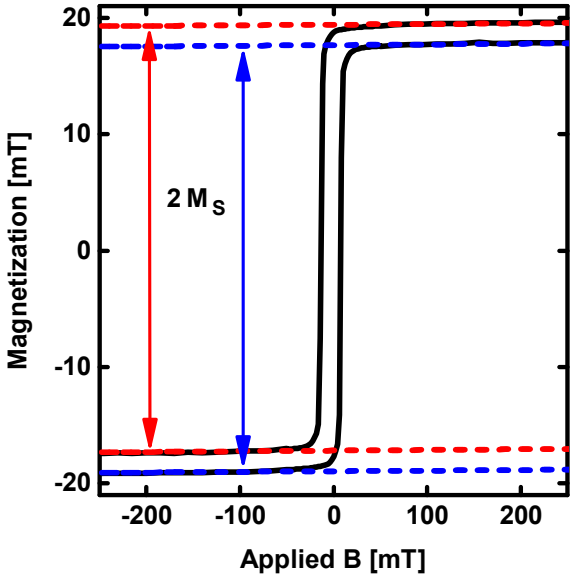

Figure 4.4: MOIF hysteresis at 31.85 °C.

down on a CPW, which was contacted with high frequency probes (GBB Picoprobe Model 40A) and connected to a Vector Network Analyzer (VNA, Rohde & Schwarz ZVA24). A magnetic field with constant amplitude of 100 mT was generated by a yoke that was rotated in the plane around the MOIF to perform ϕ-scans at frequencies up to 10 GHz [77]. The VNA detected transmission parameter S21 is monitored for absorption analysis. A more detailed description of the setup was given in subsection 2.1.5.

The frequency spectra, as visualized for one example in Figure 4.6 where the frequency and in-plane field angle dependent absorption is given, show the appearance of numerous peaks, which were interpreted as spin wave modes. The highest amplitude mode corresponds to a spin wave vector $k = 0$, i.e. a homogeneous, spatially independent excitation [78–80]. The measured resonance frequencies f_{res} of the homogeneous mode as function of temperature and the direction of the applied field in the sample plane ϕ are summarized in Figure 4.7. The dispersion relation of the homogeneous mode can be derived from the Landau-Lifshitz-Gilbert equation given in Equation 2.10 without knowledge of the materials exchange constant A, unlike for the higher k modes. For the analysis of the FMR data, the approach from Smit-Beljers-Suhl as explained in subsection 2.1.5 was applied to the resonance frequency f_{res} as a function of the angle ϕ of the applied field. By fitting equation Equation 2.19 to the measured data, the anisotropies and the orientations of their easy axes can be determined as fit parameters. The saturation magnetization is interpolated from the DC-SQUID data and entered as temperature dependent M into the fit. For the fits, the assumption of aligned

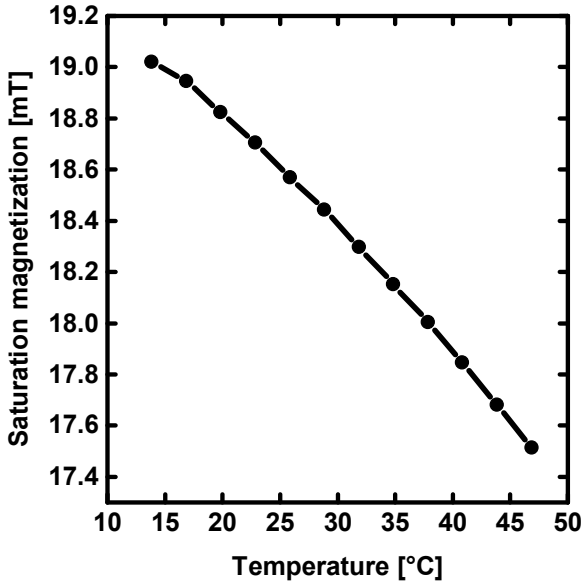

Figure 4.5: Temperature dependent saturation magnetization of the MOIF.

magnetization and magnetic field $\phi = \chi$ is not fully met in the experiment but leads to minor errors, since the applied field was significantly higher than the effective in-plane anisotropy fields. Further, the position of the extrema and the frequency offset are fitted and these values are not significantly impacted by this simplification.

The results of the f_{res} fits for all temperatures are summarized in Figure 4.8(a) in the form of anisotropy fields over temperature, where the anisotropy constants K_{ani} and anisotropy fields are related via $K_{\mathrm{ani}} = B_{\mathrm{ani}} \cdot M_{\mathrm{S}}/2$. The directions of the anisotropy axes are $\phi_{\mathrm{u}} = 0.8\,\mathrm{rad}$ $(= 46°)$ and $\phi_{\mathrm{c}} = 1.46\,\mathrm{rad}$ $(= 84°)$ for all temperatures. The in-plane uniaxial anisotropy data show no clear temperature dependence. This leads to the assumption that these very small anisotropy values below 0.25 mT, for which no physical cause is known in this sample, are artifacts of the measurement setup. Anyhow, considering the fit uncertainty the in-plane uniaxial anisotropy is negligible. The cubic and uniaxial out-of-plane anisotropies reveal a linear dependence on the temperature. They enter into the macroscopic calibration as well as into the simulation of the device response as described in section 4.3 and subsection 4.4.1, respectively. The shape of the free energy density determined by the anisotropy constants as a function of the orientation of the magnetization is visualized in Figure 4.8(b) for a cross-section in the xy-plane and in (c) for all three dimensions. From these images it is clearly visible that the preferred magnetization direction lies in the plane and points in the direction of one of the four minima.

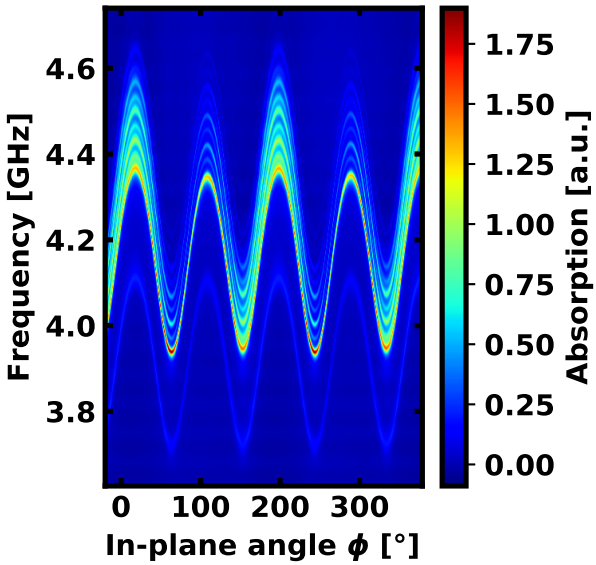

Figure 4.6: FMR frequency spectrum of the MOIF at 100 mT and 30 °C as a function of the angle ϕ of the applied in-plane field.

4.3 Macroscopic calibration

The calibration of the CMOS-MagView XL comprises three steps: (i) First, as presented above, the properties of the device itself were investigated like noise, repeatability and temperature influence as well as the MOIF magnetic properties. (ii) The theoretical functional relation between measured device intensity and underlying perpendicular magnetic field is established allowing different parameters for each image pixel. (iii) The device response in intensity is measured at different, well known magnetic fields in the electromagnet and the results are integrated into the calibration algorithm making use of the theoretical functional relation. The second and third step are explained in this section.

4.3.1 Theory

To establish a calibration algorithm based on physical mechanisms, different contributions to the measured intensity I were considered: The measured MOIF intensity is described by Malus's law [81]

$$I = I_0 \cdot cos^2(\alpha_0 + \beta). \tag{4.2}$$

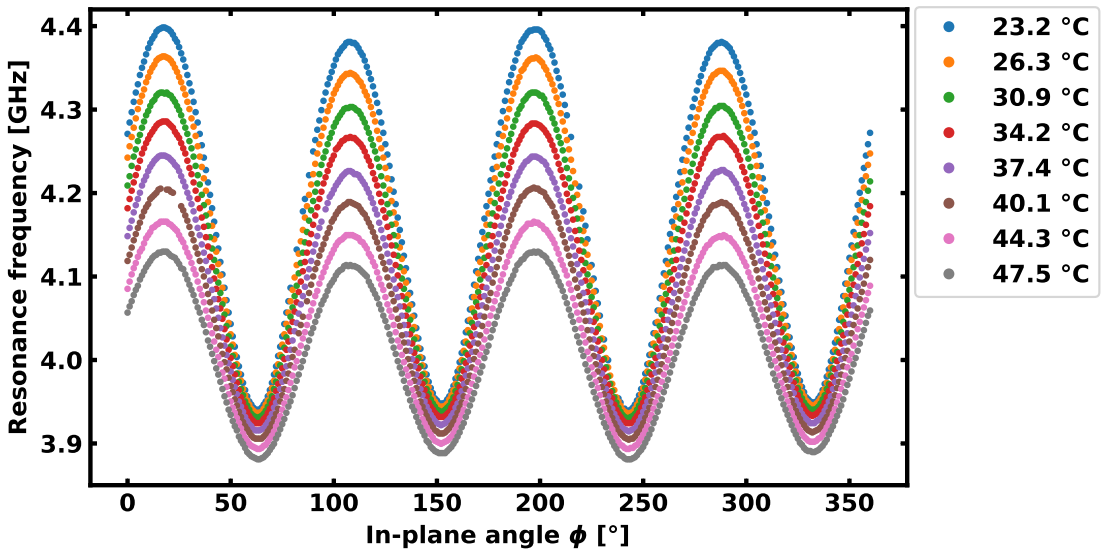

Figure 4.7: Resonance frequency f_{res} of the homogeneous mode of MOIF at 100 mT as a function of the angle ϕ of the applied in-plane field for different temperatures.

The intensity of the light before the second polarizing filter and after transmission through the MOIF is I_0. The angle $\alpha_0 = 45° + n \cdot 90°$ with $n = \pm 0, 1, 2, ...$ is the angle between the two polarizing filters which are placed in the optical path before and after the MOIF. The value of α_0 is selected to achieve the largest magnetic field sensitivity, which is in the linear regime of the cos^2 function. Whether even or odd values of n apply depends on the fact if the intensity is increasing or decreasing for an increase of the applied magnetic field. As explained in subsection 2.1.2, the Faraday rotation $\beta = c \cdot M_{\mathrm{z}}$ is proportional to the out-of-plane component of the MOIF magnetization M_{z} [36], with $M_{\mathrm{z}} = M_{\mathrm{S}} \cdot \cos\theta$, where M_{S} is the saturation magnetization of the MOIF and θ the angle between the actual direction of the magnetization and the vector normal to the film plane. The intensity thus can be described as

$$I = I_0 \cdot cos^2(\alpha_0 + c \cdot M_{\mathrm{S}} \cdot \cos\theta(B)). \tag{4.3}$$

Since $\alpha_0 + \beta \in [125°, 145°]$, because a maximum doubled Faraday rotation of 10° is observed for this particular MOIF material, the outer $\cos^2$ function can be linearly approximated leading to

$$I = k_1 + k_2 \cdot \cos\theta(B) \tag{4.4}$$

with $k_1 = I_0 \cdot \cos^2\alpha_0$ and $k_2 = -2 \cdot I_0 \cdot c \cdot M_{\mathrm{S}} \cdot \cos\alpha_0 \cdot \sin\alpha_0$. The functional dependence of $\cos\theta$ on an external field in z-direction was simulated by a minimization of the free energy.

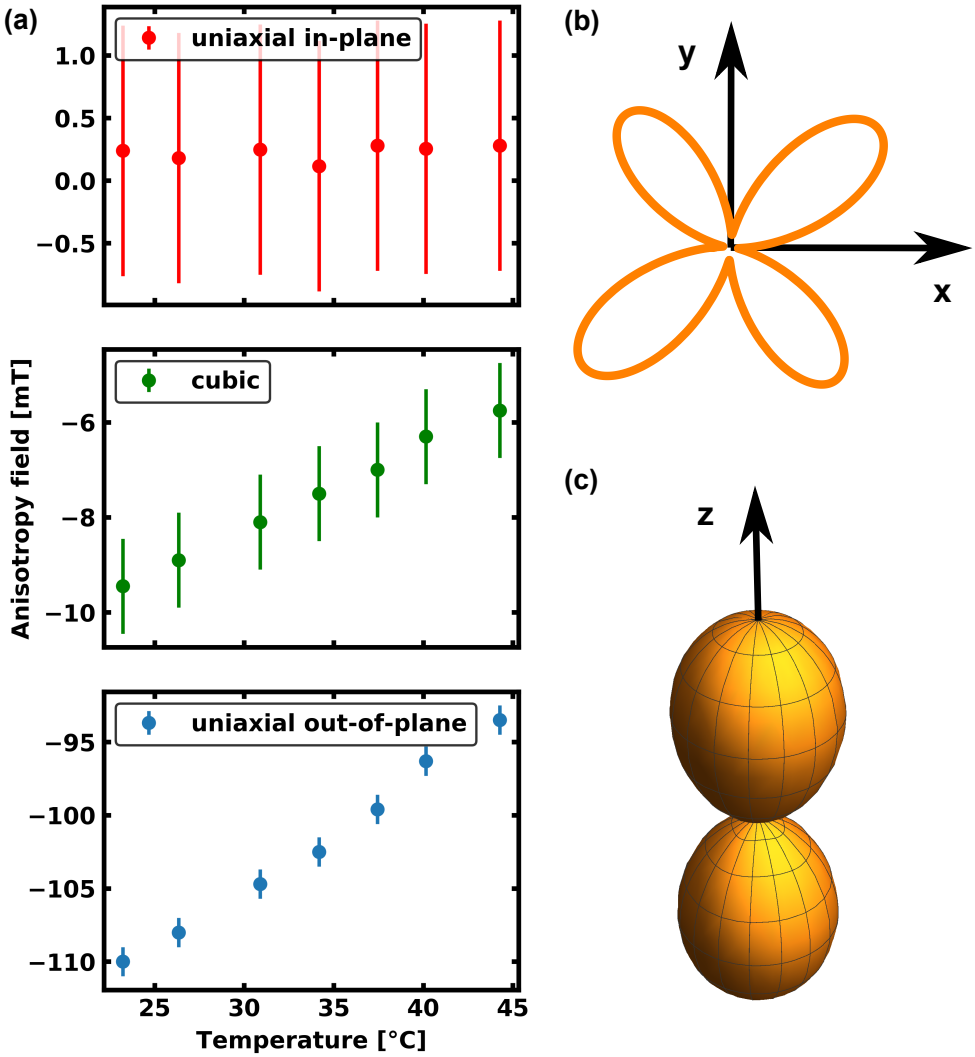

Figure 4.8: (a) Temperature dependence of the MOIF anisotropy fields. (b) Shape of the free energy density in the xy-plane. (c) Free energy density of the MOIF in three dimensions at 30.9 °C. Here, the cubic shape of the energy density as shown in (b) is not visible due to the larger effect of the out-of-plane anisotropy.

For that purpose, the magnetic anisotropy constants, which were determined with the help of FMR, were used. The simulation result could be fitted well with the cubic equation

$$\cos\theta(B) = a \cdot B^3 + b \cdot B \tag{4.5}$$

as shown in Figure 4.9. This finally leads to the following equation for the intensity response

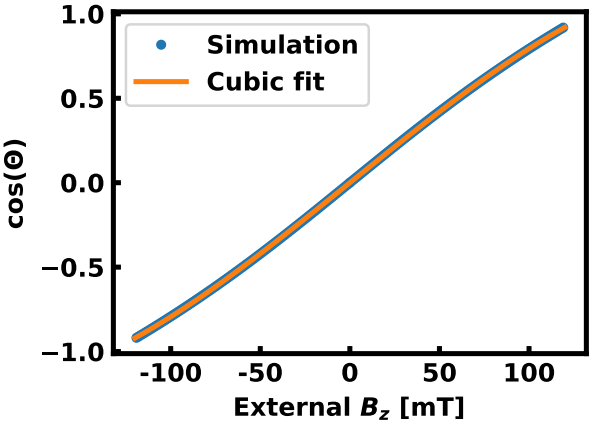

Figure 4.9: Relation between $\cos\theta$ which is proportional to the out-of-plane component of the MOIF magnetization M_z and an external, homogeneous and perpendicular magnetic flux density. The simulation considers magnetic anisotropies of the MOIF, thus this relation is not linear.

of the CMOS-MagView XL to an applied homogeneous, perpendicular magnetic field.

$$I = k_1 + k_2 \cdot \left(a \cdot B^3 + b \cdot B\right) \tag{4.6}$$

$$= k_1 + k_2 \cdot \left(-61.934 \cdot B^3 + 8.560 \cdot B\right) \tag{4.7}$$

4.3.2 Results

Assuming homogeneous MOIF material parameters over the sensor area would lead to merely lightning intensity dependent constants $k_1 = I_0 \cdot p_1$ and $k_2 = I_0 \cdot p_2$, with universal p_1 and p_2. However, fitting the measured data $I(B)$ with only I_0 as a free parameter for each pixel did not lead to satisfying results. Therefore, it is concluded that at least one further parameter is not constant over the MOIF area. So, both k_1 and k_2 were used as free fit parameters for $I(B)$.

The fit of the intensity dependence on the magnetix flux density was realized in Python using the scipy.odr package from NIST [82], considering the obtained uncertainties for the

applied magnetic field and for the intensities of the CMOS-MagView XL. The result, using Equation 4.7, is shown in Figure 4.10 for one of the pixels where the cubic relation is clearly visible. The fit solutions for k_1 and k_2 for every pixel are visualized in Figure 4.11(a) and (b).

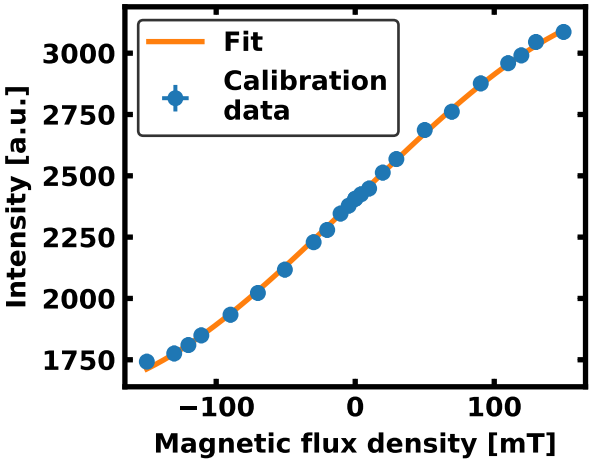

Figure 4.10: Polynomial fit of the calibration data $I(B)$ for pixel 700×1000 in the middle of the sensor film.

Figure 4.11(c) and (d) contain the doubled relative standard uncertainties of the parameters for each pixel. The mean doubled relative standard uncertainty for k_1 is 0.20 % and its standard deviation over the film area is 0.06 %. The corresponding mean uncertainty for k_2 is 1.18 % and its standard deviation is 0.48 %. To inversely calculate the stray field of a magnetic sample from the measured intensity data another Python script was programmed. This extracts the stray field values B by finding the roots of the rearranged Equation 4.7

$$0 = B^3 - 0.138 \cdot B - \frac{k_1 - I}{61.934 \cdot k_2}. \tag{4.8}$$

4.3.3 Uncertainty

Standard error propagation procedures cannot be applied to this inverse numerical process. Therefore, to relate the above discussed factors to the measurement uncertainty, artificial intensity data were created, using Equation 4.7, corresponding to a homogeneous external field of 5 mT and 108 mT, respectively. From these data the stray field values were calculated with k_1 and k_2 as well as with $k_1 - 0.2\,\%$ and $k_2 - 1.18\,\%$ which results in the largest possible error. The mean difference of these two calculations for 5 mT is 0.88 mT, which corresponds to a relative uncertainty of 17.6 %. For 108 mT the mean difference is 1.18 mT leading to a relative uncertainty of 1.09 %. The calibration algorithm allows only values within the

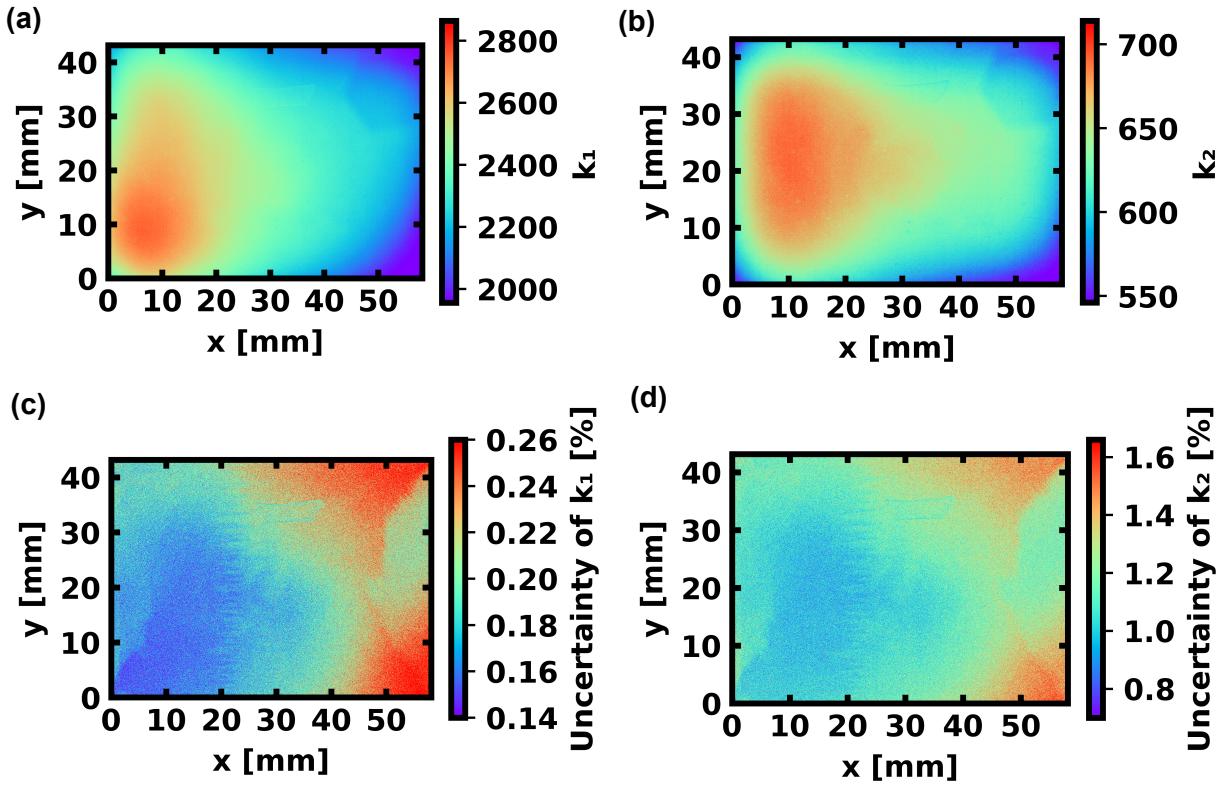

Figure 4.11: (a) and (b) Values for the fitted k parameters from the calibration data for each pixel. (c) and (d) Corresponding uncertainty data.

calibrated field range of $\pm 110\,\mathrm{mT}$, thus the maximal field uncertainty for the calibrated device is $1.18\,\mathrm{mT}$.

4.3.4 Discussion and summary

As mentioned in subsection 4.3.2, the results of the calibration fit indicate that some optical or magnetic parameters are not constant over the MOIF area. Either α_0 might vary locally due to the optical path or the film properties might change. An inhomogeneous material distribution or defects might, for example, lead to differences in the material dependent constant c. Similarly, a non-constant thickness or differences in the saturation magnetization of the MOIF would influence the result, alike local temperature or strain variations. The influence of strain from gluing the MOIF into the device is for example visible in Figure 4.11(c) and (d). The images show the uncertainties of the fit parameters for the macroscopic calibration of the MOIF device. However, the color gradients also reveal the existence of strain in the MOIF. The zig-zag structure at $x = 20\,\mu\mathrm{m}$ indicates the pathway of a domain wall in the MOIF.

Domain walls and strain influence the local orientation of the MOIF magnetization and thus also influence the calibration and measurement results.

In conclusion, the intensities measured by the MOIF device, CMOS-MagView XL, were related to applied homogeneous and well known magnetic flux densities. The calibration algorithm is based on physical properties and its parameters were determined for every pixel. All results of the uncertainty estimation for the macroscopic CMOS-MagView XL calibration in homogeneous stray fields are summarized in Figure 4.3. The uncertainty is determined to $\pm 1.18\,\mathrm{mT}$.

4.4 Microscopic calibration

For the characterization of magnetic microstructures the macroscopic calibration is not sufficient. The spatially fast changing stray field components and the sensor thickness might influence the measurement results significantly. Therefore, these topics are discussed below and demonstrated on an example in subsection 4.5.1.

4.4.1 Simulation of device response for vector stray fields

Instead of simulating the sample stray field based on the device response a forward simulation starting from a guessed sample magnetization was chosen. This takes account of the fact that the inversion process for stray fields below the switching field of the MOIF material and from the perpendicular magnetization component of the MOIF to stray field vector of the sample generally is ambiguous. The underlying magnetization pattern of the sample is estimated by a discrimination, as explained in subsection 2.1.6, assuming a perpendicular magnetization. The implemented procedure allows an arbitrary distribution of up and down magnetized regions, similar to the approach presented in section 3.6. To define a discrimination criterion, the fact was exploited that, while the device output in general must be corrected for the impact of sensor thickness and in-plane components, the field value $B = 0\,\mathrm{mT}$ is displayed correctly provided that the macroscopic calibration was performed and a reference image is subtracted from the data. Additionally, the sign of the field values is maintained. Therefore, areas with a measured field value B_{meas} above or below zero are interpreted as up and down magnetized regions, respectively. This initially results in sharp transitions between the domains. To allow for a finite domain wall width, the image can be convolved with a domain transition kernel with selectable transition width. From the estimated magnetization pattern the magnetic

stray field of the sample $\boldsymbol{B}_{\mathrm{Sample}}$ at the distance of the MOIF can be calculated based on the transfer function approach explained in subsection 2.1.7.

In the following, the approach to calculate the CMOS-MagView XL device response is described. The first objective is to determine the orientation of the sensor magnetization $\boldsymbol{M}_{\mathrm{MOIF}}$ for a given magnetic field orientation $\boldsymbol{B}_{\mathrm{Sample}}$. For this calculation, minima of the free energy function F are determined. The contributions of F are given in Equation 2.14 to Equation 2.18. At minimum free energy the angles ϕ and θ_{M} define the MOIF magnetization $\boldsymbol{M}_{\mathrm{MOIF}}$. The applied free energy function is identical to the one used for the FMR simulations considering the determined magnetic anisotropies but disregarding the negligibly small uniaxial in-plane anisotropy. When multiple minima are found, the solution closest to the solutions found for neighboring sample positions is selected to enforce continuity. Thus, $\boldsymbol{M}_{\mathrm{MOIF}}(\boldsymbol{B}_{\mathrm{Sample}})$ is known.

The second objective is to obtain the relation between $\boldsymbol{M}_{\mathrm{MOIF}}$ and the field measured by the CMOS-MagView XL B_{MagView}. This relation is not linear due to the influence of anisotropies as represented by Equation 4.5. Furthermore, the CMOS-MagView XL signal I is a monotonous and continuous function of merely the perpendicular magnetization component $M_{\mathrm{z,MOIF}}$ of the sensor film. The in-plane components of $\boldsymbol{M}_{\mathrm{(x,y),MOIF}}$ are not relevant for the response. It is assumed that the CMOS-MagView XL is perfectly calibrated by a function $I(B_{\mathrm{ext}})$ in perpendicular magnetic fields B_{ext} as discussed above. Therefore, the function $f(B_{\mathrm{ext}}) = M_{\mathrm{z,MOIF}}$ is calculated again by the minimization of the free energy function. This leads to the relation between $\boldsymbol{M}_{\mathrm{MOIF}}(\boldsymbol{B}_{\mathrm{Sample}})$ and the field value given by the CMOS-MagView XL $B_{\mathrm{MagView}} = B_{\mathrm{ext}}$ by $B_{\mathrm{MagView}} = f^{-1}(M_{\mathrm{z,MOIF}}(\boldsymbol{B}_{\mathrm{Sample}}))$. Thus, the calculated device response B_{MagView} can be directly compared to the output of the macroscopically calibrated CMOS-MagView XL.

4.4.2 Influence of MOIF thickness

The finite sensor thickness leads to an averaging of the magnetic sample stray field over the sensor. Therefore, when measuring small structures with spatial rapidly decaying stray fields, the CMOS-MagView XL measures a reduced signal compared to the field present at the sample-side face of the sensor. For perpendicular field components, the impact of the finite MOIF sensor thickness t can be estimated by a transfer function *MOIF TF* which regards the k-vector dependent decay of the stray field. It returns a first order correction of the measured stray field value, resulting into the stray field at the sample-sided sensor surface.

The MOIF induces a Faraday rotation $\beta = c_1 \cdot M_z$ of the incident light. For moderate fields, a linear relation between the z-component of the field H_z and sensor magnetization M_z can be postulated, $M_z = c_2 \cdot H_z$, in good approximation of the observed relation. Here, in-plane fields are neglected. This results in a linear relation between Faraday rotation and field, $\beta = c_1 \cdot c_2 \cdot H_z$. For a decaying H_z, the sensor volume between upper, sample sided surface at $z = z_0$ and lower surface at $z = z_0 + t$ is conceptually divided into infinitesimally thin layers parallel to the surface that contribute an amount of $\mathrm{d}\beta(x,y) = \frac{c_1 \cdot c_2}{t} \cdot H_z(x,y,z) \cdot \mathrm{d}z = \frac{c'}{t} \cdot H_z(x,y,z) \cdot \mathrm{d}z$ to the Faraday rotation. The net Faraday rotation at any position (x,y) then can be calculated as an integral over the sensor thickness

$$\beta(x,y) = \int_0^t \frac{c'}{t} \cdot H_z(x,y,z)\,\mathrm{d}z \tag{4.9}$$

The same relation also holds in the 2D-Fourier space, since the Fourier transform commutes with the z-integral. From Equation 2.24 one can derive that in 2D-Fourier space, the field component at a distance z_2, $H_z(z_2)$, can be calculated from the field at distance z_1, $H_z(z_1)$, via an exponential decay factor, $H_z(z_2) = H_z(z_1)e^{-k(z_2-z_1)}$. Inserting the latter relation into the Fourier transformed Equation 4.9 using gives:

$$\begin{aligned}\beta(\boldsymbol{k}) &= \int_0^t \frac{c'}{t} \cdot H_z(\boldsymbol{k}, z_0) \cdot e^{-kz'}\,\mathrm{d}z' \\ &= \frac{c'}{t} \cdot H_z(\boldsymbol{k}, z_0) \cdot \int_0^t e^{-kz'}\,\mathrm{d}z' \\ &= \frac{c'}{t} \cdot H_z(\boldsymbol{k}, z_0) \cdot \frac{1}{k}\left(1 - e^{-kt}\right)\end{aligned} \tag{4.10}$$

A calibrated CMOS-MagView XL device would interpret this $\beta(\boldsymbol{k})$ as a homogeneous field with constant amplitude $H_z^{\mathrm{const}} = \frac{1}{c'} \cdot \beta(\boldsymbol{k}) = \frac{1-e^{-kt}}{t \cdot k} \cdot H_z(\boldsymbol{k}, z_0)$. Therefore, to calculate the sensor response, the $H_z(\boldsymbol{k}, z_0)$ data at the upper surface of the sensor have to be multiplied with a k-vector dependent transfer function $MOIF\ TF$

$$MOIF\ TF = \frac{1 - e^{-kt}}{t \cdot k}. \tag{4.11}$$

Vice versa, the $H_z(\boldsymbol{k}, z_0)$ data can be recovered from the CMOS-MagView XL data using the inverse transfer function $MOIF\ TF^{-1} = \frac{kt}{1-e^{-kt}}$.

The derived $MOIF\ TF$ only holds strictly within the area of validity of the above stated limitations. This particularly applies to the assumed linear relation between M_z and H_z. However, even for fields where these conditions are not fully met, the $MOIF\ TF$ allows to estimate the level of relevance of the field decay for the measured field data. The relevance

depends on the relation between pixel resolution and sensor thickness t. Furthermore, it depends on the sample structure size (via k) and the sensor-sample distance z, since components with large k are mostly decayed at high distances. The impact of the MOIF sensor thickness is low for the CMOS-MagView XL with comparably large pixel size of $28 \times 28\mu m^2$ as shown in the next section. However, the correction can become significant for high resolution measurements, e.g. using MOIF based microscopes.

4.5 Application

In this section a magnetic scale is characterized with the CMOS-MagView XL. In this process, the significance of the microscopic calibration is emphasized.

4.5.1 Measurement and simulation of a magnetic scale

The performance of the CMOS-MagView XL calibration is demonstrated by the characterization of the same scale as utilized in section 3.4, SST250HFA04 from Sensitec GmbH. The scale is shown in Figure 4.12(a). The Sr-ferrite based scale has a written pole pattern of alternating up and down poles with a nominal pole size of 250 µm and a remanence magnetization of $\mu_0 M_R = 395\,\mathrm{mT}$. The measurement result is shown in Figure 4.12(b) and a magnification of the selected area for further investigation in (c). In part (d) the created discrimination image is shown. Step-like features at the pole transitions are an artefact of the limited pixel resolution. From this selected area a cross-section at $y = 1\,\mathrm{mm}$ was further examined. The results are presented in Figure 4.13. In part (a) the magnetic field data measured by the MOIF device after the macroscopic calibration is depicted together with the discrimination pattern which includes a pole transition width of 50 µm. In part (b) all three stray field components are presented as calculated from the discrimination image. Differences between the simulated z-component and the measured field as given by the CMOS-MagView XL are clearly visible. Part (c) shows the corrected stray field taking into account the finite sensor thickness, as resulting from Equation 4.11. By the perfect overlap of the two curves it can be seen that the influence of the sensor thickness is negligible in this case due to the relatively large distance between sample and sensor in comparison to the sensor thickness. Since the components for high k are already decayed. All three stray field components were used to simulate the device response as explained in subsection 4.4.1. The comparison with the measured signal is shown in part (d). For an assumed measurement height of $50\,\mu\mathrm{m} \pm 10\,\mu\mathrm{m}$ (due to the sample roughness) and an assumed thickness of $d = 75\,\mu\mathrm{m}$ for the magnetic

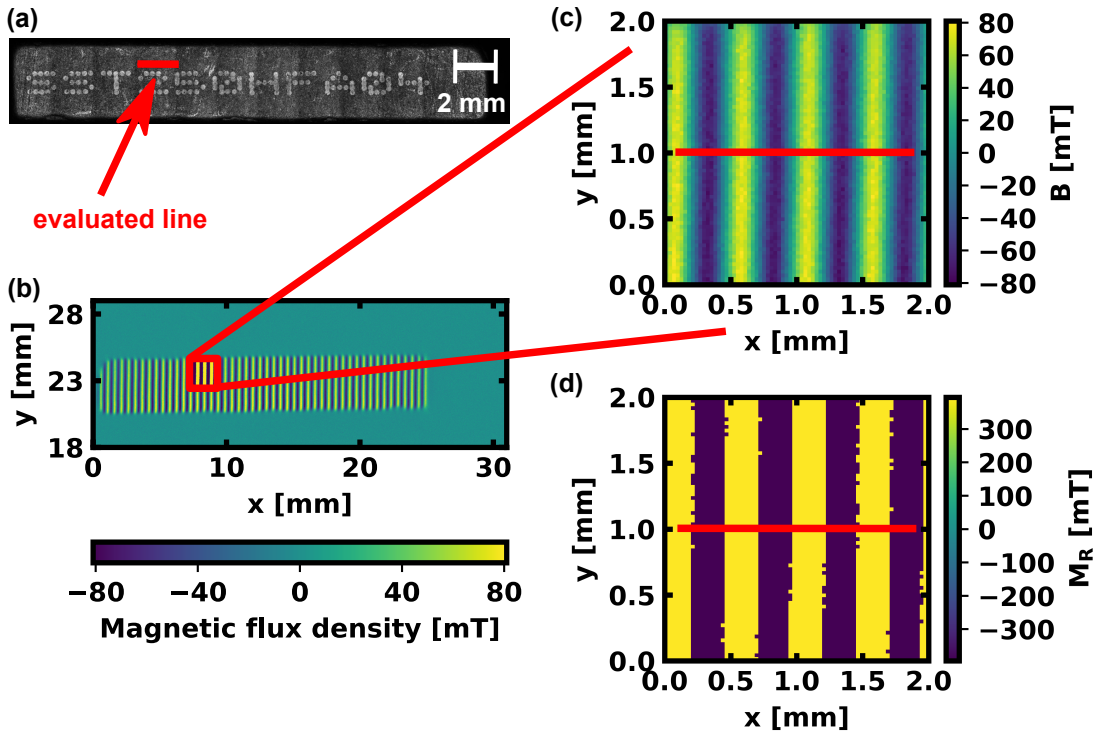

Figure 4.12: (a) Image of the investigated magnetic scale. (b) Stray field of the scale measured with CMOS-MagView XL. (c) Selected area for further investigation. (d) Assumed sample magnetization generated by discrimination.

material a good agreement between measurement and simulation is found. An initial value for the measurement height was chosen based on the measured sample roughness analyzed in Figure 3.9 and the possibility of dust particles between the sample and the sensor. Then the measurement height as well as other simulation parameters like the sample thickness were adjusted in an iterative process until a good agreement of measured and simulated data was achieved. Therefore, the significant discrepancy between measured CMOS-MagView XL data and simulated perpendicular component of the sample stray field can be well explained by the influence of in-plane magnetic field components. The small remaining differences can probably be attributed to imperfection of the writing process during the fabrication of the scale and to the rough surface of the sample with grains of about 10 µm.

4.5.2 Uncertainty Budget

The analysis of the measurement result is completed by the determination of the uncertainty budget. Since, there is no clear functional relation between B and the parameters needed to calculate B, again, the standard uncertainty propagation is not applicable. B is calculated

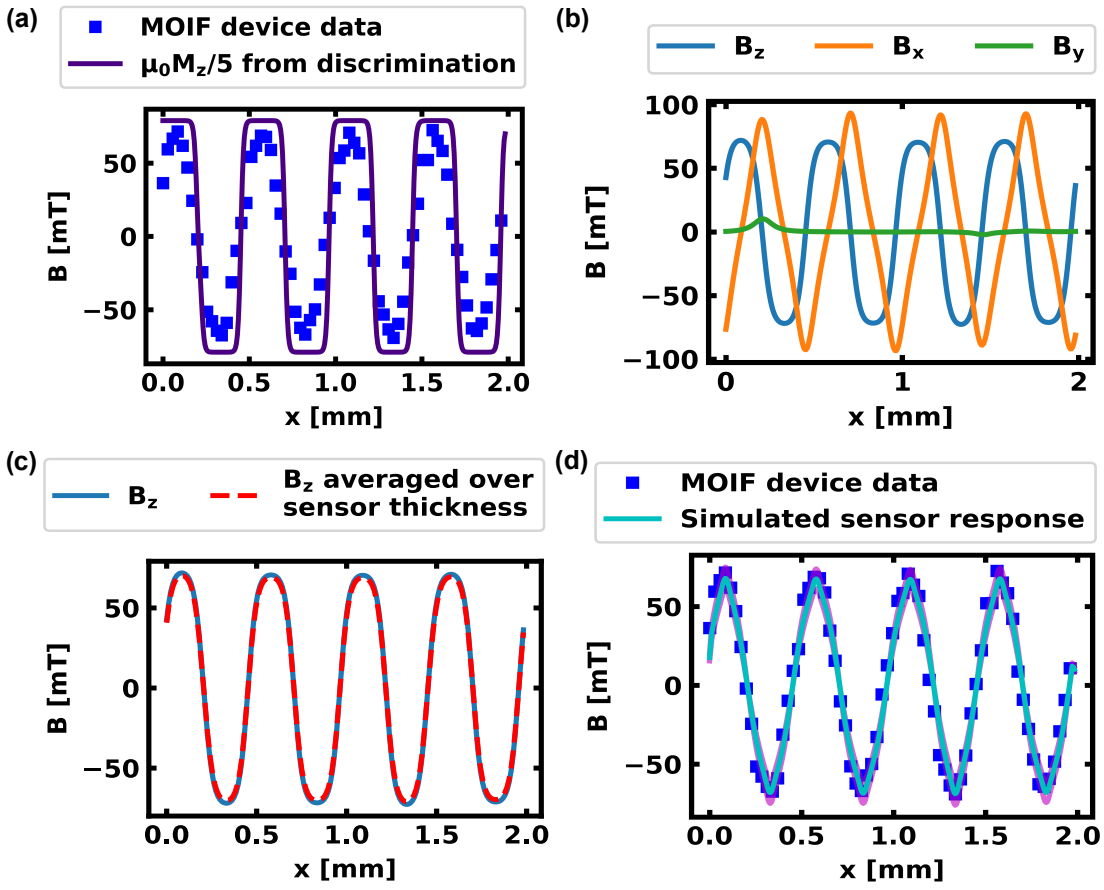

Figure 4.13: Comparison of simulation and measurement for the magnetic scale SST250HFA04. (a) Measured magnetic field of one line together with the discrimination pattern which takes the transition width into account. (b) Simulation results of all three stray field components. (c) Impact of sensor thickness on the result. (d) Comparison of measured data and simulated sensor response for a remanence magnetization of 395 mT, a transition width of 50 µm, a measurement height of 50 µm and a 75 µm thick magnetic layer. The magenta region displays the simulation uncertainty regarding measurement height uncertainty of ±10 µm.

by finding the roots of Equation 4.8. The first contribution to the uncertainty of B from this equation is the uncertainty of the macroscopic calibration with $\pm 1.18\,\mathrm{mT}$, which originates from the uncertainty of the parameters k_1 and k_2. The second contribution is the uncertainty of the measured intensity I. This uncertainty of the actual scale measurement is $\pm 1.3\,\mathrm{mT}$. It was derived from the doubled standard deviation of the mean of 10 repeated measurements averaged over all pixels. Thus, the uncertainty of the magnetic flux density is ascertained to $\pm 2.5\,\mathrm{mT} \approx \pm(1.18\,\mathrm{mT} + 1.3\,\mathrm{mT})$. The uncertainty of the measurement height was, due to the sample roughness, estimated to $\pm 10\,\mu\mathrm{m}$. The lateral resolution of $28\,\mu\mathrm{m}$ is given by the pixel number of the CMOS camera and the size of the sensor film.

4.6 Conclusion MOIF calibration

A calibration approach for MOIF devices was presented and successfully implemented for a commercial device, the CMOS-MagView XL from Matesy GmbH. The approach enables traceable measurements of magnetic microstructures. First, a macroscopic calibration using well-known, homogeneous and perpendicular stray fields is performed to relate the measured intensity to the magnetic flux density. The assessment of the uncertainty budget is discussed, revealing a calibration uncertainty of $1.18\,\mathrm{mT}$ over the measurement range of $\pm 110\,\mathrm{mT}$ for the CMOS-MagView XL. Second, a microscopic correction approach was implemented which is indispensable for the quantitative investigation of magnetic microstructures and which was realized here for the first time. It comprises the simulation of the device response considering (i) properties of the MOIF like saturation magnetization and anisotropy constants, (ii) the averaging over the sensor film thickness and (iii) the influence of in-plane stray field components. Thereby, the sensor response on all three stray field components can be determined. By a comparison with the measured signal, it is possible to estimate the sample remanence magnetization, magnetic layer thickness, transition width between opposite magnetized areas and measurement height. Further all three stray field components of the sample can be reconstructed. This is successfully demonstrated for the CMOS-MagView XL by means of the characterization of a magnetic scale. In conclusion, a unique tool for fast and quantitative characterization of scientific and industrial relevant magnetic microstructures was created.

5 Comparison of measurement techniques

A convenient way to validate the presented measurement techniques SHPM and MOIF as well as the performed calibrations is to execute a cross comparison. Therefore, in this chapter the results from the measurements of the stray field of the above introduced scale SST250HFA04 with a 5 µm gold Hall sensor on a cantilever tip by SHPM and with the CMOS-MagView XL using the Faraday effect in a MOIF as introduced in section 3.4 and subsection 4.5.1, respectively are compared. To understand the differences in the results of the two measurement methods and to validate the measured data, first the expected outcomes are analyzed in detail by investigating simulation results. The expected SHPM data represented by the perpendicular stray field component B_z was simulated with the TF approach based on the SHPM data as presented in 3.6. The simulation of the CMOS-MagView XL response was introduced in 4.4.1. It also includes the TF approach as well as a determination of the z-component of the MOIF magnetization considering in-plane stray field components, the MOIF's magnetic anisotropies and the macroscopic device calibration.

In Figure 5.1 the SHPM data and MOIF device data from characterizing the magnetic scale SST250HFA04 as well as the corresponding simulation results are presented. Differences of the two methods are emphasized by the simulations. The shape of the expected SHPM data in terms of simulated B_z is sinusoidal, or rectangular for small transition widths and low measurement heights, in comparison to the triangular shape of the simulated MOIF device response. This is due to the fact that SHPM mainly detects the out-of-plane component, whereas the MOIF device is also sensitive to in-plane components of the magnetic stray field. The stray field vector of the sample determines the z-component of the MOIF magnetization M_z that is detected by the MOIF device via Faraday rotation. Even for B_z = constant, a change in B_x or B_y will change M_z. Furthermore, not only this in-plane stray field components but also the magnetic anisotropies of the MOIF influence M_z. Thus, also the MOIF device response incorporates all these factors. Hall sensors are sensitive to the stray field component which is perpendicular to their plane. Due to the small cantilever tilt angle of 10°, SHPM detects also a small fraction of the in-plane components. However, B_z is decisive here.

The simulations show deviations in the maximum and minimum B values between SHPM and MOIF. Therefore, the influence of input parameters on the simulation outcome is analyzed in

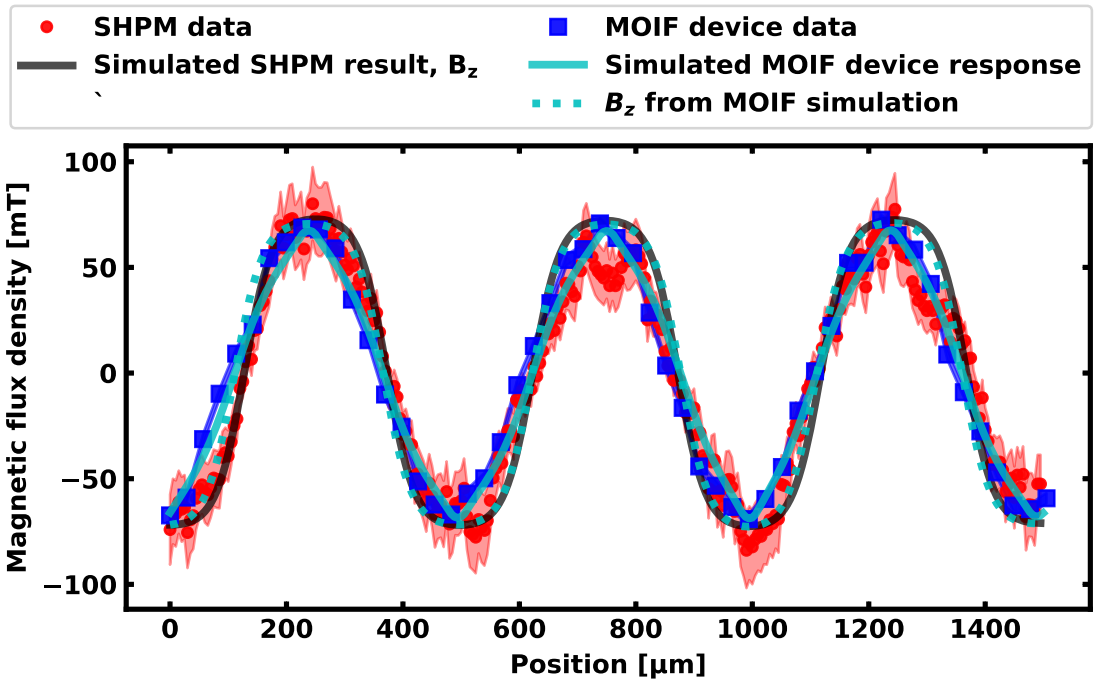

Figure 5.1: Comparing measurement results of the same magnetic scale using the two techniques MOIF with CMOS-MagView XL and traceable SHPM with a 5 µm gold Hall sensor at a measurement height of 49 µm. The uncertainty of the MOIF data is ±2.5 mT, which is smaller than the data point size. Also, simulations of the expected B values are shown. [Adopted from Manuela Gerken et al 2020 Meas. Sci. Technol. 31 075009 with permission of IOP Publishing.]

detail. Some simulation parameters as the pole transition width w, the measurement heights z_{SHPM} for SHPM and z_{MOIF} for MOIF technique as well as the magnetic layer thickness d are either not known or exhibit a non-neglectable uncertainty. They are listed in Table 5.1 and the values used and determined in the previous chapters are given in column '0'. Their uncertainties are utilized to define upper and lower boundaries as given in column '+' and '–', respectively. The transition width was assumed to 50 µm due to the pole writing process with current pulses. The lower and upper boundaries cover the possible range from perfect sharp transitions to a transition width reaching over the entire pole width. The measurement height of SHPM was set to 49 µm. The upper and lower boundaries represent the positioning uncertainty of the z-piezo in combination with the rough sample surface. The measurement height of the MOIF and the magnetic layer thickness were determined through a sample surface analysis and iterative simulations to 50 µm and 75 µm, respectively. The uncertainty of these values was estimated by simulation experience to ±10 µm and consequently the upper and lower boundaries were set. Nine simulation experiments are defined in Table 5.2 covering all possible combinations of upper and lower boundaries, similar to a design of

experiment plan [83]. This strategy has the benefit to reveal correlations between the simulation parameters. Furthermore, conventional uncertainty analysis is not applicable because no unambiguous function between the parameters and the result can be established due to the fact that the simulation of the MOIF device response is based on a minimization of the free energy and a continuous behavior of the MOIF magnetization. The results for these simulation experiments in terms of maximum and minimum B values over the poles are presented in Table 5.3 and the corresponding graphs, showing the shapes, are depicted in Figure 5.2 to Figure 5.9.

Table 5.1: Input parameters of the simulations and their boundaries defining the uncertainty range. The values in column '0' were determined by iterative simulations or are expectation values as described in the previous chapters.

Parameter	**−**	**0**	**+**
Pole transition width	0 µm	50 µm	125 µm
Measurement height			
SHPM	34 µm	49 µm	64 µm
MOIF	40 µm	50 µm	60 µm
Magnetic layer thickness	65 µm	75 µm	85 µm

Table 5.2: Parameter combinations for the simulation experiments. Combinations resulting in a good conformity with the measurement results for at least one measurement technique are highlighted in blue.

Simulation experiment	**Pole transition width**	**Measurement height**	**Magnetic layer thickness**
0	0	0	0
1	+	+	+
2	+	+	−
3	+	−	+
4	−	+	+
5	−	−	+
6	−	+	−
7	+	−	−
8	−	−	−

Table 5.3: Results of the simulated minimum and maximum stray field values B for SHPM and MOIF technique for different input parameter combinations.

Simulation	SHPM: simulated B_z		MOIF: simulated device response	
experiment	min. B [mT]	max. B [mT]	min. B [mT]	max. B [mT]
0	-71.95	73.20	-68.83	67.61
1	-63.66	63.94	-64.20	63.07
2	-53.67	54.05	-54.60	53.68
3	-88.52	88.89	-78.50	77.30
4	-67.38	67.73	-67.56	66.46
5	-90.62	90.98	-81.97	80.27
6	-56.80	57.08	-57.24	56.28
7	-74.54	74.83	-67.03	65.95
8	-76.25	76.53	-69.91	68.11

Simulation experiments leading to a satisfying congruence of measured and simulated data are highlighted in blue in the table. These simulation experiments comprise upper and lower boundaries for each parameter. However, a correlation of the measurement height and the magnetic layer thickness is highlighted. The results are only satisfying if they are shifted in the same direction. Two criteria are examined to decide if a simulation result represents the measured data sufficiently. First, the field amplitude in terms of minimum and maximum B must lie within the uncertainty range of the experimentally determined field amplitudes. For SHPM the amplitude range of [62.99 mT, 97.91 mT] is determined by the uncertainty of $\pm(7\,\mathrm{mT} + 13\,\%)$. The uncertainty of ± 2.5 mT of the MOIF measurement results in the range [66.08 mT, 71.08 mT]. Second, the overall simulated shape must fit the measured field distribution. For example, the simulated SHPM signal in simulation experiments 5 and 8 is more rectangular than the sinusoidal shape of the measured data. In both cases, no pole transition width and a rather small measurement height was assumed. Similar effects can be observed for the simulated MOIF device data, even if not as striking as for SHPM. Simulation experiments 4, 7 and 8 result in appropriate field amplitudes. While the field shape in 4 and 7 is more triangular, the shape in 8 is slightly more rounded. In 8 the in-plane field components are smaller due to the missing transition width and low measurement height. In 4 the influence of in-plane field components on the device response is larger because of the higher measurement height and in 7 the board transition width reduces the perpendicular field component. Both lead to a more triangular device response. Regarding SHPM, simulation experiments 1, 4 and 7 lead to a good overlap with the measured data. In general, a smaller

transition width, a lower measurement height and a larger sample thickness result in higher field amplitudes and less sharp behaviors. The range of minimal and maximal simulated B values for the blue denoted simulation experiments coincidence with the uncertainty budget of the measurements and show a good overlap in shape. For all simulation experiments the amount of minimum B is smaller than the amount of maximum B for SHPM, whereas it is the other way around for MOIF technique. This leads to the assumption of a systematic error in the offset correction for both measurements. However, the deviations are still within the uncertainty range of the measurements.

The above presented analysis of the influence of input parameter uncertainties on the simulation outcome is helpful to understand the comparison of the two measurement techniques SHPM and MOIF. The experimental data together with the best simulation results using parameters from column '0' in Table 5.1 are presented in Figure 5.1. Both measurement results match quite well considering the different measurement methods, the uncertainties of $\pm 2.5\,\mathrm{mT}$ for MOIF and $\pm(7\,\mathrm{mT} + 13\,\%)$ for SHPM and the fact that the data sets are not from the exact same position on the scale. The field amplitudes of the simulated SHPM result in terms of B_z lie with -71.95 mT and 73.20 mT within the range defined by the measured data of $80.45\,\mathrm{mT} \pm(7\,\mathrm{mT} + 13\,\%)$. Also, the amplitudes of the simulated MOIF device response fit with -68.83 mT and 67.61 mT perfectly the experimentally determined amplitude of $68.58\,\mathrm{mT} \pm 2.5\,\mathrm{mT}$. Likewise, the paths of the simulation results overlap nicely with the experimental data points. Due to the larger influence of in-plane field components on the MOIF device response in comparison to the Hall sensor response, it is difficult to directly compare the two measurement results. This is emphasized by the different shapes of the simulated responses. Given the measured data points, only the pole widths defined by the zero crossings of B and the amplitudes that are centered over the poles can be compared. The simulations offer another opportunity to relate the outcome of the two techniques. Before the MOIF device response could be calculated, all three sample stray field components B_x, B_y and B_z were simulated based on the measured MOIF device data. By achieving a good agreement between the MOIF device data and the MOIF device response after iterative simulation steps, the underlying perpendicular stray field component B_z can be rated as the real stray field component of the sample in this direction. Thus, it is exactly the field value that would be detected by SHPM. For the data sets and simulation results shown in Figure 5.1 both B_z shapes match. Consequently, the accuracy of the developed and calibrated methods SHPM and MOIF technique is proven and they can be used to measure the stray fields of magnetic microstructures with traceability to the SI unit Tesla.

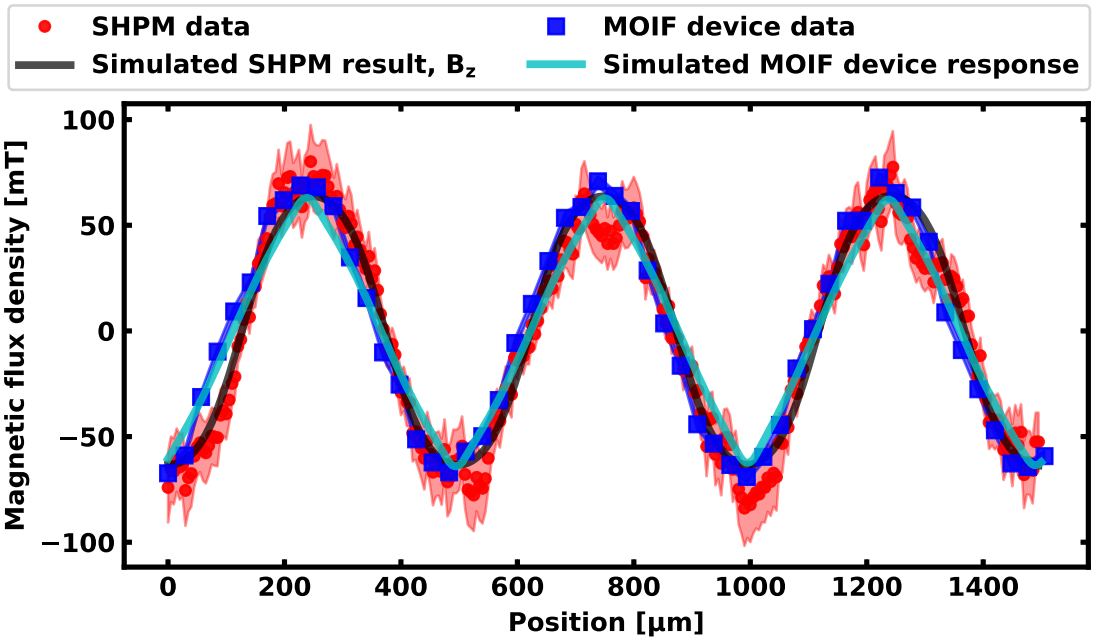

Figure 5.2: Simulation results of SHPM and MOIF technique for the parameter combination of simulation experiment 1 with $w = 125\,\mu\text{m}$, $z_{\text{SHPM}} = 64\,\mu\text{m}$, $z_{\text{MOIF}} = 60\,\mu\text{m}$ and $d = 85\,\mu\text{m}$.

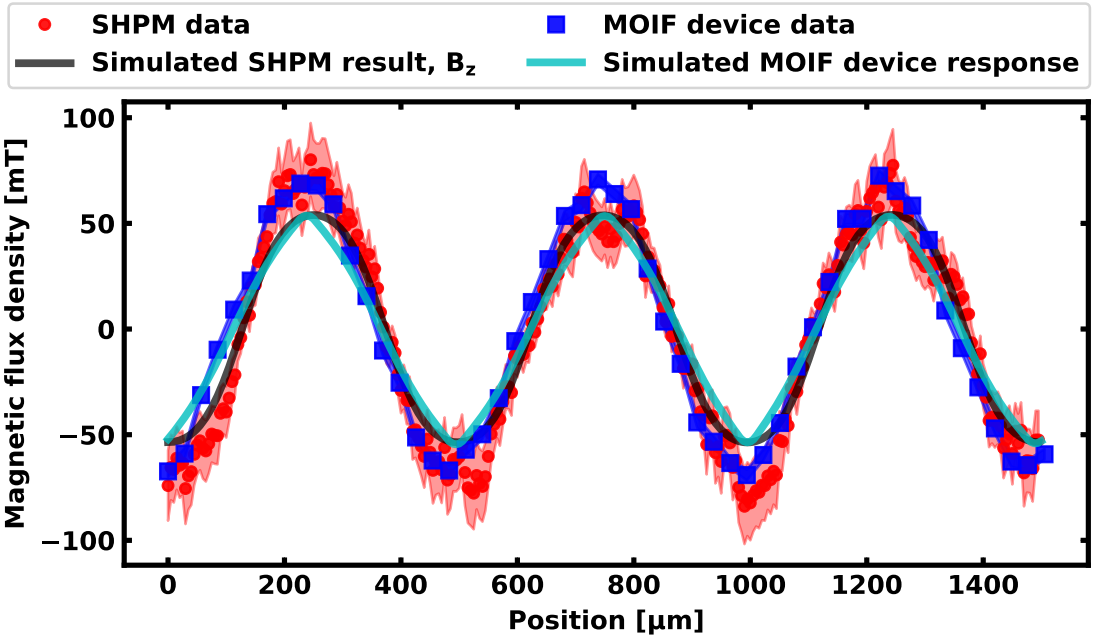

Figure 5.3: Simulation results of SHPM and MOIF technique for the parameter combination of simulation experiment 2 with $w = 125\,\mu\text{m}$, $z_{\text{SHPM}} = 64\,\mu\text{m}$, $z_{\text{MOIF}} = 60\,\mu\text{m}$ and $d = 65\,\mu\text{m}$.

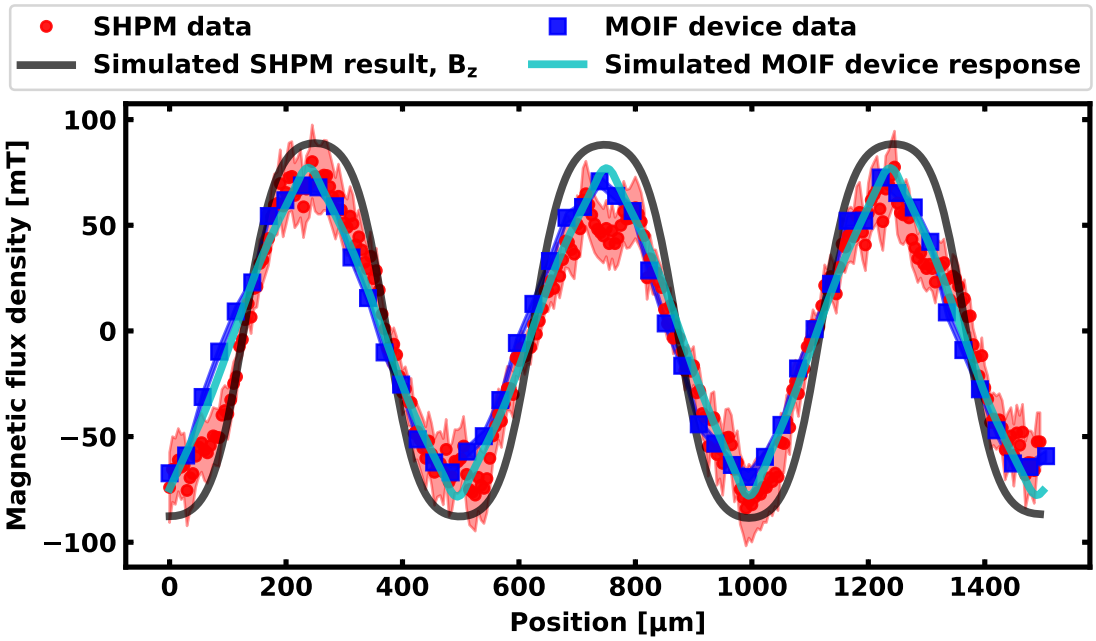

Figure 5.4: Simulation results of SHPM and MOIF technique for the parameter combination of simulation experiment 3 with $w = 125\,\mu\text{m}$, $z_{\text{SHPM}} = 34\,\mu\text{m}$, $z_{\text{MOIF}} = 40\,\mu\text{m}$ and $d = 85\,\mu\text{m}$.

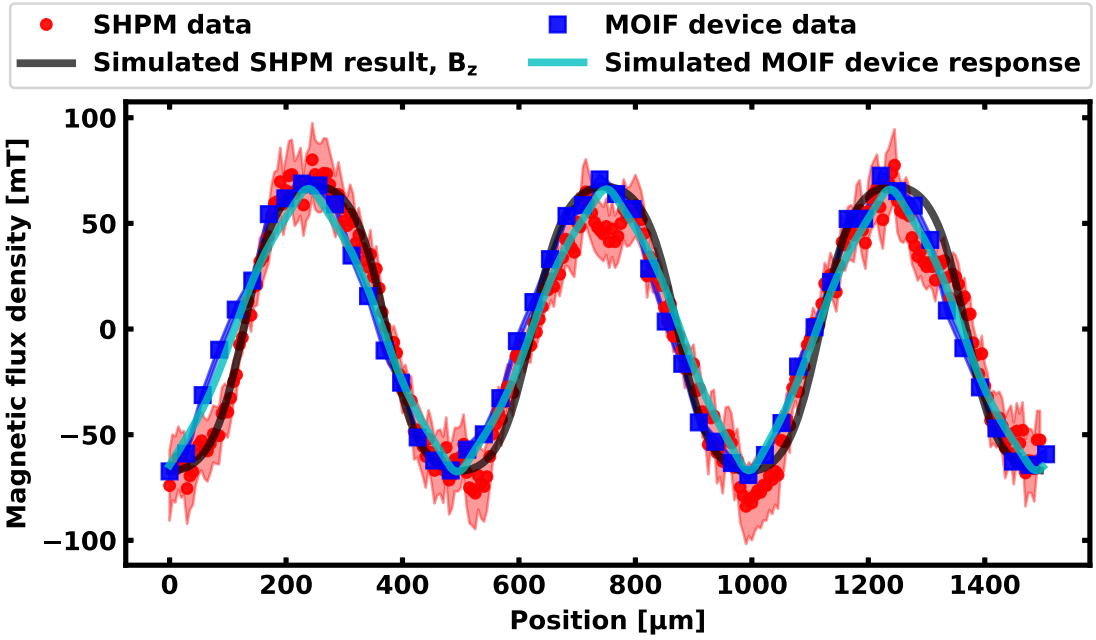

Figure 5.5: Simulation results of SHPM and MOIF technique for the parameter combination of simulation experiment 4 with $w = 0\,\mu\text{m}$, $z_{\text{SHPM}} = 64\,\mu\text{m}$, $z_{\text{MOIF}} = 60\,\mu\text{m}$ and $d = 85\,\mu\text{m}$.

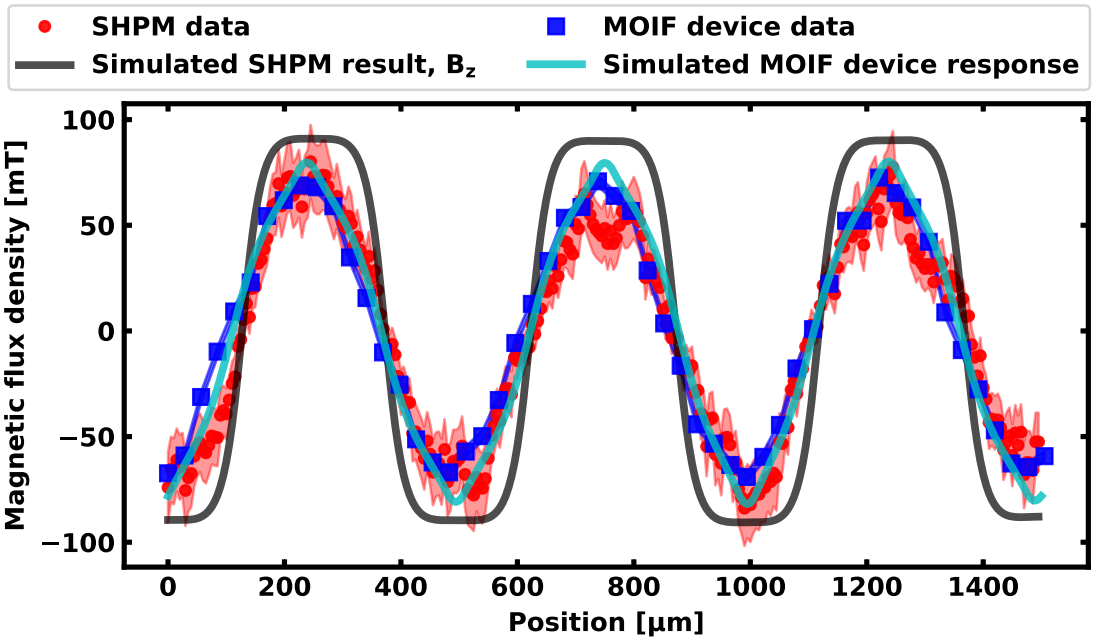

Figure 5.6: Simulation results of SHPM and MOIF technique for the parameter combination of simulation experiment 5 with $w = 0\,\mu\text{m}$, $z_{\text{SHPM}} = 34\,\mu\text{m}$, $z_{\text{MOIF}} = 40\,\mu\text{m}$ and $d = 85\,\mu\text{m}$.

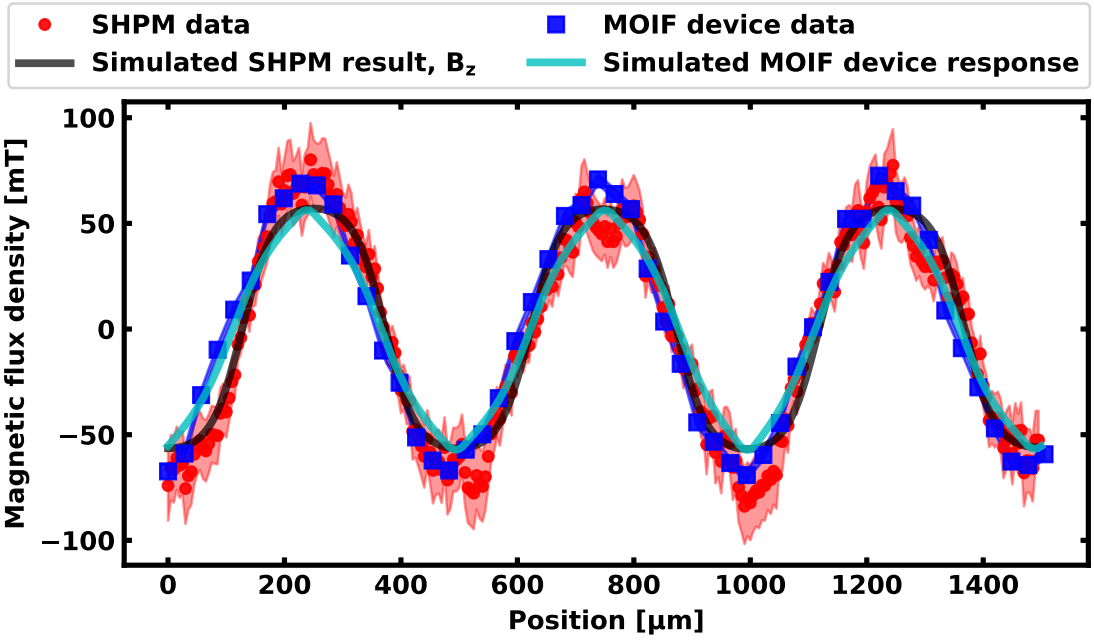

Figure 5.7: Simulation results of SHPM and MOIF technique for the parameter combination of simulation experiment 6 with $w = 0\,\mu\text{m}$, $z_{\text{SHPM}} = 64\,\mu\text{m}$, $z_{\text{MOIF}} = 60\,\mu\text{m}$ and $d = 65\,\mu\text{m}$.

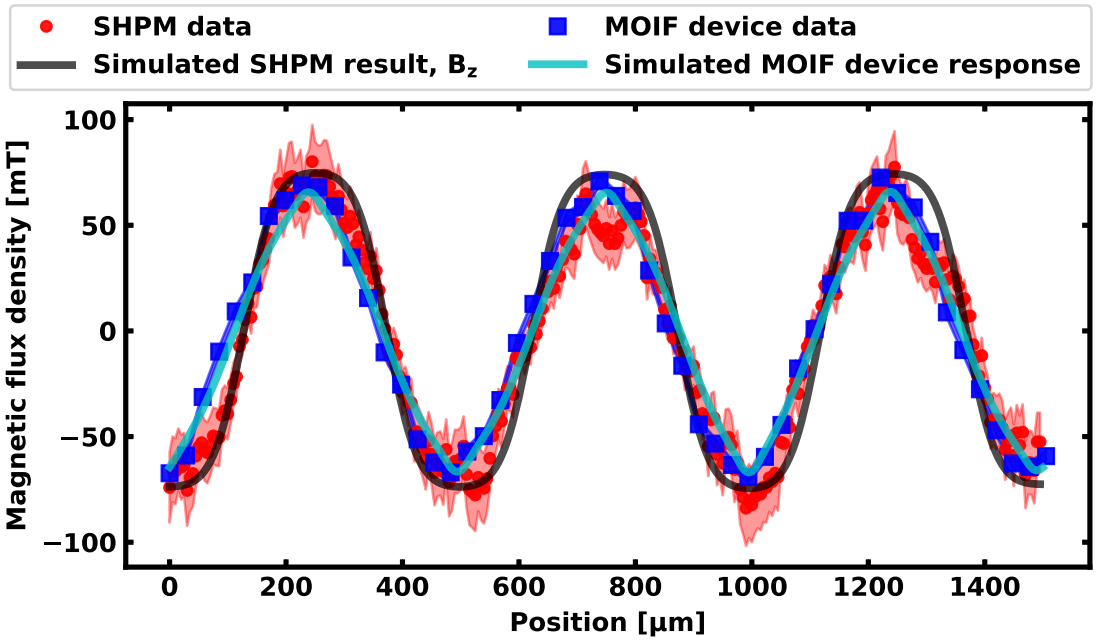

Figure 5.8: Simulation results of SHPM and MOIF technique for the parameter combination of simulation experiment 7 with $w = 125\,\mu\text{m}$, $z_{\text{SHPM}} = 34\,\mu\text{m}$, $z_{\text{MOIF}} = 40\,\mu\text{m}$ and $d = 65\,\mu\text{m}$.

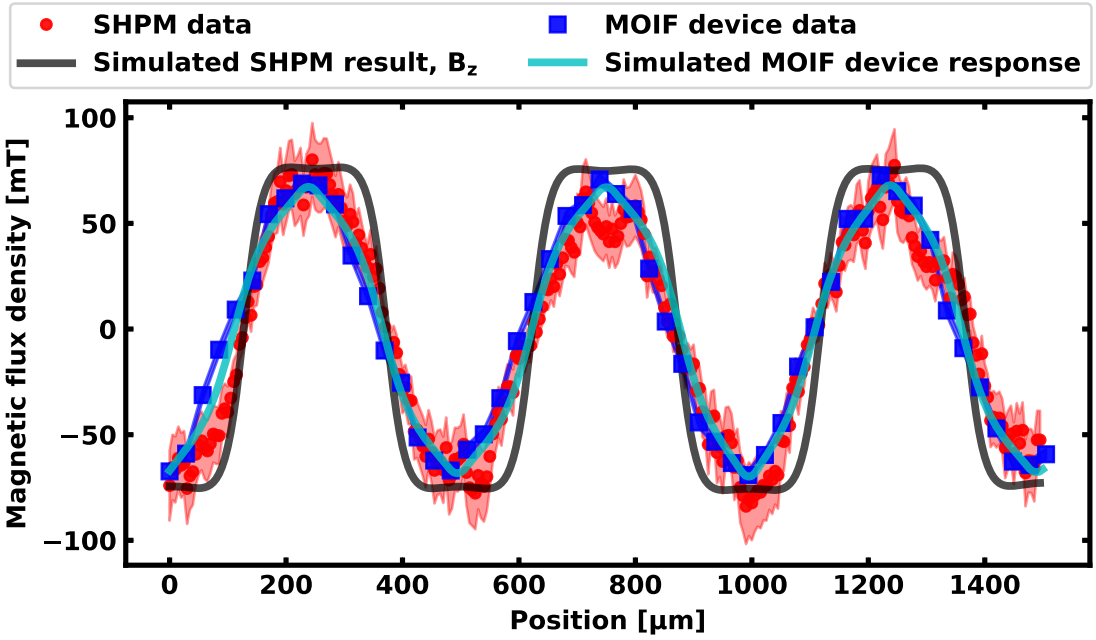

Figure 5.9: Simulation results of SHPM and MOIF technique for the parameter combination of simulation experiment 8 with $w = 0\,\mu\text{m}$, $z_{\text{SHPM}} = 34\,\mu\text{m}$, $z_{\text{MOIF}} = 40\,\mu\text{m}$ and $d = 65\,\mu\text{m}$.

6 Conclusion and Outlook

Two measurement techniques for traceable characterization of magnetic microstructures at room temperature (RT) were implemented and calibrated. The first is scanning Hall probe microscopy (SHPM) with a minimum measurement height of 4 µm, 5 µm spatial and 2 mT field resolution. It allows the characterization of magnetic microstructures down to the 10 µm range with their exponentially fast decaying stray fields with an increasing distance to the sample surface. The second is magneto-optical indicator film (MOIF) technique enabling fast characterization of magnetic microstructures over large areas. Here, the measurement height depends on the roughness and cleanness of the sample surface with a minimum of 5 µm. The spatial resolution is defined by the camera pixel size of 28 µm and the field resolution results to 2.5 mT for an averaging over 10 measurements.

To realize RT SHPM for magnetic microstructures, sensing materials were examined with respect to their sensitivity, stability and suitability for implementation into SHPM systems. To this end, Hall sensors made from gold and graphene with active area sizes from $5 \times 5\,\mu m^2$ down to $50 \times 50\,nm^2$ were fabricated. Their characterization revealed a sensitivity of 3.1 mV/(AT) for the gold sensors with a deviation of ±0.2 mV/(AT) between different sensors and batches. All measured sensors show a very good stability with a small long-term variation from start value of maximal 0.6 % over one year. The graphene sensors, in comparison, showed a roughly 400 000 – times larger sensitivity in the range from 500 V/(AT) to 1700 V/(AT). Also, the magnetic flux density resolution is better than for gold, with an average of 0.45 mT over the field and sensor range. However, they show a significantly reduced stability compared to gold sensors with a sensitivity change of up to 9.3 % from one day to another. Moreover, the placement of graphene Hall sensors on cantilever tips is not as straight forward as for gold. Accordingly, to accomplish SHPM gold Hall sensors on cantilever chips were integrated into an atomic force microscope. The SHPM performance was demonstrated by the exemplary characterization of a magnetic scale and a comparison of the results to simulations. For the calibration as well as for the measurement process a detailed uncertainty analysis was performed, yielding an extended uncertainty budget of ±(7 mT + 13 %).

The calibration of MOIF devices requires a systematic approach to determine the uncertainty budget which was demonstrated on the example of the commercial CMOS-MagView XL. First, the homogeneous and perpendicular stray field of an electromagnet utilized for the calibration was characterized. This revealed an uncertainty of the applied field of ±0.5 mT. Second,

the properties of the MOIF device itself were examined. The summarized contribution of noise, temperature and repeatability to the uncertainty was determined to ±1.85 % of the measured intensity. A calibration algorithm connecting the measured intensity with the magnetic field was established. In consideration of the before mentioned uncertainties as well as MOIF characteristics like uniaxial perpendicular and cubic magnetic anisotropies and inhomogeneous illumination, for the pixel-wise macroscopic calibration an uncertainty of ±1.18 mT was found. The influence of vectorial stray fields, especially in-plane stray field components, and sensor film thickness on the device response were incorporated in a microscopic calibration scheme that includes a simulation of the sample stray field. This principle was applied to the measurement of a magnetic scale. In the presented example the influence of the MOIF thickness was negligible due to the comparatively large sensor-sample distance, whereas a significant effect of in-plane stray field components on the measured magnetic field shape was detected.

The two traceable magnetic field measurement schemes for magnetic microstructures at RT were validated by a mutual comparison. Results form the measurement of the same magnetic scale with both methods were compared taking into account the uncertainty budgets as well as the simulation results. This led to a validation of not only the two implemented measurement schemes, SHPM and MOIF technique, but also of the developed calibration approaches. Thereby, two complementary quantitative measurement techniques for traceable measurements of magnetic microstructures at RT were provided in this work.

Outlook

The presented SHPM enables a characterization of magnetic microstructures with 5 µm spatial resolution in the xy-plane and at a minimum measurement height of 4 µm. A field resolution considering all uncertainty contributions of ±(7 mT + 13 %) was observed. The technique could in the future be further optimized to enable even the direct quantitative characterization of magnetic *nano*structures. Up to now, this is not possible with RT SHPM due to the two main challenges of realizing a sufficient signal to noise ratio and the precise positioning and operation of nano-sized Hall sensors. One option is to stabilize the carrier density in graphene with a capping layer out of aluminum dioxide or hexagonal boron nitride and a top gate. This would drastically decrease the uncertainty contribution of the Hall sensitivity. The thus stabilized graphene Hall sensors might be utilized for SHPM to increase the field resolution and the spatial resolution for nano sensors. To this end, cantilever chips must be fabricated out of the SiC substrate which is an ongoing development in cooperation with

PTB's group 'Scientific Instrumentation'. First tests of grinding and laser cutting the SiC substrate looked promising. Alternatively, the sensors could be implemented into a scanning system via a tuning fork approach. Another option is to improve the read-out electronics in terms of noise reduction and Hall voltage amplification. This would enable the application of nano-sized gold Hall sensors and thus an enhanced spatial resolution. The spatial resolution might also be improved by integrating gold and graphene Hall sensors into a metrological nanomeasuring machine [84] at PTB which accomplishes a more precise positioning with subnanometer accuracy in combination with a large scan range of 25 mm in the plane and 5 mm in the height enabling a traceable characterization of scientific and industrial relevant magnetic micro- and nanostructures.

A Explanation of exponential stray field decrease

In the following, the origin of the exponential stray field decrease stated in subsection 2.1.7 and section 3.6 is derived.

The magnetization of a ferromagnetic sample can be described by magnetic volume ρ and surface charges σ which are generated by the magnetic dipoles within the material. The magnetic stray field at a position r above the sample can be calculated by [85]

$$\boldsymbol{H}(r) = -\frac{1}{4\pi}\iiint \rho(r')\frac{r-r'}{|r-r'|^3}\mathrm{d}^3r' - \frac{1}{4\pi}\iint \sigma(r')\frac{r-r'}{|r-r'|^3}\mathrm{d}^2r' \,. \tag{A.1}$$

This is an integration over all dipoles in the magnetic sample. In the case of samples with perpendicular magnetization that is homogeneous over the sample thickness, as considered within this work, the contribution of the volume charges to the stray field is zero. The surface charges are connected to the magnetization by

$$\sigma = \boldsymbol{n} \cdot \boldsymbol{M} \tag{A.2}$$

where $\boldsymbol{n}$ is the vector normal to the sample surface. In the Fourier space the spatial integration in three dimensions is substituted by multiplications with prefacors called transfer functions. Thus, the calculation of the sample stray field from a given magnetization can be performed with low numerical effort. This method is particularly effective for planar samples when the sample dimensions are much larger than the measurement height. In this instance, the sample can be approximated as infinitely extended in comparison to the sensor and effects from the sample boundaries can be neglected. Utilizing the magnetic potential Φ, which is related to the magnetization by

$$\nabla^2\Phi = -\nabla \cdot \boldsymbol{M}, \tag{A.3}$$

the sample stray field can be calculated with $\boldsymbol{H} = -\nabla\Phi$. In the magnetostatic case without currents or varying electric fields above the sample this leads to the Laplace equation for the

magnetic potential $\nabla^2\Phi = 0$ because in the area above the sample exists no magnetization. In two-dimensional Fourier space this is expressed by [86]

$$-k_x^2\Phi(\boldsymbol{k}, z) - k_y^2\Phi(\boldsymbol{k}, z) + \frac{\partial^2\Phi(\boldsymbol{k}, z)}{\partial z^2} = 0\,. \tag{A.4}$$

A solution for this Laplace equation that realizes a vanishing potential with increasing distance to the sample is [86]

$$\Phi(\boldsymbol{k}, z) = \Phi(\boldsymbol{k}, 0) \cdot e^{-kz}\,. \tag{A.5}$$

Consequently, the magnetic stray field in Fourier space can be calculated with

$$\boldsymbol{H}(\boldsymbol{k}, z) = -\nabla\Phi(\boldsymbol{k}, z) = -\begin{pmatrix} ik_x \\ ik_y \\ -k \end{pmatrix} \Phi(\boldsymbol{k}, 0) \cdot e^{-kz}\,. \tag{A.6}$$

The further solution of this equation leads to the magnetization dependent stray field equations presented in Equation 2.22 to Equation 2.24. [48]

For a sinusoidal magnetic potential, the Fourier transform of the potential is a delta function at one k-vector. In this case, it is clearly visible from Equation A.6 that each stray field component H_x, H_y and H_z decays exponentially with increasing distance from the sample z [1, 2]. The magnetic structure investigated within this work is a magnetic scale featuring a rectangular structure of up and down magnetized poles. The rectangular magnetization can be approximated by linear combinations of sine functions. The fundamental sine function has the same periodicity as the rectangular signal. Higher harmonics with a lower amplitude are added to this fundamental sine wave until the resulting wave shows a rectangular shape. Thus, the decrease of each stray field component is a combination of the exponentially decrease for each k-vector representing the fundamental sine function and its higher harmonics. In Equation A.6 also a exponential decrease with increasing k is identifiable. Hence, contributions from higher k-vectors decay faster with increasing distance to the sample than the contributions from smaller k-vectors. The dominant k-vector belonging to the largest amplitude of the Fourier-transformed stray field is caused by the fundamental sine wave. Consequently, the decrease of each magnetic stray field component can be approximated by an exponential decay. This exponential behavior is preserved by the inverse Fourier transformation into real space.

B Fabrication details and parameters

In the following the fabrication steps for gold and graphene Hall sensors are described in detail. In addition to section 3.1 the parameters for each step are given.

B.1 Gold

The fabrication of gold Hall sensors consists of two steps: (i) active layer and (ii) contact layer. For each step the following sub-steps have to be performed:

1. Cleaning
   The wafer is laid in acetone and ultrasonic power is applied for 5 min. Then, the wafer is sluiced with isopropyl and blown dry with nitrogen. Additionally, the smaller Si_3N_4 wafers for the Hall sensors on cantilevers must be glued to a 3 inch wafer to fit into the EBL machine.

2. Resist deposition
   PMMA based electron beam resist combinations from Allresist GmbH [59] are deposited via spin coating and are tempered on a hot plate. The details and parameters for each step are given in Table B.3.

Table B.1: Parameters for resist deposition.

Step	Resist	Thickness [nm]	Spinning rate [rpm]	Spinning time [s]	Heating temperature [°C]	Heating time [min]
(i)	AR-P 642.03	80	3000	45	160	10
	AR-P 672.01	40	2000	45	160	10
(ii)	AR-P 642.03	90	2000	45	160	10
	AR-P 672.01	40	2000	45	160	10

3. Electron beam exposure
   Structures are written into the resists by the electron beam machine.

4. Developing
   The resists are developed with a solution containing 10 ml methyl ethyl ketone, 247.5 ml Methyl isobutyl ketone and 742.5 ml isoprpyl for 60 s. The process is stopped by 60 s in isopropyl and the wafer is dried with nitrogen.

5. Metalization
   The metallic layers are deposited by electron beam evaporation. The details for each fabrication step are given in Table B.5.

Table B.2: Parameters for the metalization step.

Step	Metal	Thickness [nm]	Evaporation rate [Å/s]
(i)	Titanium	5	1
	Gold	30	1
(ii)	Gold	50	1

6. Lift-off
   The wafer lies in an acetone bath for at least 15 hours.

Finally, the cleaning sub-step is performed again and the Hall sensor fabrication is finished.

B.2 Graphene

The fabrication of graphene Hall sensors consists of five steps: (i) adhering contact, (ii) small structure etch, (iii) etch, (iv) final contact and (v) passivation. Each step is a combination of different sub-steps as indicated below. For the final step, only the sub-steps 1 and 2 are conducted.

1. Cleaning
   The graphene sample and a 3 inch wafer with a titanium gold layer structure are laid in acetone and ultrasonic power is applied for 5 min. Then, both are sluiced with isopropyl and blown dry with nitrogen. The graphene sample is glued to the wafer to fit into the fabrication machines.

2. Resist deposition

   PMMA based electron beam resist combinations from Allresist GmbH [59, 60] and Kayaku Advanced Materials, Inc. [71] are deposited via spin coating and are tempered on a hot plate. The details and parameters for each step are given in Table B.3.

Table B.3: Parameters for resist deposition.

Step	Resist	Thickness [nm]	Spinning rate [rpm]	Spinning time [s]	Heating temperature [°C]	Heating time [min]
(i)	AR-P 641.03 AR-P 672.06	95 360	6000 6000	60 60	160 160	10 10
(ii)	AR-P 672.06 AR-PC 5090.02	360 60	6000 2000	45 45	160 90	10 2
(iii)	AR-P 672.06 AR-PC 5090.02	360 60	6000 2000	45 45	160 90	10 2
(iv)	AR-P 641.03 AR-P 671.01 AR-PC 5090.02	95 40 60	6000 2000 2000	60 45 45	160 160 90	10 10 2
(v)	CoPo EL3	55	4000	45	160	10

3. Chromium deposition

   During step (i) a chromium layer is deposited on top of the PMMA resists. This conducting layer prevents charging of the sample and enables a precise definition of markers for the electron beam machine. The deposition parameters are given in Table B.4.

Table B.4: Parameters for the conducting chromium layer deposition.

Step	Metal	Thickness [nm]	Evaporation rate [Å/s]
(i)	Chromium	20	0.6

4. Electron beam exposure

   Structures are written into the resists by the electron beam machine.

5. Chromium etch

   Within step (i) the chromium must be removed before the PMMA resists can be developed. For this purpose the wafer with the graphene sample is pivoted in a

chomium etch for 30 s. The process is stopped placing the wafer in a constant water flow for 60 s. Then, the sample is dried with nitrogen.

6. Conducting resist dissolution
   In steps (ii), (iii) and (iv) the conducting resist AR-PC 5090.02 is dissolved by a constant water flow for 60 s. The wafer is dried with nitrogen.

7. Developing
   The resists are developed with a solution containing 10 ml methyl ethyl ketone, 247.5 ml Methyl isobutyl ketone and 742.5 ml isoprpyl for 60 s. The process is stopped by 60 s in isopropyl and the wafer is dried with nitrogen.

8. Etching
   In steps (i), (ii) and (iii) the graphene is etched by AC oxigen plasma etching at a power of -100 V and a pressure of 8 Pa for 150 s. A gas flow of 27 sccm argon and 3 sccm oxigen is used.

9. Metalization
   The metallic layers are deposited by electron beam evaporation. The details for the appropriate fabrication steps are given in Table B.5.

Table B.5: Parameters for the metalization step.

Step	Metal	Thickness [nm]	Evaporation rate [Å/s]
(i)	Titanium	10	1
	Gold	30	1
(iv)	Gold	50	1

10. Lift-off
    The wafer lies in an acetone bath for at least 15 hours.

List of Abbrevations

AFM	atomic force microscope
Al	aluminum
Au	gold
Bi	bismuth
Bi-REIG	bismuth-substitued rare earth iron garnet
CEA	Commissariat à l'énergie atomique et aux énergies alternatives
CMOS	complementary metal oxide semiconductor
CPW	coplanar waveguide
DFT	discrete Fourier transformation
EBL	electron beam lithography
FMR	ferromagnetic resonance
GUM	Guide to the expression of uncertainty in measurement
KOH	potassium hydroxide
MFM	magnetic force micorscopy
MOIF	magneto-optical indicator film
NIST	National Institute of Standards and Technology
PCB	printed circuit board
PMMA	polymethyl mathacrylate
PDF	probability density function
PTB	Physikalisch-Technische Bundesanstalt
RE	rare earth
RIE	reactive ion etching
RT	room temperature
SEM	scanning electron microscope
SHPM	scanning Hall probe microscopy
SiC	silicon carbide
Si_3N_4	silicon nitride
SPM	scanning probe microscopy
SQUID	superconducting quantum interference device
TF	transfer function
VNA	vector network analyzer

List of Symbols

Symbol	*Name*	*Unit*
$\vec{B}$, B	magnetic flux density	T
B_{ext}	applied static magnetic flux density	T
B_{MagView}	magnetic flux density measured by CMOS-MagView XL	T
B_{meas}	measured magnetic flux density	T
B_{Sample}	magnetic flux density of a sample	T
$B_{\mathrm{ext}}^{\mathrm{set}}$	nominal value of applied static magnetic flux density	T
$B_{\mathrm{x/y/z}}$	magnetic flux density in x-, y- or z-direction	T
c	constant	
d	sample thickness	m
$\vec{E}$, E	electric field	V/m
e	electron charge	C
F	free energy	J
F_{c}	cubic anisotropy	J
F_{demag}	demagnetization energy	J
F_{L}	Lorentz force	N
F_{uip}	uniaxial in-plane anisotropy	J
F_{uoop}	uniaxial out-of-plane anisotropy	J
F_{zee}	Zeeman energy	J
f_{res}	resonance frequency	Hz
g	g-factor	–
H	magnetic field	A/m
$\boldsymbol{H}_{\mathrm{eff}}$	effective magnetic field	A/m
$\hbar$	Planck constant	Js
I	current	A
I	intensity	a.u.
I_0	light intensity before a polarizing filter	a.u.

Symbol	*Name*	*Unit*
K_c	cubic anisotropy constant	T^2
K_uip	uniaxial in-plane anisotropy constant	T^2
K_uoop	uniaxial out-of-plane anisotropy constant	T^2
$\boldsymbol{k}$	wave vector	m^{-1}
k_1	fit parameter	
k_2	fit parameter	
l	length	m
M	magnetization	A/m
M_MOIF	magnetization of the MOIF	A/m
M_R	remanence magnetization	A/m
M_S	saturation magnetization	A/m
$M_\mathrm{S,MOIF}$	saturation magnetization of the MOIF	A/m
M_z	magnetization in z-direction	A/m
$M_\mathrm{z,MOIF}$	magnetization of the MOIF in z-direction	A/m
$\boldsymbol{m}$	magnetic dipole moment	Vsm
$N_{x/y/z}$	demagnetization tensor in x-, y- or z-direction	–
n	electron density	cm^{-3}
q	charge	C
S	sensitivity	m^2/s
T	temperature	°C
T_D	damping torque	Nm
T_hf	torque generated by high frequency magnetic field	Nm
t	thickness of sensing layer	m
V_Hall	Hall voltage	V
V_offset	Hall voltage offset	V
$\vec{v}$	velocity	m/s
w	pole transition width	m
z	height	m

Symbol	*Name*	*Unit*
α	damping parameter	Vm
α_0	angle between polarizing filters	rad (or °)
β	Faraday rotation angle	rad (or °)
γ	gyromagnetic ratio	rad/(sT)
ΔB_{meas}	change of measured intensity	a.u.
ΔS_{rel}	relative sensitivity change	m^2/s
ΔT	temperature change	°C
$\Delta V_{\mathrm{offset}}$	change of Hall voltage offset	V
θ	angle to the plain normal	rad (or °)
θ_{H}	angle to the plain normal of magnetic field	rad (or °)
θ_{M}	angle to the plain normal of the magnetization	rad (or °)
μ_0	vacuum permeability	H/m
μ_{B}	Bohr magneton	Vms
ν	Verdet constant	rad/(Tm)
ϕ	angle in the plane (of the magnetization)	rad (or °)
ϕ_{c}	angle of cubic anisotropy axis	rad (or °)
ϕ_{u}	angle of uniaxial anisotropy axis	rad (or °)
χ	angle in the plane (of magnetic field)	rad (or °)
ω	angular frequency	s^{-1}

List of Figures

1.1 Stray field properties of magnetic microstructures. 2

2.1 Schematic visualizing the Hall effect. 7
2.2 Visualization of the magneto-optical Faraday effect. 8
2.3 Schematic drawing of the MOIF device operation principle. 9
2.4 Coordinate system introducing the angles between the magnetic field $\boldsymbol{H}$ and the magnetization $\boldsymbol{M}$ and the axes of the system. 12
2.5 Astroid illustrating the critical curve of a out-of-plane uniaxial anisotropy. . 13
2.6 Schematic of fields and torques affecting a magnetic dipole under ferromagnetic resonance condition. 15
2.7 Schematic of the FMR setup with a rotatable electromagnet. 15
2.8 Approximation of a sample magnetization distribution from measured stray field data. 18
2.9 Stray field simulation process. 20
2.10 Simulated perpendicular stray field component at different distances to the sample surface. 22
2.11 Exponential decrease of the field amplitude with increasing measurement height. 23
2.12 Graphene lattice structure and Brillouin zone. 26
2.13 Band structure of graphene near the Fermi energy depicted in the reciprocal-space. 27

3.1 Schematic of the lift-off process. 30
3.2 Layer structure and SEM image of a gold Hall sensor. 32
3.3 Schematic gold Hall sensor on cantilever chip and SEM image. 33
3.4 Layer structure and SEM images of a graphene Hall sensor. 34
3.5 Typical calibration curves of gold and graphene Hall sensors. 37
3.6 Temperature dependence of Hall sensitivity and offset voltage for gold and graphene. 38
3.7 Integration of gold Hall sensor on cantilever chip into scanning system. . . . 40
3.8 Schematic of the AFM-SHPM measurement principle. 40
3.9 Histogram indicating the roughness of the magnetic scale SST250HFA04. . . 42
3.10 Height dependent SHPM of a magnetic scale. 43
3.11 SHPM results in tapping mode leading to an averaged measurement height of 4 µm. 44
3.12 Traceable SHPM data with uncertainty budget compared to simulated stray field values. 46
3.13 Simulated stray field decay with increasing measurement height. 49
3.14 k-vector dependent Fourier transform of $B_z((k_x, 0), z)$ at a distance to the sample surface of $z = 4\,\mu\text{m}$, $z = 40\,\mu\text{m}$ and $z = 400\,\mu\text{m}$. 50

4.1 Electromagnet utilized for the calibration. 53

4.2 Temperature dependence and homogeneity of the electromagnet. 54
4.3 Ishikawa diagram summarizing uncertainty contributions of the CMOS-MagView XL calibration for perpendicular homogeneous magnetic stray fields. 56
4.4 MOIF hysteresis at 31.85 °C. 58
4.5 Temperature dependent saturation magnetization of the MOIF. 59
4.6 FMR frequency spectrum of the MOIF. 60
4.7 Resonance frequency f_{res} of the homogeneous mode of MOIF. 61
4.8 Temperature dependence of the MOIF anisotropy fields and visualization of anisotropy shapes. 62
4.9 Relation between $\cos\theta$ which is proportional to the out-of-plane component of the MOIF magnetization M_z and an external, homogeneous and perpendicular magnetic flux density. 63
4.10 Polynomial fit of the calibration data. 64
4.11 Values for the fitted k parameters from the calibration data. 65
4.12 MOIF measurement of magnetic scale and discrimination image. 70
4.13 Comparison of simulation and MOIF measurement of a magnetic scale. . . . 71

5.1 Comparison measurement. 74
5.2 Simulation results of SHPM and MOIF technique for the parameter combination of simulation experiment 1 with $w = 125\,\mu\mathrm{m}$, $z_{\mathrm{SHPM}} = 64\,\mu\mathrm{m}$, $z_{\mathrm{MOIF}} = 60\,\mu\mathrm{m}$ and $d = 85\,\mu\mathrm{m}$. 78
5.3 Simulation results of SHPM and MOIF technique for the parameter combination of simulation experiment 2 with $w = 125\,\mu\mathrm{m}$, $z_{\mathrm{SHPM}} = 64\,\mu\mathrm{m}$, $z_{\mathrm{MOIF}} = 60\,\mu\mathrm{m}$ and $d = 65\,\mu\mathrm{m}$. 78
5.4 Simulation results of SHPM and MOIF technique for the parameter combination of simulation experiment 3 with $w = 125\,\mu\mathrm{m}$, $z_{\mathrm{SHPM}} = 34\,\mu\mathrm{m}$, $z_{\mathrm{MOIF}} = 40\,\mu\mathrm{m}$ and $d = 85\,\mu\mathrm{m}$. 79
5.5 Simulation results of SHPM and MOIF technique for the parameter combination of simulation experiment 4 with $w = 0\,\mu\mathrm{m}$, $z_{\mathrm{SHPM}} = 64\,\mu\mathrm{m}$, $z_{\mathrm{MOIF}} = 60\,\mu\mathrm{m}$ and $d = 85\,\mu\mathrm{m}$. 79
5.6 Simulation results of SHPM and MOIF technique for the parameter combination of simulation experiment 5 with $w = 0\,\mu\mathrm{m}$, $z_{\mathrm{SHPM}} = 34\,\mu\mathrm{m}$, $z_{\mathrm{MOIF}} = 40\,\mu\mathrm{m}$ and $d = 85\,\mu\mathrm{m}$. 80
5.7 Simulation results of SHPM and MOIF technique for the parameter combination of simulation experiment 6 with $w = 0\,\mu\mathrm{m}$, $z_{\mathrm{SHPM}} = 64\,\mu\mathrm{m}$, $z_{\mathrm{MOIF}} = 60\,\mu\mathrm{m}$ and $d = 65\,\mu\mathrm{m}$. 80
5.8 Simulation results of SHPM and MOIF technique for the parameter combination of simulation experiment 7 with $w = 125\,\mu\mathrm{m}$, $z_{\mathrm{SHPM}} = 34\,\mu\mathrm{m}$, $z_{\mathrm{MOIF}} = 40\,\mu\mathrm{m}$ and $d = 65\,\mu\mathrm{m}$. 81
5.9 Simulation results of SHPM and MOIF technique for the parameter combination of simulation experiment 8 with $w = 0\,\mu\mathrm{m}$, $z_{\mathrm{SHPM}} = 34\,\mu\mathrm{m}$, $z_{\mathrm{MOIF}} = 40\,\mu\mathrm{m}$ and $d = 65\,\mu\mathrm{m}$. 81

List of Tables

3.1 Properties of 5 µm gold and graphene Hall sensors. 36
3.2 Influence of the temperature dependence of Hall sensitivity and offset Hall voltage on sensitivity uncertainty and on the uncertainty of the magnetic flux density measured with the sensors for gold and graphene. 39

5.1 Input parameters of the simulations and their boundaries defining the uncertainty range. 75
5.2 Parameter combinations for the simulation experiments. Combinations resulting in a good conformity with the measurement results for at least one measurement technique are highlighted in blue. 75
5.3 Results of the simulated minimum and maximum stray field values B for SHPM and MOIF technique for different input parameter combinations. . . . 76

B.1 Parameters for resist deposition. 87
B.2 Parameters for the metalization step. 88
B.3 Parameters for resist deposition. 89
B.4 Parameters for the conducting chromium layer deposition. 89
B.5 Parameters for the metalization step. 90

References

[1] P. J. A. van Schendel, *Investigation of Magnetization Structures in Ferromagnetic and Superconducting Samples by Magnetic Force Microscopy*. PhD thesis, University Basel, 1999.

[2] C. Schönenberger and S. F. Alvarado, "Understanding magnetic force microscopy," *Z. Phys. B-Condensed Matter*, vol. 80, pp. 373–383, 1990.

[3] G. Shaw, K. Kramer, N. M. Dempsey, K. Hasselbach, R. B. G. Kramer, N. M. Dempsey, and K. Hasselbach, "A Scanning Hall Probe Microscope for high resolution, large area, variable height Magnetic Field Imaging," *Review of Scientific Instruments*, vol. 87, p. 113702, nov 2016.

[4] S. Sonusen, O. Karci, M. Dede, S. Aksoy, and A. Oral, "Single layer graphene Hall sensors for scanning Hall probe microscopy (SHPM) in 3–300K temperature range," *Applied Surface Science*, vol. 308, pp. 414–418, jul 2014.

[5] A. Sandhu, K. Kurosawa, M. Dede, and A. Oral, "50 nm Hall Sensors for Room Temperature Scanning Hall Probe Microscopy," *Japanese Journal of Applied Physics*, vol. 43, pp. 777–778, feb 2004.

[6] J. McCord, "Progress in magnetic domain observation by advanced magneto-optical microscopy," *Journal of Physics D: Applied Physics*, vol. 48, p. 333001, aug 2015.

[7] C. Jooss, J. Albrecht, H. Kuhn, S. Leonhardt, and H. Kronmüller, "Magneto-optical studies of current distributions in high-T_C superconductors," *Reports on Progress in Physics*, vol. 65, pp. 651–788, may 2002.

[8] NanoMagnetics Instruments, "RT-SHPM Room Temperature Scanning Hall Probe Microscope," *https://www.nanomagnetics-inst.com*, jul 2017.

[9] NanoMagnetics Instruments, "micro-Hall Probes & micro-Hall Probe Gaussmeter," *https://www.nanomagnetics-inst.com*, jul 2017.

[10] T. Takezaki and K. Sueoka, "Quantitative current measurements using scanning magnetoresistance microscopy," *Ultramicroscopy*, vol. 108, pp. 970–974, aug 2008.

[11] M. Costa, J. Gaspar, R. Ferreira, E. Paz, H. Fonseca, M. Martins, S. Cardoso, and P. P. Freitas, "Integration of Magnetoresistive Sensors With Atomic Force Microscopy Cantilevers for Scanning Magnetoresistance Microscopy Applications," *IEEE Transactions on Magnetics*, vol. 51, pp. 1–4, nov 2015.

[12] O. Kazakova, R. Puttock, C. Barton, H. Corte-León, M. Jaafar, V. Neu, and A. Asenjo, "Frontiers of magnetic force microscopy," *Journal of Applied Physics*, vol. 125, p. 060901, feb 2019.

[13] X. K. Hu, G. Dai, S. Sievers, V. Neu, and H. W. Schumacher, "Uncertainty Propagation and Evaluation of Nano-Scale Stray Field in Quantitative Magnetic Force Microscopy Measurements," in *2018 Conference on Precision Electromagnetic Measurements (CPEM 2018)*, pp. 1–2, IEEE, jul 2018.

[14] M. Dede, R. Akram, and A. Oral, "3D scanning Hall probe microscopy with 700 nm resolution," *Applied Physics Letters*, vol. 109, p. 182407, oct 2016.

[15] C. W. Hicks, L. Luan, K. A. Moler, E. Zeldov, and H. Shtrikman, "Noise characteristics of 100 nm scale GaAs/$Al_xGa_{1-x}As$ scanning Hall probes," *Applied Physics Letters*, vol. 90, p. 133512, mar 2007.

[16] B. Chenaud, A. Segovia-Mera, A. Delgard, N. Feltin, A. Hoffmann, F. Pascal, W. Zawadzki, D. Mailly, and C. Chaubet, "Sensitivity and noise of micro-Hall magnetic sensors based on InGaAs quantum wells," *Journal of Applied Physics*, vol. 119, p. 024501, jan 2016.

[17] A. Pross, A. I. Crisan, S. J. Bending, V. Mosser, and M. Konczykowski, "Second-generation quantum-well sensors for room-temperature scanning Hall probe microscopy," *Journal of Applied Physics*, vol. 97, p. 096105, may 2005.

[18] K. S. Novoselov, S. V. Morozov, S. V. Dubonos, M. Missous, A. O. Volkov, D. A. Christian, and A. K. Geim, "Submicron probes for Hall magnetometry over the extended temperature range from helium to room temperature," *Journal of Applied Physics*, vol. 93, pp. 10053–10057, jun 2003.

[19] T. Ciuk, B. Stanczyk, K. Przyborowska, D. Czolak, A. Dobrowolski, J. Jagiello, W. Kaszub, M. Kozubal, R. Kozlowski, and P. Kaminski, "High-Temperature Hall Effect Sensor Based on Epitaxial Graphene on High-Purity Semiinsulating 4H-SiC," *IEEE Transactions on Electron Devices*, vol. 66, pp. 3134–3138, jul 2019.

[20] L. Huang, Z. Zhang, B. Chen, X. Ma, H. Zhong, and L.-M. Peng, "Ultra-sensitive graphene Hall elements," *Applied Physics Letters*, vol. 104, p. 183106, may 2014.

[21] C.-C. Tang, M.-Y. Li, L. J. Li, C. C. Chi, and J. C. Chen, "Characteristics of a sensitive micro-Hall probe fabricated on chemical vapor deposited graphene over the temperature range from liquid-helium to room temperature," *Applied Physics Letters*, vol. 99, p. 112107, sep 2011.

[22] J. Dauber, A. A. Sagade, M. Oellers, K. Watanabe, T. Taniguchi, D. Neumaier, and C. Stampfer, "Ultra-sensitive Hall sensors based on graphene encapsulated in hexagonal boron nitride," *Applied Physics Letters*, vol. 106, p. 193501, may 2015.

[23] Y. Kabanov, A. Zhukov, V. Zhukova, and J. Gonzalez, "Magnetic domain structure of wires studied by using the magneto-optical indicator film method," *Applied Physics Letters*, vol. 87, p. 142507, oct 2005.

[24] A. Lucarelli, G. Lüpke, T. J. Haugan, G. A. Levin, and P. N. Barnes, "Time-resolved magneto-optical imaging of $Y_1Ba_2Cu_3O_{7-\delta}$ thin films in high-frequency AC current regime," *Superconductor Science and Technology*, vol. 19, pp. 667–670, jun 2006.

[25] S. Dreyer, J. Norpoth, C. Jooss, S. Sievers, U. Siegner, V. Neu, and T. H. Johansen, "Quantitative imaging of stray fields and magnetization distributions in hard magnetic element arrays," *Journal of Applied Physics*, vol. 101, p. 083905, apr 2007.

[26] C. Jooss and V. Born, "Determination of electric field distributions in superconductors via magneto-optical imaging and the Faraday law," *Physical Review B*, vol. 73, p. 094508, mar 2006.

[27] Z. W. Lin, J. G. Zhu, Y. G. Guo, X. L. Wang, S. X. Dou, T. H. Johansen, X. Shi, and K. Y. Choi, "Flux distribution in Fe-based superconducting materials by magneto-optical imaging," *Journal of Applied Physics*, vol. 111, p. 07E143, apr 2012.

[28] F. Laviano, D. Botta, A. Chiodoni, R. Gerbaldo, G. Ghigo, L. Gozzelino, S. Zannella, and E. Mezzetti, "An improved method for quantitative magneto-optical analysis of superconductors," *Superconductor Science and Technology*, vol. 16, pp. 71–79, jan 2003.

[29] C. Liu, X. Zhang, and Y.-H. Zhou, "A novel design for magneto-optical microscopy and its calibration," *Measurement Science and Technology*, vol. 30, p. 115904, nov 2019.

[30] G. Shaw, J. Brisbois, L. B. G. L. Pinheiro, J. Müller, S. Blanco Alvarez, T. Devillers, N. M. Dempsey, J. E. Scheerder, J. Van de Vondel, S. Melinte, P. Vanderbemden, M. Motta, W. A. Ortiz, K. Hasselbach, R. B. G. Kramer, and A. V. Silhanek, "Quantitative magneto-optical investigation of superconductor/ferromagnet hybrid structures," *Review of Scientific Instruments*, vol. 89, p. 023705, feb 2018.

[31] Matesy Magnetic Technologies & Systems, "cmos-magview - Magnetfelder sichtbar machen," *https://matesy.de*, apr 2018.

[32] Innovent Technologieentwicklung Jena, "Magnetooptik," *https://www.innovent-jena.de*, apr 2019.

[33] E. H. Hall, "On a New Action of the Magnet on Electric Currents," *American Journal of Mathematics*, vol. 2, p. 287, sep 1879.

[34] S. Blundell, *Magnetism in Condensed Matter*. New York: Oxford University Press Inc., 2001.

[35] R. A. Serway and J. W. Jewett, *Physics for scientists and engineers.* Thomson-Brooks/Cole, 2004.

[36] J. Stöhr and H. C. Siegmann, "Polarized Electrons and Magnetism," in *Magnetism: From Fundamentals to Nanoscale Dynamics*, pp. 345 – 347, Berlin, Heidelberg: Springer Berlin Heidelberg, 2006.

[37] K. Shinagawa, "Faraday and Kerr Effects in Ferromagnets," in *Magneto-Optics* (S. Sugano and N. Kojima, eds.), vol. 128 of *Springer Series in Solid-State Sciences*, pp. 137 – 177, Berlin, Heidelberg: Springer Berlin Heidelberg, 2000.

[38] J. Stöhr and H. C. Siegmann, "The Magnetic Anisotropy," in *Magnetism: From Fundamentals to Nanoscale Dynamics*, pp. 504 – 511, Berlin, Heidelberg: Springer Berlin Heidelberg, 2006.

[39] M. Getzlaff, *Fundamentals of Magnetism*. Berlin, Heidelberg: Springer Berlin Heidelberg, 2008.

[40] E. C. Stoner and E. P. Wohlfarth, "A mechanism of magnetic hysteresis in heterogeneous alloys," *Philosophical Transactions of the Royal Society of London. Series A, Mathematical and Physical Sciences*, vol. 240, pp. 599–642, may 1948.

[41] A. Thiaville, "Extensions of the geometric solution of the two dimensional coherent magnetization rotation model," *Journal of Magnetism and Magnetic Materials*, vol. 182, no. 1-2, pp. 5–18, 1998.

[42] A. Thiaville, "Coherent rotation of magnetization in three dimensions: A geometrical approach," *Physical Review B*, vol. 61, pp. 12221–12232, may 2000.

[43] J. Stöhr and H. C. Siegmann, "The Torque on a Magnetic Moment in a Magnetic Field," in *Magnetism: From Fundamentals to Nanoscale Dynamics*, pp. 84 – 97, Berlin, Heidelberg: Springer Berlin Heidelberg, 2006.

[44] J. Smit and H. G. Beljers, "Ferromagnetic Resonance Absorption in $BaFe_{12}O_{19}$, a Highly Anisotropic Crystal," *Philips Res. Rep.*, vol. 10, no. 538.221, pp. 113 – 130, 1955.

[45] H. Suhl, "Ferromagnetic Resonance in Nickel Ferrite Between One and Two Kilomegacycles," *Physical Review*, vol. 97, pp. 555–557, jan 1955.

[46] J. Lindner, "Ferromagnetische Resonanz an ultradünnen magnetischen Einfach- und Mehrfachlagen der 3d-Übergangsmetalle - Statik und Dynamik," 2002.

[47] H. J. Hug, B. Stiefel, P. J. A. van Schendel, A. Moser, R. Hofer, S. Martin, H.-J. Güntherodt, S. Porthun, L. Abelmann, J. C. Lodder, G. Bochi, and R. C. O'Handley, "Quantitative magnetic force microscopy on perpendicularly magnetized samples," *Journal of Applied Physics*, vol. 83, pp. 5609–5620, jun 1998.

[48] P. J. A. van Schendel, H. J. Hug, B. Stiefel, S. Martin, and H.-J. Güntherodt, "A method for the calibration of magnetic force microscopy tips," *Journal of Applied Physics*, vol. 88, pp. 435–445, jul 2000.

[49] Joint Committee for Guides in Metrology (JCGM), "Evaluation of measurement data - Guide to the expression of uncertainty in measurement," *JCGM 100:2008*, 2008.

[50] Joint Committee for Guides in Metrology (JCGM), "Evaluation of measurement data – Supplement 1 to the "Guide to the expression of uncertainty in measurement" – Propagation of distributions using a Monte Carlo method," *JCGM 101:2008*, 2008.

[51] Joint Committee for Guides in Metrology (JCGM), "Evaluation of measurement data - Supplement 2 to the "Guide to the expression of uncertainty in measurement" - Extension to any number of output quantities," *JCGM 102:2011*, 2011.

[52] A. A. R. Elshabini-Riad and F. D. Barlow III, "Properties of Thin Film Materials," in *Thin Film Technology Handbook*, p. 12, McGraw-Hill Companies, Inc., 1997.

[53] K. S. Novoselov, "Electric Field Effect in Atomically Thin Carbon Films," *Science*, vol. 306, pp. 666–669, oct 2004.

[54] A. H. Castro Neto, F. Guinea, N. M. R. Peres, K. S. Novoselov, and A. K. Geim, "The electronic properties of graphene," *Reviews of Modern Physics*, vol. 81, pp. 109–162, jan 2009.

[55] E. Y. Andrei, G. Li, and X. Du, "Electronic properties of graphene: a perspective from scanning tunneling microscopy and magnetotransport," *Reports on Progress in Physics*, vol. 75, p. 056501, may 2012.

[56] T. Aichele, A. Lorenz, R. Hergt, and P. Görnert, "Garnet layers prepared by liquid phase epitaxy for microwave and magneto-optical applications – a review," *Crystal Research and Technology*, vol. 38, pp. 575–587, jul 2003.

[57] E. Mallmann, A. Sombra, J. Goes, and P. Fechine, "Yttrium Iron Garnet: Properties and Applications Review," *Solid State Phenomena*, vol. 202, pp. 65–96, may 2013.

[58] A. A. Serga, A. V. Chumak, and B. Hillebrands, "YIG magnonics," *Journal of Physics D: Applied Physics*, vol. 43, p. 264002, jul 2010.

[59] Allresist GmbH, "Positive PMMA E-Beam Resists AR-P 630-670 series," *http://www.allresist.com/ebeamresists-ar-p-631-679/*, jan 2014.

[60] Allresist GmbH, "Protective Coating PMMA Electra 92 (AR-PC 5090)," *http://www.allresist.com/ar-pc-5090-5091-electra-92/*, jan 2016.

[61] J. Taniguchi, "Electron-Beam Machining," in *Micro and Nano Fabrication Technology* (J. Yan, ed.), pp. 555–575, Singapore: Springer, 2018.

[62] N. Yao and Z. L. Wang, "Handbook of Microscopy for Nanotechnology," *Materials Today*, vol. 8, p. 51, aug 2005.

[63] A. A. R. Elshabini-Riad and F. D. Barlow III, "Film Deposition Techniques and Processes," in *Thin Film Technology Handbook*, pp. 1–18, McGraww-Hill Companies, Inc., 1997.

[64] A. A. R. Elshabini-Riad and F. D. Barlow III, "Pattern Generation Techniques," in *Thin Film Technology Handbook*, p. 34, McGraw-Hill Companies, Inc., 1997.

[65] M. Kruskopf, D. M. Pakdehi, K. Pierz, S. Wundrack, R. Stosch, T. Dziomba, M. Götz, J. Baringhaus, J. Aprojanz, C. Tegenkamp, J. Lidzba, T. Seyller, F. Hohls, F. J. Ahlers, and H. W. Schumacher, "Comeback of epitaxial graphene for electronics: large-area growth of bilayer-free graphene on SiC," *2D Materials*, vol. 3, p. 041002, sep 2016.

[66] D. Momeni Pakdehi, J. Aprojanz, A. Sinterhauf, K. Pierz, M. Kruskopf, P. Willke, J. Baringhaus, J. P. Stöckmann, G. A. Traeger, F. Hohls, C. Tegenkamp, M. Wenderoth, F. J. Ahlers, and H. W. Schumacher, "Minimum Resistance Anisotropy of Epitaxial Graphene on SiC," *ACS Applied Materials & Interfaces*, vol. 10, pp. 6039–6045, feb 2018.

[67] D. Momeni Pakdehi, K. Pierz, S. Wundrack, J. Aprojanz, T. T. N. Nguyen, T. Dziomba, F. Hohls, A. Bakin, R. Stosch, C. Tegenkamp, F. J. Ahlers, and H. W. Schumacher, "Homogeneous Large-Area Quasi-Free-Standing Monolayer and Bilayer Graphene on SiC," *ACS Applied Nano Materials*, vol. 2, pp. 844–852, feb 2019.

[68] O. Göktaş, J. Weber, J. Weis, and K. von Klitzing, "Alloyed ohmic contacts to two-dimensional electron system in AlGaAs/GaAs heterostructures down to submicron length scale," *Physica E: Low-dimensional Systems and Nanostructures*, vol. 40, pp. 1579–1581, mar 2008.

[69] K. Nagashio, T. Nishimura, K. Kita, and A. Toriumi, "Contact resistivity and current flow path at metal/graphene contact," *Applied Physics Letters*, vol. 97, p. 143514, oct 2010.

[70] J. Weis and K. von Klitzing, "Metrology and microscopic picture of the integer quantum Hall effect," *Philosophical Transactions of the Royal Society A: Mathematical, Physical and Engineering Sciences*, vol. 369, pp. 3954–3974, oct 2011.

[71] Micro Chem, "NANO^{TM} PMMA and Copolymer," *https://kayakuam.com/products/pmma-positive-resists/*, 2001.

[72] Nanosensors TM, "PPP-MFMR," *https://www.nanosensors.com*, mar 2020.

[73] K. Klauenberg, G. Wübbeler, B. Mickan, P. Harris, and C. Elster, "A tutorial on Bayesian Normal linear regression," *Metrologia*, vol. 52, pp. 878–892, dec 2015.

[74] A. Manzin and V. Nabaei, "Modelling of micro-Hall sensors for magnetization imaging," *Journal of Applied Physics*, vol. 115, p. 17E506, may 2014.

[75] V. Nabaei, R. K. Rajkumar, A. Manzin, O. Kazakova, and A. Tzalenchuk, "Optimization of Hall bar response to localized magnetic and electric fields," *Journal of Applied Physics*, vol. 113, p. 064504, feb 2013.

[76] Quantum Design, "Accuracy of the Reported Moment: Sample Shape Effects," *SQUID VSM Application Note 1500-015*, 2010.

[77] A. Ben Hamida, S. Sievers, K. Pierz, and H. W. Schumacher, "Broadband ferromagnetic resonance characterization of GaMnAs thin films," *Journal of Applied Physics*, vol. 114, p. 123704, sep 2013.

[78] S. Klingler, A. V. Chumak, T. Mewes, B. Khodadadi, C. Mewes, C. Dubs, O. Surzhenko, B. Hillebrands, and A. Conca, "Measurements of the exchange stiffness of YIG films using broadband ferromagnetic resonance techniques," *Journal of Physics D: Applied Physics*, vol. 48, p. 015001, jan 2015.

[79] C. W. Sandweg, Y. Kajiwara, K. Ando, E. Saitoh, and B. Hillebrands, "Enhancement of the spin pumping efficiency by spin wave mode selection," *Applied Physics Letters*, vol. 97, p. 252504, dec 2010.

[80] H. Yu, O. d'Allivy Kelly, V. Cros, R. Bernard, P. Bortolotti, A. Anane, F. Brandl, R. Huber, I. Stasinopoulos, and D. Grundler, "Magnetic thin-film insulator with ultra-low spin wave damping for coherent nanomagnonics," *Scientific Reports*, vol. 4, p. 6848, may 2015.

[81] M. P. Vaughan, "Polarisation," in *Optics*, pp. 153–154, University College Cork, 2014.

[82] P. T. Boggs, R. H. Byrd, J. E. Rogers, and R. B. Schnabel, *User's Reference Guide for ODRPACK Version 2.01 Software for Weighted Orthogonal Distance Regression*. Gaithersburg: National Institute of Standards and Technology, 1992.

[83] K. Siebertz, D. van Bebber, and T. Hochkirchen, *Statistische Versuchsplanung*. Berlin, Heidelberg: Springer Berlin Heidelberg, 2017.

[84] G. Dai, X. Hu, S. Sievers, A. Fernández Scarioni, V. Neu, J. Fluegge, and H. W. Schumacher, "Metrological large range magnetic force microscopy," *Review of Scientific Instruments*, vol. 89, p. 093703, sep 2018.

[85] S. Vock, *Resolving local magnetization structures by quantitative magnetic force microscopy*. PhD thesis, Technische Universität Dresden, 2014.

[86] R. Hoffmann, *Magnetic and Interatomic Forces Measured by Low Temperature Scanning ForceMicroscopy*. PhD thesis, University Basel, 2001.

Own Publications

Conference contributions:

M. Gerken, S. Gorny, S. Lindner, M. Lindner, S. Sievers, H.W. Schumacher: Quantitative imaging of magnetic nanostructures using magneto optical indicator film techniques [poster], DPG-Frühjahrstagung 2017 der Sektion kondensierte Materie, Dresden (2017)

M. Gerken, S. Gorny, S. Lindner, M. Lindner, S. Sievers, H.W. Schumacher: Quantitative imaging of magnetic nanostructures using magneto optical indicator film techniques [poster], Bad Honnef Physics School on Magnetism, Bad Honnef (2017)

R. Puttock, C. W. Barton, H. Corte-León, M. Gerken, A. Manzin, V. Antonov, O. Kazakova: Calibrated magnetic force microscopy with electrostatic compensation [poster], 62nd Annual Conference on Magnetism and Magnetic Materials (MMM), Pittsburgh (2017)

M. Gerken, A. Müller, M. Momeni Pakdehi, T. Weimann, S. Sievers, H. W. Schumacher: Gold and graphene Hall sensors for scanning magnetic field measurements on magnetic microstructures [presentation], DPG-Frühjahrstagung 2018 der Sektion Kondensierte Materie und der Condensed Matter Division der EPS, Berlin (2018)

C. W. Barton, R. Puttock, H. Corte-León, M. Gerken, A. Manzin, S. Sievers, V. Neu, H. W. Schumacher, O. Kazakova: Calibration of MFM probes using electrostatic compensated μ-coils [presentation], 21st International Conference on Magnetism (ICM), San Francisco (2018)

M. Gerken, A. Müller, M. Momeni Pakdehi, T. Weimann, A. Solignac, A. Doll, F. Nording, F. Hohls, S. Sievers, M. Schilling, H. W. Schumacher: Development of gold and graphene nano Hall sensors for scanning magnetic field microscopy [poster], 9th Joint European Magnetic Symposia (JEMS), Mainz (2018)

M. Gerken, S. Sievers, H. W. Schumacher: Fast and quantitative measurement of microscale magnetic stray fields [poster], 15th xMR-Symposium "Magnetoresistive Sensors and Magnetic Systems", Wetzlar (2019)

P. Krzysteczko, A. Fernandez Scarioni, M. Gerken, M. Regin, J. Wells, J. Storm, M. Schmidt, J. Beyer, T. Schurig: From spincaloritronics to quantum magnetometers [presentation], Colloquium of the Department of Electronics, Krakau (2019)

M. Gerken, D. Momeni Pakdehi, T. Weimann, A. Müller, A. Solignac, A. Doll, K. Pierz, F. Hohls, S. Sievers, H. W. Schumacher: Nano Hall sensor for scanning magnetic field microscopy [presentation], DPG-Frühjahrstagung 2019 der Sektion kondensierte Materie, Regensburg (2019)

M. Gerken, D. Momeni Pakdehi, T. Weimann, K. Pierz, F. Hohls, S. Sievers, H. W. Schumacher: Gold and Graphene nano Hall sensors for scanning Hall microscopy [presentation], Magnetic Frontiers - Magnetic Sensors, Lissabon (2019)

M. Gerken, S. Sievers, H. W. Schumacher: Fast and quantitative measurement of microscale magnetic stray fields [poster, Best Poster Award], International Summer School on Metrology 2019 "Prospects of Quantum Metrology", Drübeck (2019)

M. Gerken, T. Weimann, A. Solignac, S. Sievers, H. W. Schumacher: Gold nano Hall sensors for traceable scanning probe magnetic field microscopy [poster], NanoScale 2019, 12th Seminar on Quantitative Microscopy (QM) and 8th Seminar on Nanoscale Calibration, Standards and Methods, Braunschweig (2019)

M. Gerken, D. Momeni Pakdehi, T. Weimann, A. Solignac, K. Pierz, S. Sievers, H. W. Schumacher: Validated nano scanning Hall microscopy [presentation], 64th Annual Conference on Magnetism and Magnetic Materials, Las Vegas (2019)

Paper:

H. Corte-León, V. Neu, A. Manzin, C. W. Barton, T. Yuanjun, M. Gerken, P. Klapetek, H. W. Schumacher O. Kazakova: Comparison and validation of different magnetic force microscopy calibration schemes, Small 2020, 16, 1906144 (2020)
https://doi.org/10.1002/smll.201906144

M. Gerken, S. Sievers, H. W. Schumacher: Inhomogeneous Field Calibration of a Magneto-optical Indicator Film Device, Measurement Science and Technology, 31, 075009 (2020)
https://doi.org/10.1088/1361-6501/ab816e

M. Gerken, A. Solignac, D. Momeni Pakdehi, A. Manzin, T. Weimann, K. Pierz, S. Sievers, H. W. Schumacher: Traceably calibrated scanning Hall probe microscopy at room temperature, Journal of Sensors and Sensor Systems, 9, 391–399 (2020)
https://doi.org/10.5194/jsss-9-391-2020

Acknowledgements

I would particularly like to thank PD Dr. Hans Werner Schumacher for supervising me, providing all necessary equipment and contributing with his scientific experience. Furthermore, I would like to express my gratitude to Prof. Dr. Meinhard Schilling for his supervision.

I am deeply grateful to my mentor, Dr. Sibylle Sievers, for friendly guiding me through all the stages during my PhD. I would like to thank her for on the one hand trusting in my competences and on the other hand always supporting me in the laboratory, during data evaluation and publication processes if I needed it.

I have greatly benefited from Dr. Thomas Weimanns expert knowledge on electron beam lithography and Dr. Aurélie Solignacs expertise with cantilever fabrication. Thanks to her I experienced a perfect communication even about the distance resulting in a successful collaboration. Davood Momeni Pakdehi not only provided the graphene samples but also gave me advice how to handle it. Dr. Alessandra Manzin contributed to the data verification by performing simulations. Also, thanks to Dr. Felix Nording for performing noise measurements on my Hall sensors.

I would like to thank Dr. André Müller for the introduction into sample fabrication and the lithography process as well as Kathrin Störr for answering all questions concerning working procedures in the clean room. With Peter Hinze scanning electron microscopy was always entertaining.

Special thanks to Dr. Xiukun Hu and Alexander Fernández Scarioni. Sharing the office with them was always enjoyable and their company on business trips was pleasant. Moreover, I would like to show my appreciation to all members of department 2.5 who assisted me in terms of setup optimization, technical discussions or helpful advices. You all made my PhD time a great experience.

I would like to show my gratitude to the team of NanoMet (DFG Research Training Group 1952 Metrology for Complex Nanosystems) and B-IGSM for the general organization as well as to all members for the entertaining and easy going company on workshops and summer schools.

Thanks to Sensitec GmbH for providing the magnetic scale and to Matesy GmbH for allocating the CMOS-MagView XL. I would like to thank the team from Innovent e.V. for

implementing required software adaptations. Financial support was supplied by EURAMET for the NanoMag projekt.

Last but not least my hartfelt appreciation goes to my fiancé Ingmar Raulfs for his encouragement and love on every single day and his ability to bring me back down to earth. Likewise I owe my deepest gratitude to my parents Anke and Manfred Gerken, my sister Andrea Gerken as well as my grandparents Martha and Dieter Gänsslen who enabled me to go this way with their support, confidence and love during my whole life.